Travelling wave states in pipe flow

By O Z G E   O Z C A K I R[1],   S A L E H   T A N V E E R[1],
P H I L I P   H A L L[2], and E D W A R D   O V E R M A N[1]

[1]Department of Mathematics, Ohio State University, W 18th Avenue, Columbus, OH 43210,
U.S.A.

[2]Department of Mathematics, Imperial College of Science, Technology and Medicine,180
Queen's Gate, London, SW7 2AZ, U.K.

In this paper, we report numerical calculations of two new travelling wave states with shift and reflect two-fold azimuthal symmetry (S_2 symmetry of Wedin and Kerswell (2004)), characterized by a shrinking core towards the pipe center with increasing R. Further, one of these solutions, termed $C2$, has additional shift and rotate symmetry. We also present arguments to identify all possible scaling solutions as $R \to \infty$. Within the solution class where the axial wave length is independent of R, we identify two families. One is a nonlinear viscous core (NVC) solution characterized by a fully nonlinear interaction between rolls, streaks and waves in a shrinking core of radius $\delta = R^{-1/4}$ where all axial velocity components scale as $R^{-1/2}$, while perpendicular plane components of velocity scale at $R^{-3/4}$. In this case, the wave speed satisfies $(1 - c) = O(R^{-1/2})$. These states are similar to the states calculated by Deguchi and Hall (2014) in boundary layer flows, except that the wave and roll components decay algebraically rather than exponentially in the far-field as one exits the core. The streak for two fold azimuthally symmetric states, with or without additonal shift and rotate symmetry, does not decay as one exits the core until wall effects become important.

The asymptotics also suggests possibility of a second class of solutions that we call vortex wave interaction (VWI) solutions: For $\delta = 1$ or $\delta = R^{-1/6}$, a linear wave of size $\delta^{-4/3}R^{-5/6}$ travelling with wave speed c where $1 - c = O(\delta^2)$ concentrated in a critical layer of thickness $\delta(\delta^4 R)^{-1/3}$ around the critical curve drives rolls of size $R^{-1}\delta^{-1/3}$ localized in a core of radius δ, which in turn drives a streak of size δ^2. We identify previously calculated states by Viswanath (2009a) as a VWI state with $\delta = 1$.

1. Introduction

Research on flows in a pipe is an area of much recent activity. While Hagen-Poiseuille flow is believed to be linearly stable at any Reynolds number R, it is susceptible to non-linear instability with the amplitude of the critical perturbation scaling with some inverse power of R for large values of that parameter. Understanding the fate of trajectories in the phase-space of the Navier-Stokes dynamical system that veer away from the the base flow (either Hagen-Poiseuille flow in a pipe or plane Couette flow) is an important tool in our understanding of turbulence. In characterizing the large time behavior of a dynamical system, an important role is played by the ω-limit sets. These are sets of points in phase space whose arbitrarily close vicinity is visited infinitely often in time by a trajectory in phase-space. This time-invariant ω-limit set includes the steady states or travelling wave solutions of Navier-Stokes equations. Physically, for large Reynolds number R, it

seems that these can correspond to coherent states in a turbulent flow that are observable experimentally if the unstable manifolds of these states are low-dimensional and their evolution in time is slow. That conclusion is suggested by numerical calculations of one of these states in pipe geometry by Viswanath (2009b). Indeed, in intermediate Reynolds number turbulence, it has been observed in the experiments of Hof *et al* (2004) that flow moves between different travelling wave states. The nonlinear states are also of potential technological importance if suitable controls can be inserted in order to stabilize a coherent state that has a significantly smaller drag than for uncontrolled turbulent flow.

All of these coherent states at finite Reynolds number have been discovered through numerical computations in channels(Nagata (1990), Waleffe (1995),Waleffe (1997), Waleffe (1998), Waleffe (2001), Waleffe (2003), Wang *et al* (2007), Gibson *et al* (2009), Blackburn *et al* (2013)) and pipe flows (Faisst and Eckhardt (2003), Hof *et al* (2004), Fitzerald (2004), Wedin and Kerswell (2004), Kerswell and Tutty (2007), Pringle and Kerswell (2007), Viswanath (2007)) with different degrees of symmetry. The physical mechanism to sustain such steady states for large Reynolds number is now well-understood. In the context of pipe flow, if we use cylindrical coordinates (r, θ, z) with cylinder axis aligned along z, and nondimensionalization with domain corresponding to $r < 1$, the nonlinear states are Navier-Stokes traveling wave solutions of the form

$$\mathbf{u} = \mathbf{v}_P(r) + \mathbf{U}(r, \theta) + \mathbf{v}_w(r, \theta, z - ct) \tag{1.1}$$

where $\mathbf{v}_P(r) = (1 - r^2)\hat{\mathbf{z}}$ is Hagen-Poiseuille flow, and $\mathbf{v}_w$ is 2π periodic in both θ and in $\tilde{z} := \alpha(z - ct)$, with zero axial average over a period, denoted by $\langle \mathbf{v}_w \rangle = 0$. If we write $\mathbf{U}(r, \theta) = (U(r, \theta), V(r, \theta), W(r, \theta))$ in cylindrical coordinates, $(U(r, \theta), V(r, \theta), 0)$ is referred to as the *roll* part of the flow and represents stream-wise vortices; $(0, 0, W(r, \theta))$ is termed the *streak* while $\mathbf{v}_w(r, \theta, z - ct)$ represents the wave part of the flow. A similar decomposition is possible for Couette flow and indeed for any predominantly unidirectional shear flows. In a boundary layer study by Hall and Smith (1991) for large Reynolds number R, it was for the first time recognized that in a general shear flow context that an $O(R^{-1})$ streamwise perturbation vorticity can produce an $O(1)$ streak thereby significantly altering the linear stability features of unperturbed flow, and that neutrally stable small amplitude waves of the right magnitude through Reynolds stresses can sustain $O(R^{-1})$ streamwise vortices, which otherwise would have decayed in time. This is exactly the same self-sustaining process (SSP) discovered numerically later for channel (Waleffe (1995), Waleffe (1997)) and pipe flows (Faisst and Eckhardt (2003),Wedin and Kerswell (2004)).

The amplitudes of the rolls, streaks and waves have to be just of the right size to sustain this three way interaction between rolls, streaks and waves. If the streak is too large or too small, the waves would become unstable or die off; if the wave amplitude is too large or too small, the forcing in the roll equation would become too large or too small to sustain a steady streak of just the right size that would create neutrally stable waves. Later, this three way interaction has been described completely for channel flows asymptotically by Hall and Sherwin (2010) through numerical solutions of the rescaled parameter free equations, and remarkable agreement found with direct numerical calculations (Wang *et al* (2007), Blackburn *et al* (2013)) even at moderate R. Following Waleffe (1997), these states have been called SSP states in most of literature; we prefer to call them the VWI (Vortex-Wave Interaction) states as it is descriptive of the physical mechanism that sustains such flows, as discovered originally by Hall and Smith (1991). There is also some evidence to suggest that these VWI states are edge states (Scneider and Eckhardt (2009)) for large Reynolds number in the sense that they separate the initial conditions in phase space between those that return to laminar flow from those that don't. As described by

large R asymptotics by Hall and Sherwin (2010), VWI states are characterized by small amplitude linear waves driving the rolls through Reynolds stress. Another possibility for travelling waves is the occurrence of a fully nonlinear viscous core (NVC) similar to the one observed earlier in boundary layer flows by Deguchi and Hall (2014). While NVC states are also characterized by a three-way interaction mentioned before, there is no meaningful separation in scales between rolls, streaks and waves in this case, and the interaction between different axial wave number components is fully nonlinear as $R \to \infty$, unlike the VWI states. We will use the terminology of travelling wave (TW) to describe both VWI and NVC states.

This paper concerns primarily the calculation of two new travelling wave (TW) solutions, called $C1$ and $C2$, that collapse towards the center of the pipe as $R \to \infty$, which we identify as NVC states. Despite localization of rolls and waves over a shrinking core at the center of the pipe, the streaks do not decay and remain the same size outside as inside the core, until wall effects become important. We also present scaling arguments to identify in general the asymptotic structure of travelling wave solution as $R \to \infty$ for which the axial wave-length α is independent of R. We also confirm that the so-called S-antisymmetric state calculated in a pipe by Viswanath (2009a) is a VWI state with scales in agreement with expected asymptotics. Instead of following previous approaches and trying to use numerical continuation of some fictitous forcing to determine suitable initial guess for our Newton iteration procedure, which need not always result in convergence, we perturb the base Hagen-Poiseuille flow by introducing azimuthal suction-injection of small magnitude that is enough to cause instability of base flow at large R. Using the solution from the resulting Hopf-bifurcation as an initial guess for small amplitude waves, we continue in wave amplitude before turning off the suction-injection. Our calculations, we believe, are also reasonably efficient and accurate and are valid at very large R; this is helped in large part by exploiting asymptotic scalings of wave amplitudes in the choice of preconditioners needed to solve the large linear systems of equations arising in Newton iteration.

The travelling wave (TW) solutions we are looking for satisfy the Navier-Stokes

$$\mathbf{u}_t + \mathbf{u} \cdot \nabla \mathbf{u} = -\nabla p + \frac{1}{R} \Delta \mathbf{u} \quad , \quad \nabla \cdot \mathbf{u} = 0 \tag{1.2}$$

in the form

$$\mathbf{u} = \mathbf{v}_B(r, \theta) + \mathbf{v}(r, \theta, z - ct) \tag{1.3}$$

$\mathbf{v}_B$ is the base flow, while (r, θ, z) are cylindrical coordinates with pipe aligned along the z-axis. We assume $\mathbf{v}$ to be 2π periodic in θ and $\tilde{z} := \alpha(z - ct)$ and satisfies boundary condition on the wall

$$\mathbf{v}(1, \theta, z - ct) = 0 \tag{1.4}$$

We take the base flow $\mathbf{v}_B = \mathbf{v}_B(r, \theta)$ to be the steady Navier-Stokes solution with only nonzero radial and azimuthal components satisfying a periodic suction-injection boundary condition at the wall:

$$\mathbf{v}_B(1, \theta) = \frac{s}{R} \cos(k_0 \theta) \hat{\mathbf{r}} \tag{1.5}$$

with the same θ-averaged pressure gradient $-\frac{4}{R}\hat{\mathbf{z}}$ as for Hagen-Poiseuille flow $\mathbf{v}_P = (1 - r^2)\hat{\mathbf{z}}$.

Solutions to (1.2) in the form (1.3) have been computed before for $s = 0$, *i.e.* when $\mathbf{v}_B = \mathbf{v}_P$, through an initial guess determination procedure (Wedin and Kerswell (2004)) that mimics the three-way interaction between rolls, streaks and waves and/or introduction of forcing (Faisst and Eckhardt (2003)). Our procedure is different; we first study the linear

stability of the base flow $\mathbf{v}_B$ for $s \neq 0$ and determine (α, R) at which the flow becomes unstable. A finite amplitude solution from a Hopf-bifurcation at a neutrally stable point is then used to determine initial guess in the Newton iteration procedure for traveling wave solutions in the form (1.3); at finite wave amplitude far from the bifurcation point, the solution is then continued to $s = 0$ to determine a TW state without suction/injection. We used this to recalculate the TW states of Wedin and Kerswell (2004) in a more efficient manner. We also find new states, which we later identify as finite R realization of NVC asymptotic states, that are concentrated in the center of the pipe as $R \to \infty$. We make no attempt to determine all possible TW states numerically; we focus mainly on the properties of these new center-modes that are concentrated at the center of the pipe. Investigation of the scaling properties of these states, both numerically and through asymptotic arguments, constitutes the most significant part of this paper. We also present more general arguments to identify all possible consistent $R \to \infty$ asymptotic scalings of roll, streak and wave components of a travelling wave state when the axial wave number α is independent of R. It is to be noted that these states differ from the spiralling center modes of Smith and Bodonyi (1982), Deguchi and Walton (2013).

2. Computational method

The efficient and accurate numerical calculation of the three dimensional large Reynolds number travelling wave solutions of the Navier Stokes equations is challenging since boundary and critical layers have to be adequately resolved. This requires a large number of modes which as a result leads to large matrix inversion problem for the associated Newton iteration scheme. Our basis representation for the velocity is similar to Wedin and Kerswell (2004), except that we use a sin, cos real valued representation instead of complex exponentials in both the azimuthal (θ) and axial (z) directions. We also find it more efficient to eliminate the pressure through a Poisson equation rather than by enforcing the divergence condition directly. The matrix inversion process is similar to Viswanath (2009a), though our choice of preconditioner exploits the knowledge (Hall and Sherwin (2010)) that TW states have only a weak nonlinear interaction between different wave modes when R is large.

Now let us describe the numerical procedure employed for eliminating pressure term $-\nabla q$; the procedure is similar for the basic state, stability and TW calculations. The pressure elimination is efficacious in TW calculations since the inversions of relatively small matrices are involved for each Fourier mode in θ and z and that is more than compensated for by the reduction of the size of the Jacobian by a fourth in the Newton iteration scheme for the nonlinear system. Next we briefly describe calculations of the basic state $\mathbf{v}_B \neq \mathbf{v}_P$ when the suction-injection parameter $s \neq 0$. The description of the calculation of the linear stability modes and TW states then follow.

2.1. *Collocation Method for Pressure - Poisson Equation*

In the context of TW calculations, we use the pressure† representation:

$$q = \sum_{\substack{0 \leqslant j \leqslant N \\ 0 \leqslant k \leqslant M \\ 0 \leqslant l \text{ even } \leqslant P}} (q_{jkl}^{(1)} \cos l\tilde{z} + q_{jkl}^{(2)} \sin l\tilde{z})\Omega_j(r; kk_0) \cos kk_0\theta$$

$$+ \sum_{\substack{0 \leqslant j \leqslant N \\ 0 \leqslant k \leqslant M \\ 0 \leqslant l \text{ odd } \leqslant P}} (q_{jkl}^{(1)} \cos l\tilde{z} + q_{jkl}^{(2)} \sin l\tilde{z})\Omega_j(r; kk_0) \sin kk_0\theta \ , \quad \text{where} \ \ \tilde{z} = \alpha(z - ct) \ ,$$

$$(2.1)$$

where

$$\Omega_j(r; k) = \begin{cases} T_{2j+1}(r) & k \text{ odd} \\ T_{2j}(r) & k \text{ even } (k, l) \neq (0, 0) \\ T_{2j+2}(r) & \text{when } (k, l) = (0, 0), \end{cases} \tag{2.2}$$

For the basic state $\mathbf{v}_B$, only $l = 0$ term is needed in (2.1), while for linear stability, only the $l = 1$ terms appears; in the latter case, a complex representation

$$q = e^{i\tilde{z}} \sum_{\substack{0 \leqslant j \leqslant N \\ 0 \leqslant k \leqslant M}} q_{jk}\Omega_j(r; kk_0) \sin kk_0\theta \ , \tag{2.3}$$

is more convenient. In each case, we are interested in solving the Poisson equation

$$\Delta q = \mathcal{N}(\mathbf{v}), \tag{2.4a}$$

for given $\mathbf{v}$ with compatible Neumann boundary condition of the form

$$\frac{\partial q}{\partial r} = \mathcal{N}_b(\mathbf{v}) \qquad \text{at } r = 1 \ , \tag{2.4b}$$

where $\mathcal{N}(\mathbf{v})$ and $\mathcal{N}_b(\mathbf{v})$ are defined for each of basic state, linear stability and TW in (2.15)-(2.16), (2.21a)- (2.21b) and (2.23a)-(2.23b), respectively. The representation (2.3) is appropriate for stability since $\mathbf{v}$ and therefore each of $\mathcal{N}[\mathbf{v}]$ and $\mathcal{N}_b[\mathbf{v}]$ (see (2.21a)-(2.21b)) is of the form $e^{i\tilde{z}}G$ for some G. We chose the shifted basis $T_{2j+2}(r)$ for $k = 0$, $l = 0$ in (2.2) to exclude constant term $T_0(r) = 1$, thereby ensuring unique solution q to the Poisson equation (2.4a) with compatible Neumann B.C. (2.4b)).

We now describe how q_{jkl}^1 and q_{jkl}^2, appearing in (2.1), are determined in TW calculations. The procedure for basic state and linear stability is quite similar, only simpler. For a given truncated basis representation for $\mathbf{v}$ (see (2.25)) we evaluate $\mathbf{v}$ at the following set of points:

$$(r_{j'}, \theta_k, \tilde{z}_l) = \left(\cos \frac{(2(N - j') + 1)\pi}{4N + 4}, \frac{2\pi/k_0}{4M + 1}(k - 1), \frac{2\pi}{4P + 1}(l - 1) \right)$$

for $j' = 0, \ldots, N - 1$, $k = 1, \ldots, 4M + 1$ and $l = 1, \ldots, 4P + 1$ using the direct evaluation of $\Psi_j(r_{j'})$, $\Phi_j(r_{j'})$ and their derivatives, and Fourier transform in θ and $\tilde{z}$. Here, we use twice as many azimuthal and axial points to avoid aliasing error in the calculation of nonlinear terms. Thus $\mathcal{N}(\mathbf{v})$ is evaluated at these grid points $(r_{j'}, \theta_k, \tilde{z}_l)$. Using a discrete Fourier transform in θ and $\tilde{z}$, then dropping higher order modes ($k > M, l > P$), $f_{kl}^{(1)}(r_{j'})$,

---

† Here q, which is periodic, and is actually the deviation of pressure from the linear term $-\frac{4}{R}z$.

$f_{kl}^{(2)}(r_{j'})$ for each $j' = 0, \ldots, N-1$ as well as, $f_b^{(1)}$ and $f_b^{(2)}$ are determined in the following representation of $\mathcal{N}[\mathbf{v}]$ and $\mathcal{N}_b[\mathbf{v}]$:

$$
\mathcal{N}[\mathbf{v}](r_{j'}, \theta, \tilde{z}) = \sum_{\substack{0 \leqslant k \leqslant M \\ 0 \leqslant l \text{ even} \leqslant P}} (f_{kl}^{(1)}(r_{j'}) \cos l\tilde{z} + f_{kl}^{(2)}(r_{j'}) \sin l\tilde{z}) \cos k k_0 \theta
$$
$$
+ \sum_{\substack{0 \leqslant k \leqslant M \\ 1 \leqslant l \text{ odd} \leqslant P}} (f_{kl}^{(1)}(r_{j'}) \cos l\tilde{z} + f_{kl}^{(2)}(r_{j'}) \sin l\tilde{z}) \sin k k_0 \theta
$$
(2.5a)

for $j' = 0, \ldots, N$, and

$$
\mathcal{N}_b[\mathbf{v}](\theta, \tilde{z}) = \sum_{\substack{0 \leqslant k \leqslant M \\ 0 \leqslant l \text{ even} \leqslant P}} (f_{b_{kl}}^{(1)} \cos l\tilde{z} + f_{b_{kl}}^{(2)} \sin l\tilde{z}) \cos k k_0 \theta
$$
$$
+ \sum_{\substack{0 \leqslant k \leqslant M \\ 1 \leqslant l \text{ odd} \leqslant P}} (f_{b_{kl}}^{(1)} \cos l\tilde{z} + f_{b_{kl}}^{(2)} \sin l\tilde{z}) \sin k k_0 \theta.
$$
(2.5b)

Fourier-Transform process also generates terms other than the ones shown in (2.5b) without the (k, l) parity; however, due to the representation (2.25), these terms are within round-off error and ignored. On the other hand, from the representation of q at the radial grid points $r_{j'}$ for $j' = 0, \ldots N-1$

$$
\Delta q = \sum_{j=0}^{N} \sum_{\substack{0 \leqslant k \leqslant M \\ 0 \leqslant l \text{ even} \leqslant P}} (q_{jkl}^{(1)} \cos l\tilde{z} + q_{jkl}^{(2)} \sin l\tilde{z}) \Delta\Omega_j(r_{j'}; kk_0) \cos k k_0 \theta
$$
$$
+ \sum_{j=0}^{N} \sum_{\substack{0 \leqslant k \leqslant M \\ 0 \leqslant l \text{ odd} \leqslant P}} (q_{jkl}^{(1)} \cos l\tilde{z} + q_{jkl}^{(2)} \sin l\tilde{z}) \Delta\Omega_j(r_{j'}; kk_0) \sin k k_0 \theta ,
$$
(2.6)

where

$$
\Delta\Omega_j(r_{j'}; kk_0) := \frac{\partial^2}{\partial r^2} \Omega_j(r_{j'}; kk_0) + \frac{1}{r}\frac{\partial}{\partial r} \Omega_j(r_{j'}; kk_0) - \left(\frac{(kk_0)^2}{r_{j'}^2} + (\alpha l)^2\right) \Omega_j(r_{j'}; kk_0).
$$

Then, equating Fourier coefficients in θ and $\tilde{z}$ in (2.5a) and (2.5b) with those in (2.6) and similar representation of $\frac{\partial q}{\partial r}$ at the boundary $r = 1$, we obtain for $i = 1, 2$, $0 \leqslant k \leqslant M$, $0 \leqslant l \leqslant P$ the following conditions:

$$
\sum_{j=0}^{N} q_{jkl}^{(i)} \Delta\Omega_j(r_{j'}; kk_0) = f_{kl}^{(i)}(r_{j'})
$$
(2.7)

at the set of interior collocation points $\{r_{j'}\}_{j'=0}^{N-1}$ and the following at $r = 1$:

$$
\sum_{j=0}^{N} q_{jkl}^{(i)} \Omega_j'(1; kk_0) = f_{b_{kl}}^{(i)}
$$
(2.8)

Equations (2.6)-(2.7) constitutes a system of $(N+1)$ linear equations for $(N+1)$ unknowns $q_{jkl}^{(i)}$ for each (k, l) in the given range, for each $i = 1, 2$, which was solved using Gaussian

elimination. Once $q_{jkl}^{(i)}$ is known, we can evaluate

$$-\nabla q = -\sum_{j=0}^{N} \sum_{\substack{0 \leqslant k \leqslant M \\ 0 \leqslant l \text{ even} \leqslant \text{P}}} \nabla \left((q_{jkl}^{(1)} \cos l\tilde{z} + q_{jkl}^{(2)} \sin l\tilde{z}) \Omega_j(r; kk_0) \cos kk_0\theta \right)$$

$$-\sum_{j=0}^{N} \sum_{\substack{0 \leqslant k \leqslant M \\ 0 \leqslant l \text{ odd} \leqslant \text{P}}} \nabla \left((q_{jkl}^{(1)} \cos l\tilde{z} + q_{jkl}^{(2)} \sin l\tilde{z}) \Omega_j(r; kk_0) \sin kk_0\theta \right) \,, \tag{2.9}$$

in the Navier-Stokes momentum equation, as described in the following sub-sections. The q calculation for the basic state and the linear stability problem are analogous but simpler since only one l-mode is involved.

2.2. *Basic State Calculation*

For the basic state calculation for $s \neq 0$, we find it convenient to decompose

$$\mathbf{v}_B = \mathbf{g}_S + \mathbf{v}_S \,, \tag{2.10}$$

where

$$\mathbf{g}_S = \frac{s}{R} \left(r(2 - r^2) \cos(k_0\theta) \,, -\frac{4}{k_0} r(1 - r^2) \sin(k_0\theta) \,, 0 \right) \tag{2.11}$$

is a smooth divergence free function chosen to satisfy boundary condition at the wall, which allows $\mathbf{v}_S = (u_S(r,\theta), v_S(r,\theta), w_S(r,\theta))$ to have the the same type of basis representation as for TW states:

$$\begin{pmatrix} u_S \\ v_S \\ w_S \end{pmatrix} = \begin{pmatrix} 0 \\ 0 \\ 1 - r^2 \end{pmatrix} + \sum_{\substack{0 \leqslant j \leqslant N \\ 0 \leqslant k \leqslant M}} \begin{pmatrix} u_{jk} \Phi_j(r; kk_0) \cos kk_0\theta \\ v_{jk} \Phi_j(r; kk_0) \sin kk_0\theta \\ w_{jk} \Psi_j(r; kk_0) \cos kk_0\theta \end{pmatrix} \tag{2.12}$$

where Φ_j, Ψ_j is given in terms of Tchebyshev polynomials T_j as follows:

$$\Phi_j(r; k) = T_{2j+2}(r) - T_{2j}(r) \text{ for } k \text{ odd} \,, \Phi_j(r; k) = T_{2j+3}(r) - T_{2j+1}(r) \text{ for } k \text{ even} \tag{2.13}$$

$$\Psi_j(r; k) = T_{2j+3}(r) - T_{2j+1}(r) \text{ for } k \text{ odd} \,, \Psi_j(r; k) = T_{2j+2}(r) - T_{2j}(r) \text{ for } k \text{ even} \tag{2.14}$$

We decompose $p_S = -\frac{4z}{R} + q_S$ where q_S satisfies the Poisson equation

$$\Delta q_S = -\nabla \cdot (\mathbf{v}_S \cdot \nabla \mathbf{v}_S + \mathbf{g}_S \cdot \nabla \mathbf{v}_S + \mathbf{v}_S \cdot \nabla \mathbf{g}_S + \mathbf{f}_S) := \mathcal{N}[\mathbf{v}_s] \,, \tag{2.15}$$

subject to compatible Neumann boundary condition at $r = 1$:

$$\frac{\partial q_S}{\partial r} = \hat{\mathbf{r}} \cdot \left(\frac{1}{R} \Delta \mathbf{v}_s - \mathbf{f}_S \right) =: \mathcal{N}_b[\mathbf{v}_S] \,, \tag{2.16}$$

where

$$\mathbf{f}_S = -\frac{1}{R} \Delta \mathbf{g}_S + \mathbf{g}_S \cdot \nabla \mathbf{g}_S \tag{2.17}$$

We solve (2.15) with boundary condition (2.16) in a procedure similar to that described in the preceding section, except that no collocation in $\tilde{z}$ is involved since only $l = 0$ mode is present. This allows computation of $-\nabla q_S = -\nabla \Delta^{-1} \mathcal{N}[\mathbf{v_S}]$ for given $\mathbf{v}_S$ in the following equation:

$$\mathbf{v}_S \cdot \nabla \mathbf{v}_S + \mathbf{g}_S \cdot \nabla \mathbf{v}_S + \mathbf{v}_S \cdot \nabla \mathbf{g}_S = -\frac{4}{R} \hat{\mathbf{z}} - \nabla q_S + \frac{1}{R} \Delta \mathbf{v}_S - \mathbf{f}_S \tag{2.18}$$

Using a Galerkin approximation $0 \leqslant k \leqslant K$ in θ and collocation at the radial points $\{r_{j'}\}_{j'=0}^{N}$ we obtain a system of $3 \times (K+1) \times (N+1)$ algebraic equations for as many unknowns $\{u_{k,j}, v_{k,j}, w_{k,j}\}_{k=0,\cdots K, j=0,\cdots,N}$ that is solved through Newton iteration. The initial guess is obtained through a continuation process, starting at $s = 0$, when $\mathbf{v}_S = \mathbf{v}_P$ is an exact solution.

2.3. *Linear Stability Calculations of basic state* $\mathbf{v}_B$

The linear stability of base state $\mathbf{v}_B$ is governed by the nonzero solution $\mathbf{v}(r, \theta, z)$ satisfying the linear equation

$$-c\frac{\partial \mathbf{v}}{\partial z} = -\nabla \Delta^{-1} \mathcal{N}[\mathbf{v}] + \frac{1}{R}\Delta \mathbf{v} - \mathbf{v}_B \cdot \nabla \mathbf{v} - \mathbf{v} \cdot \nabla \mathbf{v}_B \ , \tag{2.19}$$

with boundary conditions

$$\mathbf{v}(1, \theta, z) = 0 \ , \tag{2.20}$$

where c is allowed to be complex, with $\Im c$ is the associated the growth rate for the particular mode, and in this case

$$\mathcal{N}[\mathbf{v}] := \nabla \cdot [-\mathbf{v_B} \cdot \nabla \mathbf{v} - \mathbf{v} \cdot \nabla \mathbf{v_B}] \tag{2.21a}$$

with $\mathcal{N}_b[\mathbf{v}]$ appearing implicitly in Δ^{-1} operation are now given by

$$\mathcal{N}_b[\mathbf{v}] := \hat{\mathbf{r}} \cdot \left[\frac{1}{R}\Delta \mathbf{v} - \mathbf{v_B} \cdot \nabla \mathbf{v} - \mathbf{v} \cdot \nabla \mathbf{v_B}\right] \tag{2.21b}$$

Since the basic state $\mathbf{v}_B$ has no z dependence, it is enough to replace $\mathbf{v}(r, \theta, z)$ by $e^{i\tilde{z}}\mathbf{v}(r, \theta)$ in (2.19)-(2.21b), in which case the operator $\frac{\partial}{\partial z}$ in (2.19) is replaced by multiplication by $i\alpha$. We also notice that in this case, each term $\mathcal{N}[\mathbf{v}]$ and $\mathcal{N}_b[\mathbf{v}]$ is linear in $\mathbf{v}$, implying that $\nabla \Delta^{-1} \mathcal{N}[\mathbf{v}]$ obtained through a procedure detailed in §2.1 will have only a $e^{i\tilde{z}}$ dependence in z. Therefore, as for the basic state, no collocation point in $\tilde{z}$ is necessary for computation of q. The basis representation for $\mathbf{v}(r, \theta)$ is the same form as that for $\mathbf{v}_S$, except that there is no Poisseiulle term $(1 - r^2)\hat{\mathbf{z}}$. Once again, as for $\mathbf{v}_S$, Galerkin in θ and collocation at the set of radial points $\{r_j\}_{j=0}^{N}$ leads to a set of equations, this time linear and homogeneous, in the matrix form $\mathbf{Ax} = c\mathbf{Bx}$, where $\mathbf{B}$ has only nonzero components in a diagonal block with each block of size $(N+1) \times (N+1)$ arising from evaluation of $\{\Phi_{j'}(r_j), \Psi_{j'}(r_j)\}_{0 \leqslant j, j' \leqslant N}$, which allows $\mathbf{B}$, to be inverted readily, thereby allowing use of a standard eigenvalue/eigenvector solver for $\mathbf{B}^{-1}\mathbf{A}$.

2.4. *TW calculations*

As mentioned in the introduction, TW states correspond to solutions of Navier-Stokes in the form $\mathbf{u} = \mathbf{v}_B(r, \theta) + \mathbf{v}(r, \theta, z - ct)$ where c is now real. It is clear that $\mathbf{v}$ satisfies

$$-c\frac{\partial \mathbf{v}}{\partial z} + (\mathbf{v} \cdot \nabla)\mathbf{v} = -\nabla \Delta^{-1} \mathcal{N}[\mathbf{v}] + \frac{1}{R}\Delta \mathbf{v} - \mathbf{v_B} \cdot \nabla \mathbf{v_B} - \mathbf{v_B} \cdot \nabla \mathbf{v} - \mathbf{v} \cdot \nabla \mathbf{v_B} \ , \quad (2.22)$$

where in this case

$$\mathcal{N}[\mathbf{v}] := \nabla \cdot [-\mathbf{v_B} \cdot \nabla \mathbf{v_B} - \mathbf{v_B} \cdot \nabla \mathbf{v} - \mathbf{v} \cdot \nabla \mathbf{v_B}] \ , \tag{2.23a}$$

$$\mathcal{N}_b[\mathbf{v}] := \hat{\mathbf{r}} \cdot \left[\frac{1}{R}\Delta \mathbf{v} - \mathbf{v_B} \cdot \nabla \mathbf{v_B} - \mathbf{v_B} \cdot \nabla \mathbf{v} - \mathbf{v} \cdot \nabla \mathbf{v_B}\right] \tag{2.23b}$$

where $\mathcal{N}_b[\mathbf{v}]$ appears in definition of Δ^{-1} through Neumann Boundary condition. On the pipewall,

$$\mathbf{v}(1, \theta, z - ct) = 0 \ . \tag{2.24}$$

We use the following representation of $\mathbf{v}$ in cylindrical coordinates

$$
\begin{pmatrix} u \\ v \\ w \end{pmatrix} = \sum_{\substack{0 \leqslant j \leqslant N \\ 0 \leqslant k \leqslant M \\ 0 \leqslant l \ \text{even} \leqslant P}} \begin{pmatrix} (u_{jkl}^{(1)} \cos l\tilde{z} + u_{jkl}^{(2)} \sin l\tilde{z})\Phi_j(r; kk_0) \cos kk_0\theta \\ (v_{jkl}^{(1)} \cos l\tilde{z} + v_{jkl}^{(2)} \sin l\tilde{z})\Phi_j(r; kk_0) \sin kk_0\theta \\ (w_{jkl}^{(1)} \sin l\tilde{z} + w_{jkl}^{(2)} \cos l\tilde{z})\Psi_j(r; kk_0) \cos kk_0\theta \end{pmatrix}
$$

$$
+ \sum_{\substack{0 \leqslant j \leqslant N \\ 0 \leqslant k \leqslant M \\ 1 \leqslant l \ \text{odd} \leqslant P}} \begin{pmatrix} (u_{jkl}^{(1)} \cos l\tilde{z} + u_{jkl}^{(2)} \sin l\tilde{z})\Phi_j(r; kk_0) \sin kk_0\theta \\ (v_{jkl}^{(1)} \cos l\tilde{z} + v_{jkl}^{(2)} \sin l\tilde{z})\Phi_j(r; kk_0) \cos kk_0\theta \\ (w_{jkl}^{(1)} \sin l\tilde{z} + w_{jkl}^{(2)} \cos l\tilde{z})\Psi_j(r; kk_0) \sin kk_0\theta \end{pmatrix}
\tag{2.25}
$$

This is a basis representation suitable† at $r = 0$ for the so-called S-symmetric states discussed in Wedin and Kerswell (2004); note Viswanath (2009b) calculates S anti-symmetric states which has a representation different from (2.25). In addition, this representation fixes the origin in θ, even in the case when $s = 0$, when basic state $\mathbf{v}_B = \mathbf{v}_P$ is rotationally symmetric θ. In addition, to fix the origin in z, we impose the phase condition

$$
\sum_{j=0}^{N} u_{j,1,1}^{(1)} = 0
\tag{2.26}
$$

We use representation (2.25) and equate coefficients of $\cos(kk_0\theta)\cos(l\tilde{z})$, $\sin(kk_0\theta)\cos(l\tilde{z})$, $\cos(kk_0\theta)\sin(l\tilde{z})$, and $\sin(kk_0\theta)\sin(l\tilde{z})$ for $0 \leqslant k \leqslant M$, $0 \leqslant l \leqslant P$ on both sides of (2.22) and evaluate resulting expressions at the collocation points $\{r_{j'}\}$. This, together with scalar equation (2.26), results in a nonlinear system of algebraic equations for $(\mathbf{X}, c)$ of the form:

$$
\mathbf{G}(\mathbf{X}, c; \boldsymbol{\beta}) = 0
\tag{2.27}
$$

where $\mathbf{X} = \left\{ u_{jkl}^{(i)}, v_{jkl}^{(i)}, w_{jkl}^{(i)} \right\}_{j,k,l,i}$ and $\boldsymbol{\beta} = (R, \alpha, s)$ is the set of specified parameters. More details about the number of variables, calculation of corresponding Jacobian $\mathbf{J}$ that arise in Newton iteration and its efficient inversion through use of preconditioner and GMRES is described elsewhere (Ozcakir (2014)). In the vicinity of neutral stability points $\alpha = \alpha_N(R)$, shown in red crosses in Figure 1 for $R = 1700$, $s = 10$, we use eigenfunction at $\alpha = \alpha_N$ of the stability problem summed with its complex conjugate, re-expressed in the real form (2.25) to determine suitable initial guess for travelling wave calculations. Sufficiently far from the bifurcation point, we continue to $s \to 0$ to determine a TW state. Note that the azimuthal symmetry ($k_0 = 2$) of the suction-injection profile is reflected in the ultimate symmetry of the travelling wave solutions.

3. Numerical Results for TW calculations

The calculations described thus far are limited to $k_0 = 2$; i.e. two-fold azimuthally symmetric TW states. Unless otherwise stated, in our figures we used $(N, M, P) = (85, 12, 5)$ when $R > 5000$ and $(N, M, P) = (45, 8, 5)$ when $R < 5000$. Significantly increasing each of N, M and P for particular Reynolds number in this range and comparing with baseline calculations suggested that the calculation for c was accurate to four significant digits, whereas the velocity was accurate to at least to three digits. We display with cross

† Though we did not explictly impose the regularity condition at $r = 0$ of Batchelor and Gill (1962), we checked that it was satisfied to a numerical accuracy sufficient for the reported calculation.

marks results from higher resolution calculation that resulted in the largest deviation from baseline calculations shown in the solid or dashed lines.

We reproduced the S-symmetric solution of Wedin and Kerswell (2004) for $k_0 = 2$. The comparison of c vs R curve for $\alpha = 1.55$ is shown in Figure 2. Our calculations for $(N, M, P) = (45, 8, 5)$ (shown in blue) is indistinguishable from the gray curve of Wedin and Kerswell (2004). The black curve, which sits on top of the blue curve corresponds to higher resolution $(N, M, P) = (85, 12, 5)$. More details of the flow in a plane perpendicular to the pipe axis corresponding to points labelled (i) and (j) in Fig. 2 is shown in Fig. 4 for the WK solution. Note that the Poissueille flow has been subtracted out. The lighter color corresponds to positive values of streak W, *i.e.* the streamwise-averaged axial flow is into the plane, while darker colors correspond to negative W. This pattern looks the same to the eye as Wedin and Kerswell (2004). In (a), corresponding to (i), $\max W = 0.076$, $\min W = -0.333$, $\max |(U, V)| = 0.014$, while in (b), corresponding to (j), $\max W = 0.0741$, $\min W = -0.296$, $\max |(U, V)| = 0.0121$ in close agreement to Wedin and Kerswell (2004).

The scaling of rolls, streaks and waves for the computed WK solutions are roughly in agreement with the expected VWI scales for $\delta = 1$ (see §4.2), which is the same as the Hall and Sherwin (2010) scaling in channel flows though our inability to continue the WK solution past about $R = 11,000$ hampered a more precise comparison between numerical results and $R \to \infty$ scaling results.

In addition, two new branches of travelling wave solutions have been found, which we denote as $C1$ and $C2$. Besides the S-symmetry (shift-and-reflect) the $C2$ branch also has Ω_2-symmetry (shift-and-rotate) as defined in Pringle *et al*(2009), though this additional symmetry was not imposed in the numerical code. As pointed out earlier, in the representation (2.25), this corresponds to nonzero contributions only for even $k + l$. For $k_0 = 2$, this results in rolls and streams having four-fold azimuthal symmetry.

However, unlike other states calculated before these new branches appear to have a collapsing vortex-wave structure toward the center of pipe as $R \to \infty$ which will be quantified. These states are also different from the helical center modes of Smith and Bodonyi (1982)(confirmed for finite R by Deguchi and Walton (2013)) where the dependence in θ and z are linked; these spiral modes are special to $k_0 = 1$. In Figure 3 the phase speed c is shown as a function of R for the two wave numbers α for $C1$ and $C2$ solutions for the lower-branch. For $C1$ and $C2$, we were able to compute solutions indefinitely with increasing R, though resolution checks were limited to $R < 2 \times 10^5$.

For these new states, the streamwise averaged flows are displayed in a plane perpendicular to the pipe axis at several values of R in Figures 5, 7 and 9 where the rolls (U, V) are depicted using arrows whilst the streak velocity intensity is represented in colors. For comparison we also present the WK solution at $R = 3940$ in Figure 6 and $R = 10000$ in Figure 8 (Note that we were unable to obtain numerical convergence for the WK branch of solution for R larger than about 11000). In all of the plots, the streak velocity ranges in the interval $[-0.4163, 0.0963]$ where the minimum streak velocity is shown in dark red and the maximum streak velocity in light yellow. Note that the streaks get weaker as R becomes larger, in accordance with asymptotic scaling results in §4.

The gray surfaces in Figures 10-21 show surfaces of constant magnitude of streamwise velocity, excluding Poisseuille, at a value of 0.8 times the maximal value for three different R values for states $C1$ and $C2$ for two different streamwise wave number α. The colored surfaces in the corresponding figures denote iso-surfaces of 0.8 times maximal or minimal streamwise vorticity, with blue corresponding to positive vorticity and red corresponding to negative vorticity. Note that while the vortex structures become closer to the origin with larger R, the streamwise velocity magnitude iso-surface, which is dominated by

the streak component, does not shrink noticeably towards the origin. This feature is explained theoretically in §4.4 and owes its origin to the mechanism found by Deguchi and Hall (2014).

A quantity of general interest and which has some technological implications is the friction factor Λ associated with each of these states. Λ is defined as

$$\Lambda := \frac{64Re}{Re_m^2}$$

where,

$$Re_m := 2\overline{w}/\nu$$

and $\overline{w}$ is the nondimensional mean streamwise velocity given by

$$\overline{w} = 2 \int\limits_0^1 \left((1 - r^2) + \sum_{j=0}^{N} w_{j00}^{(2)} \Psi_j(r; 0) \right) r dr \tag{3.1}$$

Λ is plotted against R for WK, $C1$, $C2$ solutions for three different values of α and compared against the Hagen-Poiseuille value of $\frac{64}{R}$ in Figure 23.

In order to understand the asymptotic scaling of the new centermodes $C1$ and $C2$, in Figure 22, $1 - c$ is plotted against R on a $\log - \log$ scale for two different values of α, with slopes m ranging from -0.32 to -0.38. This does not change much with higher resolution calculations shown in cross marks. A linear least square fit using data in the range $5 \times 10^4 < R < 2 \times 10^5$ is shown in dotted lines. We also noted that the slope in the regime $10^5 < R < 2 \times 10^5$ is about three percent larger than than the quoted value, suggesting that the solution may not have reached an ultimate asymptotic scale. Also, we noted a consistent tendency for $1 - c$ versus R curve to steepen slightly with increasing α. For instance, the linear fit based on limited calculations for $\alpha = 2.51$ in a large R regime for $C1$ solution shows† $(1 - c) \sim R^{-0.39}$

Now we report on other scaling features of the $C1$, $C2$ solutions for large R, restricted to $R < 2 \times 10^5$. These include the behaviors of rolls, streaks and waves, including the location and magnitude of their maximum. We will also consider the collapsing of these solutions towards the center of the pipe. It is convenient to define

• the amplitude $A_k^U(r)$ of k-th azimuthal Fourier component of the radial roll velocity:

$$A_k^U(r) = \sqrt{(\sum_{n=0}^{N} u_{nk0}^{(1)} \Phi_n(r))^2 + (\sum_{n=0}^{N} u_{nk0}^{(2)} \Phi_n(r))^2} \tag{3.2}$$

with the maximum

$$A_{k,m}^U := \max_r A_k^U(r) = A_k^U(r_m)$$

attained at $r = r_m$.

• the amplitude $A_k^S(r)$ of k-th azimuthal component of the streaks:

$$A_k^S(r) = \sqrt{(\sum_{n=0}^{N} w_{nk0}^{(1)} \Psi_n(r))^2 + (\sum_{n=0}^{N} w_{nk0}^{(2)} \Psi_n(r))^2} \tag{3.3}$$

† The notation '$\sim$' here and in the rest of the paper is *not* in the usual asymptotic sense; instead it is to be interpreted as the scaling.

with the maximum

$$A^S_{k,m} := \max_r A^S_k(r) = A^S_k(r_m)$$

attained at $r = r_m$.

• the amplitudes $A^w_l(r, \theta)$ and $A^\perp_l(r, \theta)$ of l-th axial Fourier component of wave velocity:

$$A^w_l(r, \theta) = \sqrt{w^{(1)}_l(r, \theta)^2 + w^{(2)}_l(r, \theta)^2} \tag{3.4}$$

$$A^\perp_l(r, \theta) = \sqrt{u^{(1)}_l(r, \theta)^2 + v^{(1)}_l(r, \theta)^2 + u^{(2)}_l(r, \theta)^2 + v^{(2)}_l(r, \theta)^2} \tag{3.5}$$

where l-th axial Fourier component of wave velocity is defined as

$$\begin{pmatrix} u^{(i)}_l(r, \theta) \\ v^{(i)}_l(r, \theta) \\ w^{(i)}_l(r, \theta) \end{pmatrix} = \sum_{\substack{0 \leqslant j \leqslant N \\ 0 \leqslant k \leqslant M}} \begin{pmatrix} u^{(i)}_{jkl} \Phi_j(r; kk_0) \cos kk_0\theta \\ v^{(i)}_{jkl} \Phi_j(r; kk_0) \sin kk_0\theta \\ w^{(i)}_{jkl} \Psi_j(r; kk_0) \cos kk_0\theta \end{pmatrix}$$

when l is even,

$$= \sum_{\substack{0 \leqslant j \leqslant N \\ 0 \leqslant k \leqslant M}} \begin{pmatrix} u^{(i)}_{jkl} \Phi_j(r; kk_0) \sin kk_0\theta \\ v^{(i)}_{jkl} \Phi_j(r; kk_0) \cos kk_0\theta \\ w^{(i)}_{jkl} \Psi_j(r; kk_0) \sin kk_0\theta \end{pmatrix}$$

when l is odd for each $i = 1, 2$.

Also, we define an axial wave amplitude function

$$w_{k,l}(r) = \left\{ \left(\sum_{j=0}^N w^{(1)}_{jkl} \Psi_j(r; kk_0) \right)^2 + \left(\sum_{j=0}^N w^{(2)}_{jkl} \Psi_j(r; kk_0) \right)^2 \right\}^{1/2} \tag{3.6}$$

and corresponding maximum

$$w_{k,l,m} = \max_r w_{k,l}(r) = w_{k,l}(r_m) , \tag{3.7}$$

where r_m is the location of the maximum, when uniquely defined. Figure 24 show roll component sup-norms $\|U\|_\infty$ and $\|V\|_\infty$ and streak sup-norms $\|W\|_\infty$ for two different α as a function of R on a log-log scale. The linear fittings on a log-log scale are based on a best-fit estimate of the data in the regime $5 \times 10^4 < R < 2 \times 10^5$. The scaling for rolls for $C1$ ranges between $R^{-0.74}$ and $R^{-0.77}$; whilst the streak scaling ranges between $R^{-0.34}$ and $R^{-0.38}$. We found a systematic trend for the slope to steepen slightly with increasing α. For instance at $\alpha = 2.51$, observed roll slope is close to $R^{-0.80}$, while the streak slope is $R^{-0.40}$. The roll scaling for $C2$ on the other hand ranges between $R^{-0.78}$ and $R^{-0.79}$, whilst the streak size scaling ranges between $R^{-0.29}$ and $R^{-0.35}$, again with slight dependence on α. At $\alpha = 2.51$, the observed roll slope is about $R^{-0.80}$ and streak slope is $R^{-0.38}$. The maximal streamwise wave amplitude for the l mode, $\|A^w_l\|_\infty$ for $l = 1, 2, 3$ is shown in Figure 25 for two different values of α for both $C1$ and $C2$. Note that the $l = 1$ component for axial wave velocity scales somewhere between $R^{-0.50}$ and $R^{-0.52}$ for $C1$, and $R^{-0.54} - R^{-0.55}$ for $C2$, though the log-log scale also shows that the curves are yet to straighten completely for larger l range, and hence R may not be large enough to reach the asymptotic regime. For $l = 2$, the decay rate is about $R^{-0.51} - R^{-0.60}$

range. For $l = 3$ the apparent scale is $R^{-0.5}$ for $C1$ at $\alpha = 0.624$, while it is $R^{-0.71}$ for $C2$. Note that the different l modes have approximately the same decay rate in R, suggesting that wave nonlinearity is important as $R \to \infty$. In other words, the numerical results do not appear to be consistent with the VWI scenario of a dominating single axial wave mode.

On the other hand, Figure 26 shows the scaling of the wave amplitude $A_l^\perp(r, \theta)$ in the perpendicular plane for $C1$ and $C2$. For $l = 1$, this scaling ranges between $R^{-0.76}$ and $R^{-0.78}$ for both $C1$ and $C2$, while the $l = 2$ mode corresponds to a faster decay rate in both cases; note $l = 3$ curve is not as straight suggesting it is further from reaching its asymptotic limit.

In Figure 27, we plot $A_k^U(r)/A_{k,m}^U$ against r/r_m for the $C1$ solution for two different values of α in (a) and (b). We notice that the curves have almost collapsed into a single graph, as might be expected if a single collapsing scale exists. The collapse is not nearly as good for $k = 3$, apparently because $R \to \infty$ asymptotics is only achieved for larger R when k is larger. Note the decay of the rolls in r/r_m. This is explained asymptotically in §4.3.

Figure 28 displays $A_{k,m}^U$ against R on a $\log - \log$ scale for different values of k for two different values of α in (a) and (b). We notice that for the most dominant mode($k = 2$), the curve is very close to the straight line in the range $5 \times 10^4 < R < 2 \times 10^5$ with the approximate behavior $R^{-0.78}$- $R^{-0.84}$, consistent with the decay rate of $\|U\|_\infty$ observed in Fig. 24. Beyond the most dominant mode, the graphs for other modes have not yet approached a straight line suggesting that R is not large enough to reach the asymptotic scaling regime for larger k. The corresponding radial location $(r = r_m)$, where the max $A_{k,m}^U$ is attained, is shown in Figure 29 through a $\log - \log$ linear fitting in the range $7 \times 10^4 < R < 2 \times 10^5$. Notice that for the largest azimuthal component $(k = 2)$, shown in magenta, r_m scales approximately as $R^{-0.23} - R^{-0.24}$, This is nearly the same for other k values $(k = 1, 3)$ though the curves become linear for larger R.

Figures 30, 31, 32 give the same set of scaling results for the solution branch $C2$. Note however, that the odd values of k are missing from the graph. This is because those components (within small calculation error) are zero since corresponding solution have the Ω_2-symmetry (shift-and-rotate) defined by Pringle *et al*(2009).

Figure 33 shows streak amplitude $A_k^S(r)$ for different R and k with $\alpha = 1.55$ and $\alpha = 0.624$ for the $C1$ solution. It is to be noted that for $k = 0$, we have a very flat profile (see §4.4.2 for theoretical explanation.). Because the roll effect on the streak is more global, $A_k^S(r)$ does not collapse in the same way for different R as do rolls, though for $k \neq 0$, there is a slight tendency of the maximum of the pattern to shift towards the origin for large R.

Figure 34 shows for the $C1$ solution how the maximal streak amplitude $A_{k,m}^S$ scales with R for different azimuthal wave number k , while Figure 35 shows maximal radial location r_m against R. Note $k = 0$ curve is missing since r_m is not well-defined for a flat profile (see Figure 33). The streak amplitude for the dominant $k = 0$ mode scales as $R^{-0.37}$- $R^{-0.33}$, close to the scaling of $\|W\|_\infty$ in Figure 24.

Figure 36 shows streak amplitude function $A_k^S(r)$ for different R and k for $\alpha = 0.624$ and $\alpha = 1.55$ for $C2$ solution. Again for $k = 0$, we again observe a very flat profile.

Figure 37 shows for the $C2$ solution the scaling of maximal streak amplitude $A_{k,m}^S$ with R for different azimuthal wave number k, while Figure 38 shows how the corresponding radial maximal location r_m against with R. Once again $k = 0$ mode data is absent since r_m is ill-defined for a flat profile. The streak amplitude for the most dominant mode $(k = 0)$ scales as $R^{-0.35}$, $R^{-0.28}$ for $\alpha = 1.55, 0.624$ respectively, consistent with the

scaling of $\|W\|_\infty$ in Figure 24. Note that like the $C1$ solution the maximal location r_m is almost independent of R; this feature is explained theoretically in §4.4.1.

Figure 39 shows the collapse of the radial profile of the scaled axial wave amplitude $\frac{w_{k,l}(r)}{w_{k,l,m}}$ against $\frac{r}{r_m}$ (see (3.6)-(3.7)) for $l = 1$ for different k and R for $C2$ solution for $\alpha = 1.55$. A similar collapse was observed for the $C1$ solution and for other l modes. For the radial wave components, the collapse was worse, presumably because of their smaller sizes and limitations in numerical accuracy. However, in all cases, we noted that the location of maximum r_m shifted towards the origin for larger and larger Reynolds number at a rate similar to the collapse rate of rolls. Also note the rapid decay of the solutions with large $\hat{r}$. This is shown to be a general property of all such states in §4.5.

It is to be noted that the streak structure does not collapse with R, not at least at the same rate as rolls and waves, and appears to extend to a region where r/r_m is large. We explain this theoretically in §4.3. This is similar to the streak features observed in boundary layer flows observed by Deguchi and Hall (2014).

To distinguish between a collapsing VWI state, where the wave amplitude is large in a critical layer only and a nonlinear viscous core (NVC) state where axial wave and streak amplitude are of the same order through out a shrinking core similar to the state discovered by Deguchi and Hall (2014) in a different context, we present the contour plots for Reynolds stress. For a NVC state in a pipe (see §4.1, we have a core shrinking as $R^{-1/4}$, with $1 - c = O(R^{-1/2})$. The critical curve defined by $1 - c - r^2 + W(r,\theta) = 0$ has no significance in contrast to a vortex-wave (VWI) state. The Reynolds stresse S_1 and S_2 defined as

$$S_1(r,\theta) = \sqrt{\langle w\frac{\partial u}{\partial z}\rangle^2 + \langle w\frac{\partial v}{\partial z}\rangle^2} \tag{3.8}$$

and

$$S_2(r,\theta) = \sqrt{\langle u\frac{\partial u}{\partial r} + \frac{v}{r}\frac{\partial u}{\partial \theta} - \frac{v^2}{r}\rangle^2 + \langle u\frac{\partial v}{\partial r} + \frac{v}{r}\frac{\partial v}{\partial \theta} + \frac{uv}{r}\rangle^2} \tag{3.9}$$

then determine $S_{j,m} := \max_{(r,\theta)} S_j(r,\theta)$ and corresponding maximal location (r_m, θ_m) in polar coordinates.

Figure 40 shows $S_{1,m}$ and $S_{2,m}$ against R for $\alpha = 0.624$ for the $C1$ and $C2$ solutions. It is clear that $S_{2,m} > S_{1,m}$. Note for the $C1$ solution, $S_{1,m}$, $S_{2,m}$ scale as $R^{-1.27}$, $R^{-1.29}$ respectively, while they scale as $R^{-1.34} - R^{-1.35}$ for $C2$ solution. Similar results for $\alpha = 1.55$ are shown Figure 41. For stress plots, linear fittings involved the range: $5 \times 10^4 < R < 2 \times 10^5$. The red points in Figures 42 and 43 identifies for $C1$ and $C2$ solutions respectively the locations corresponding to (r_m, θ_m) where S_2 attains a maximum. Contour plots of $S_2(r,\theta)$ where $\frac{S_2}{S_{2,m}} = 0.9, 0.8, 0.7, 0.5, 0.3$ are also shown in the same set of figures for different R and α. Though the contours for higher values of $\frac{S_2}{S_{2,m}}$ appear centered about the critical curve (where $1 - c - r^2 + W(r,\theta) = 0$) shown in black, they are far more spread out than expected for a critical curve (See Deguchi and Hall (2014)) leading us to believe that both $C1$-$C2$ solutions are finite R realization of an NVC state, despite the observed difference between empirical $R^{-0.32} - R^{-0.38}$ behavior of $(1-c)$ against the NVC prediction of $(1-c) \sim R^{-1/2}$ (see §4.1). In this context, it may be pointed that $(1-c) \sim R^{-1/3}$ asymptotic prediction of spiral states of Smith and Bodonyi (1982) is not realized accurate in numerical observations until $R \geqslant 10^8$ Therefore, there is reason to believe that the numerical results are yet to reflect the final asymptotic slope. In this context, the observation that $(1 - c)$ versus R curves get steeper for larger α, albeit slightly in the range of R numerically calculated, suggests that this may be the

case since the scaling arguments in §4 for waves suggests that αR is the effective large parameter. This is also the case for the streak amplitude versus R, suggesting that that theoretical streak scaling $R^{-1/2}$ scaling as $R \to \infty$ is yet to be realized for the range of R where accurate computation was feasible. A linear fit of $\log r_m$ against $\log R$, which has not been shown here, suggests $r_m \sim R^{-0.23} - R^{-0.24}$, consistent with the collapse rate exhibited in Figures 29 and 32, and not far from theoretical $R^{-1/4}$ scale predicted asymptotically §4.1.

4. Large R asymptotics for travelling waves

We discuss all possible large R asymptotic structure of travelling waves in a pipe when axial wave number α is independent of R. Assume we have a structure at the center of the pipe of width $\delta \leqslant 1$. $\delta = 1$ corresponds to non-collapsing structure characterized by $1 - c$ not small. We introduce rescaled radial variable $\hat{r}$ so that

$$r = \delta \hat{r} \tag{4.1}$$

Then, on subtracting Poisseiulle flow $(1 - r^2)\hat{\mathbf{z}}$, and decomposing remaining velocity into its axial component and its complement

$$\mathbf{v} = \tilde{w}\hat{\mathbf{z}} + \mathbf{v}_\perp \tag{4.2}$$

it may be checked from the Navier-Stokes equation that $\mathbf{v}$ satisfies

$$\left(1 - c - \delta^2 \hat{r}^2 + \tilde{w}\right)\partial_z \mathbf{v} + \delta^{-1}\left(\mathbf{v}_\perp \cdot \nabla_\perp\right)\mathbf{v} - 2\delta\hat{r}\left(\mathbf{v} \cdot \hat{\mathbf{r}}\right)\hat{\mathbf{z}}$$
$$= -\delta^{-1}\nabla_\perp \tilde{p} - \frac{\partial \tilde{p}}{\partial z}\hat{\mathbf{z}} + \delta^{-2}R^{-1}\Delta_\perp \mathbf{v} + R^{-1}\frac{\partial^2}{\partial z^2}\mathbf{v} \ , \tag{4.3}$$

$$\delta^{-1}\nabla_\perp \cdot \mathbf{v}_\perp + \frac{\partial \tilde{w}}{\partial z} = 0 \tag{4.4}$$

We now introduce scaled variables

$$\mathbf{v}_\perp = \delta_1 \mathbf{U}(\hat{r}, \theta) + \delta_2 \mathbf{u}(\hat{r}, \theta, z) \tag{4.5}$$

where $\mathbf{U}$ is the scaled roll and $\mathbf{u}$ the scaled wave components The decomposition is made unique by requiring axial wave-length average $\langle \mathbf{u} \rangle = 0$. Similarly, we decompose the axial velocity

$$\tilde{w} = \delta_3 W(\hat{r}, \theta) + \delta_4 w(\hat{r}, \theta, z) \ , \tag{4.6}$$

where W is the scaled streak and w is the scaled axial wave velocity. We make the mild assumption that $\delta_2 \delta^{-1}$ is the same order or smaller than δ_3, which without loss of generality† implies

$$\delta_2 \delta^{-1} \leqslant \delta_3 \tag{4.7}$$

As will be seen later, $\delta_4 \leqslant \frac{\delta_2}{\delta}$, and so condition (4.7) requires that the largest possible scale of the wave amplitude in the axial direction does not exceed that for the streak. We make no further *a priori* assumption on the scales, but will systematically derive them from asymptotic consistency as $R \to \infty$. We also decompose the pressure likewise

$$\tilde{p} = \delta_5 P(\hat{r}, \theta) + \delta_6 p(\hat{r}, \theta, z) \tag{4.8}$$

---

† Note replacing any δ by 2δ or similar multiple of δ has no effect on the arguments since this is equivalent to replacing the variable multiplying δ by a constant multiple, which does not affect the argument about existence of solution

	$\alpha = 1.55$		$\alpha = 0.624$	
	C1	C2	C1	C2
δ_c (Fig 22)	0.38	0.37	0.36	0.32
δ_3 (Fig 24)	0.38	0.35	0.34	0.29
δ_1 (Fig 24)	0.77	0.79	0.75	0.80
δ (Figs 29, 32)	0.23	0.23	0.24	0.23
δ_2 (Fig 26)	0.76	0.78	0.76	0.78
δ_4 (Fig 25)	0.52	0.54	0.50	0.55

Table 1: Estimated γ values in a $R^{-\gamma}$ scaling.

and define

$$1 - c = \delta_c c_1 \tag{4.9}$$

where $c_1 = O_s(1)$, *i.e.* strictly order one. The estimated values of δ_c, δ, δ_1-δ_4 on fitting numerically obtained data for R in the interval $\left(5 \times 10^4, 2 \times 10^5\right)$ for $C1,C2$ states are displayed in Table 1.

Now, we return to theoretical arguments on the relation between different δ's and R. On taking axial wavelength average $\langle \cdot \rangle$ of (4.3) and (4.4), the projection of the velocity in the plane orthogonal to z-axis gives

$$\delta^{-1}\delta_1^2 \mathbf{U} \cdot \nabla_\perp \mathbf{U} = -\delta_5 \delta^{-1} \nabla_\perp P + \delta_1 \delta^{-2} R^{-1} \Delta_\perp \mathbf{U} - \delta^{-1}\delta_2^2 \langle \mathbf{u} \cdot \nabla_\perp \mathbf{u} \rangle - \delta_4 \delta_2 \langle w \frac{\partial}{\partial z} \mathbf{u} \rangle \tag{4.10}$$

$$\nabla_\perp \cdot \mathbf{U} = 0 \tag{4.11}$$

In order to enforce divergence condition (4.11), P must appear in the leading order asymptotics in (4.10), implying

$$\delta_5 = \delta_1^2 \ , \tag{4.12}$$

For the solutions with collapsing structure for which $\delta << 1$, we impose property $\mathbf{U} \to 0$ as $\hat{r} \to \infty$ (in the inner radial scale). On the otherhand, for $\delta = 1$, the solution satisfies homogeneous boundary condition $\mathbf{U} = 0$ at $r = 1$. In either case, leading order balance in (4.10) as $R \to \infty$ must involve viscous term since nontrivial solution otherwise. Thus,

$$\delta_1 \delta = R^{-1} \tag{4.13}$$

Using (4.12) and (4.13), (4.10) reduces to

$$\mathbf{U} \cdot \nabla_\perp \mathbf{U} = -\nabla_\perp P + \Delta_\perp \mathbf{U} - \delta_2^2 \delta_1^{-2} \langle \mathbf{u} \cdot \nabla_\perp \mathbf{u} \rangle - \delta_4 \delta \delta_1^{-2} \delta_2 \langle w \partial_z \mathbf{u} \rangle \tag{4.14}$$

We are constrained to choose without any loss of generality

$$\max \left\{ \delta_2, \sqrt{\delta_4 \delta \delta_2} \right\} \geqslant \delta_1 \tag{4.15}$$

since otherwise $\mathbf{U} = O_s(1)$ is inconsisent with homogeneous boundary conditions and

asymptotically small forcing in (4.14)-(4.11) when $R >> 1$. We note that the equality in (4.15) will hold if there is no critical layer and wave magnitude is the same order whenever $\hat{r} = O(1)$. If there is a critical layer of thickness $\hat{\delta} << 1$ in the $\hat{r}$ scale, since wave $(\mathbf{u}, w) = O(\hat{\delta})$ outside the critical layer, then we must have max $\left\{\delta_2^2/\delta_1^2, \delta_4\delta\delta_2/\delta_1^2\right\} >> 1$ in (4.15). In the limit when $\hat{\delta} \to 0$, the forcing reduces to a delta function at the critical curve consistent with $\mathbf{U} = O_s(1)$ in (4.14) provided a constraint between $\hat{\delta}, \delta_2, \delta_1$ is satisfied; this will be discussed in §4.2.

Consider now the axial component of $\mathbf{v}$ in (4.3). Using (4.5)-(4.6), we obtain by axial averaging $\langle\cdot\rangle$ and using (4.13), the following equation for streak:

$$\mathbf{U} \cdot \nabla_\perp W = \Delta_\perp W + \frac{\delta^2}{\delta_3} 2\hat{r}U_1 - \frac{\delta_2\delta_4}{\delta_1\delta_3}\langle\mathbf{u} \cdot \nabla_\perp w\rangle \tag{4.16}$$

Requring solution $W = O_s(1)$ in (4.16) with homogeneous boundary condition implies that either the roll or wave term enters into the equation at the leading order, *i.e.*

$$\delta_3 = \delta^2 \quad , \quad \text{or} \quad \frac{\delta_2\delta_4}{\delta_1\delta_3} \geqslant 1, \delta^2 \leqslant \delta_3 \tag{4.17}$$

where the latter possibility will be ruled out in the ensuing discussions. Consider now the equation for the wave $(\mathbf{u}, w)$ defined uniquely by the property $\langle(\mathbf{u}, w)\rangle = 0$, where $\mathbf{u}$ is the projection in the perpendicular plane, with radial and azimuthal components (u, v) From the axial component of (4.3), using (4.5),(4.6), (4.13) and (4.16), we obtain

$$\left(\delta_c c_1 - \delta^2\hat{r}^2 + \delta_3 W + \delta_4 w\right)\partial_z w + \delta_1\delta^{-1}\left(\mathbf{U}\cdot\nabla_\perp\right)w + \delta_2\delta^{-1}\mathbf{u}\cdot\nabla_\perp w$$
$$= -\frac{\delta_2}{\delta\delta_4}\mathbf{u}\cdot\nabla_\perp\left(-\delta^2\hat{r}^2 + \delta_3 W\right) - \frac{\delta_6}{\delta_4}\frac{\partial p}{\partial z} + \delta^{-2}R^{-1}\Delta_\perp w + R^{-1}\partial_z^2 w + \delta_2\delta^{-1}\langle\mathbf{u}\cdot\nabla_\perp w\rangle ,$$
$$\tag{4.18}$$

For the components of the wave perpendicular to the cylinder, (4.3), with (4.5),(4.6), (4.13) and (4.14) imply

$$\left(\delta_c c_1 - \delta^2\hat{r}^2 + \delta_3 W + \delta_4 w\right)\partial_z\mathbf{u} + \delta_1\delta^{-1}\left(\mathbf{U}\cdot\nabla_\perp\right)\mathbf{u} + \delta_1\delta^{-1}\left(\mathbf{u}\cdot\nabla_\perp\right)\mathbf{U}$$
$$+ \delta_2\delta^{-1}\mathbf{u}\cdot\nabla_\perp\mathbf{u} = -\frac{\delta_6}{\delta_2\delta}\nabla_\perp p + \delta^{-2}R^{-1}\Delta_\perp\mathbf{u} + R^{-1}\partial_z^2\mathbf{u} + \delta_2\delta^{-1}\langle\mathbf{u}\cdot\nabla_\perp\mathbf{u}\rangle + \delta_4\langle w\partial_z\mathbf{u}\rangle ,$$
$$\tag{4.19}$$

together with the divergence condition (4.4), which now implies:

$$\nabla_\perp \cdot \mathbf{u} + \frac{\delta_4\delta}{\delta_2}\frac{\partial w}{\partial z} = 0 \tag{4.20}$$

It is clear that without any loss of generality,

$$\delta_4 \leqslant \frac{\delta_2}{\delta} \tag{4.21}$$

as otherwise the leading order divergence equation would imply w to be independent of z, which from $\langle w\rangle = 0$ implies $w = 0$, which is inconsistent. Also, note that with condition (4.15) and (4.21), implies

$$\delta_2 \geqslant \delta_1 \tag{4.22}$$

The parameter c_1 in the system of equations (4.18)-(4.20) must appear in the leading order equation since it acts as a eigenvalue for nonzero solution to a system of homogeneous equations for $(\mathbf{u}, w)$ with homogenous boundary conditions. Furthermore, the pressure

must come into the leading order balance in (4.19) as otherwise one cannot satisfy (4.20). Next the term $\delta^2 \hat{r}^2 + \delta_3 W$ must appear in the leading order balance as otherwise using

$$\frac{1}{R\delta^2} = \delta_1\delta^{-1} \leqslant \delta_2\delta^{-1} \leqslant \delta_3 << \delta_c$$

the resulting leading order equations $c_1\partial_z w = -\delta^2\partial_z \tilde{p}$, $c_1\partial_z \mathbf{u} = -\nabla_\perp \tilde{p}$ (for some rescaled pressure $\tilde{p}$), together with (4.20) has no nontrivial solution. Thus, $\delta_c = O_s(\delta_3)$ since the possibility $\delta_3 << \delta^2$ is ruled out in (4.17). Therefore, without any loss of generality, we have

$$\delta_c = \delta_3 \qquad (4.23)$$

Other terms appearing in each of (4.18)-(4.19) have to be the same or lower order than this term. For pressure term to appear to the leading order in (4.18), as it must,

$$\delta_6 = \delta_2\delta\delta_3 \qquad (4.24)$$

Further, all the other terms appearing in each of (4.18) and (4.19) cannot be any larger than δ_c (or δ_3), which on using (4.13), (4.21), (4.22) and (4.24) implies without any loss of generality

$$\frac{1}{R\delta^2} = \delta_1\delta^{-1} \leqslant \delta_2\delta^{-1} \leqslant \delta_3 \ , \quad \delta^2 \leqslant \delta_3 \ , \quad \text{and} \quad \frac{\delta_3\delta_2}{\delta\delta_4} \leqslant \delta_3 \qquad (4.25)$$

Note that the last inequality gives $\delta_4 \geqslant \frac{\delta_2}{\delta}$, which together with (4.21) implies

$$\delta_4 = \frac{\delta_2}{\delta} \qquad (4.26)$$

Using (4.22), (4.23), (4.26) and (4.24), we may rewrite (4.18)-(4.20) as

$$\left(c_1 - \frac{\delta^2}{\delta_3}\hat{r}^2 + W + \frac{\delta_2}{\delta\delta_3}w\right)\partial_z w + \frac{1}{R\delta^2\delta_3}\left(\mathbf{U}\cdot\nabla_\perp\right)w + \frac{\delta_2}{\delta\delta_3}\mathbf{u}\cdot\nabla_\perp w + \mathbf{u}\cdot\nabla_\perp\left(W - \frac{\delta^2}{\delta_3}\hat{r}^2\right)$$

$$= -\delta^2\frac{\partial p}{\partial z} + \frac{1}{R\delta^2\delta_3}\Delta_\perp w + \frac{1}{R\delta_3}\partial_z^2 w + \frac{\delta_2}{\delta\delta_3}\langle\mathbf{u}\cdot\nabla_\perp w\rangle \quad (4.27)$$

$$\left(c_1 - \frac{\delta^2}{\delta_3}\hat{r}^2 + W + \frac{\delta_2}{\delta\delta_3}w\right)\partial_z \mathbf{u} + \frac{1}{R\delta^2\delta_3}\left(\mathbf{U}\cdot\nabla_\perp\right)\mathbf{u} + \frac{1}{R\delta^2\delta_3}\left(\mathbf{u}\cdot\nabla_\perp\right)\mathbf{U}$$

$$+ \frac{\delta_2}{\delta\delta_3}\mathbf{u}\cdot\nabla_\perp\mathbf{u} = -\nabla_\perp p + \frac{1}{R\delta^2\delta_3}\Delta_\perp\mathbf{u} + \frac{1}{R\delta_3}\partial_z^2\mathbf{u} + \frac{\delta_2}{\delta\delta_3}\langle\mathbf{u}\cdot\nabla_\perp\mathbf{u}\rangle + \frac{\delta_2}{\delta\delta_3}\langle w\partial_z\mathbf{u}\rangle \ ,$$

$$(4.28)$$

$$\nabla_\perp\cdot\mathbf{u} + \frac{\partial w}{\partial z} = 0 \qquad (4.29)$$

There are now two distinct possibilities:

$$\text{(i)} \ \frac{1}{R\delta^2\delta_3} = 1 \quad , \quad \text{(ii.)} \ \frac{1}{R\delta^2\delta_3} << 1 \qquad (4.30)$$

4.1. Case (i): $\frac{1}{R\delta^2\delta_3} = 1$, (Nonlinear Viscous Core (NVC))

If we assume (i), then it follows from (4.23) and (4.25) that

$$\frac{1}{R\delta^2} = \frac{\delta_1}{\delta} = \frac{\delta_2}{\delta} = \delta_3 = \delta_c \qquad (4.31)$$

With the above scaling, and (4.26), the equations for rolls, streaks and waves from (4.14), (4.16), (4.27)- (4.28) become

$$\mathbf{U} \cdot \nabla_\perp \mathbf{U} = -\nabla_\perp P + \Delta_\perp \mathbf{U} - \langle \mathbf{u} \cdot \nabla_\perp \mathbf{u} \rangle - \langle w \partial_z \mathbf{u} \rangle \tag{4.32}$$

$$\mathbf{U} \cdot \nabla_\perp \left(W - R\delta^4 \hat{r}^2 \right) = \Delta_\perp W - \langle \mathbf{u} \cdot \nabla_\perp w \rangle \tag{4.33}$$

$$\left(c_1 - R\delta^4 \hat{r}^2 + W + w \right) \partial_z w + \left(\mathbf{U} \cdot \nabla_\perp \right) w + \mathbf{u} \cdot \nabla_\perp w + \mathbf{u} \cdot \nabla_\perp \left(W - R\delta^4 \hat{r}^2 \right)$$
$$= -\delta^2 \frac{\partial p}{\partial z} + \Delta_\perp w + \delta^2 \partial_z^2 w + \langle \mathbf{u} \cdot \nabla_\perp w \rangle \tag{4.34}$$

$$\left(c_1 - R\delta^4 \hat{r}^2 + W + w \right) \partial_z \mathbf{u} + \left(\mathbf{U} \cdot \nabla_\perp \right) \mathbf{u} + \left(\mathbf{u} \cdot \nabla_\perp \right) \mathbf{U}$$
$$+ \mathbf{u} \cdot \nabla_\perp \mathbf{u} = -\nabla_\perp p + \Delta_\perp \mathbf{u} + \delta^2 \partial_z^2 \mathbf{u} + \langle \mathbf{u} \cdot \nabla_\perp \mathbf{u} \rangle + \langle w \partial_z \mathbf{u} \rangle \;, \tag{4.35}$$

along with divergence conditions (4.11) and (4.29). Note that on using (4.31), (4.17), implies

$$R\delta^4 \leqslant 1 \tag{4.36}$$

In this case, viscosity and nonlinearity come at the same order in a coupled system of roll, streak and wave equations above. The distinguished scale in (4.32)- (4.35) is clearly

$$\delta = R^{-1/4} \tag{4.37}$$

since it brings the Poisseuille term deviation from 1 of axial velocity at the same order as W and allows far-field matching. to Pouisseuille flow. With this choice of δ, we obtain from (4.26) and (4.31)

$$\delta_1 = R^{-3/4} = \delta_2 \quad , \qquad \delta_3 = R^{-1/2} = \delta_4 \;, \quad \delta_c = R^{-1/2} \tag{4.38}$$

Since (4.32)- (4.35) with $R\delta^4 = 1$ is a completely coupled system of roll, streak and wave equations, it is not necessary to separate roll, streak and wave components to obtain parameter free leading order asymptotic equations. One can directly look for travelling wave solutions to (4.3) using the scales in (4.38):

$$1 - c = R^{-1/2} c_1 \quad , \mathbf{v} = \tilde{w}\hat{\mathbf{z}} + \mathbf{v}_\perp \;, \tag{4.39}$$

$$\tilde{w} = R^{-1/2}\hat{w} \;, \quad \mathbf{v}_\perp = R^{-3/4}\hat{\mathbf{v}}_\perp \quad , \text{ and } \; \tilde{p} = R^{-3/2}\hat{p} \tag{4.40}$$

This gives rise to a parameter-free canonical nonlinear eigenvalue problem presented in §4.6. The far-field conditions on different azimuthal Fourier components are readily deduced from discussions in §(4.3)- §(4.5). Unlike roll and wave components, we find the remarkable feature that certain azimuthal streak components do not decay as $\hat{r} \to \infty$. This is similar to what was observed earlier by Deguchi and Hall (2014) in a different context.

4.2. *Case* (ii): $\frac{1}{R\delta^2 \delta_3} << 1$ *(VWI: Vortex Wave Interacting states)*

We now consider consider full implications of assumption (ii). *Apriori*, this involves two sub-cases (ii.a) $\frac{\delta_2}{\delta} = \delta_3$ with $(\mathbf{u}, w) = O_s(1)$ when $\hat{r} = O_s(1)$, *i.e.* there is no critical layer phenomena in the scaled $(\hat{r}, \theta)$ variables and wave nonlinearity is important everywhere in this region; and case (ii.b) where $(\mathbf{u}, w) << 1$ outside a critical layer of thickness $\hat{\delta} << 1$ (in the $\hat{r}$ variable) in the vicinity of the critical curve. In case (ii.a), the only choice of distinguished scale in δ that brings viscous term to the same order as nonlinearity corresponds to $\frac{1}{R\delta^2 \delta_3} = 1$, which is the case already discussed in (i).

Therefore, we are only left case (**ii.b**). It is clear that (4.27)-(4.28) reduces to the following leading order linear wave equations except in a neighborhood of $\mu = 0$ where

$$\mu := c_1 - \frac{\delta^2}{\delta_3}\hat{r}^2 + W \tag{4.41}$$

$$\left(c_1 - \frac{\delta^2}{\delta_3}\hat{r}^2 + W\right)\partial_z w + \mathbf{u}\cdot\nabla_\perp\left(W - \frac{\delta^2}{\delta_3}\hat{r}^2\right) = -\delta^2\frac{\partial p}{\partial z} \ , \tag{4.42}$$

$$\left(c_1 - \frac{\delta^2}{\delta_3}\hat{r}^2 + W\right)\partial_z\mathbf{u} = -\nabla_\perp p \ , \tag{4.43}$$

It is possible to eliminate $\mathbf{u}$ and w altogether from (4.42)-(4.43) using (4.29) and the following Rayleigh-equation for pressure to the leading order outside the critical layer:

$$\nabla_\perp\cdot\left(\frac{\nabla_\perp p}{(c_1 - \frac{\delta^2}{\delta_3}\hat{r}^2 + W)^2}\right) + \frac{\delta^2}{(c_1 - \frac{\delta^2}{\delta_3}\hat{r}^2 + W)^2}\frac{\partial^2 p}{\partial z^2} = 0 \tag{4.44}$$

It is known that when the critical curve is approached, the inviscid $(\mathbf{u}, w)$ blows up like the distance from the critical curve. More precisely $\mathbf{u}\cdot\mathbf{e}_s$ and w blows up like $\frac{1}{\mu}$. Note that the scales δ_2 and $\delta_4 = \frac{\delta_2}{\delta}$ for perpendicular components $\mathbf{u} = (u, v)$ and axial components w is based on the maximal value that these attain anywhere in the domain; in particular this is based on their sizes in the critical layer, if there is one. Outside the critical layer, they must drop by a factor of $\hat{\delta}$, *i.e.*

$$(\mathbf{u}, w) = O(\hat{\delta}) \text{ outside the critical} - \text{layer} \tag{4.45}$$

Using (4.21), this implies that the size of the forcing in the Roll equation (4.14) is $\frac{\delta_2^2}{\delta_1^2} \gg 1$ inside the critical curve of width $\hat{\delta}$, where as it is $O\left(\frac{\delta_2^2}{\delta_1^2}\hat{\delta}^2\right)$ outside the critical layer. Therefore, in the asymptotic limit $R \to \infty$, when critical layer thickness $\hat{\delta} \to 0$, the forcing is in the form $\delta_2^2\delta_1^{-2}\mathbf{F}\left([\mathbf{x} - \mathbf{X}_c(s)]/\hat{\delta}\right)$, which reduces to a delta function at the critical curve $\mathbf{X}_c(s)$ provided

$$\frac{\delta_2^2}{\delta_1^2} = \frac{1}{\hat{\delta}} \ , \quad \text{or} \quad \delta_2 = \delta_1\hat{\delta}^{-1/2} \tag{4.46}$$

Now consider the appropriate expression for critical layer thickness $\hat{\delta}$ where the inviscid linear wave equation has to be modified. Within the layer, $\mu = O(\hat{\delta})$, where as nonlinear terms are of size $\hat{\delta}^{-1}\delta_2\delta^{-1}\delta_3^{-1}$ and viscous terms are $O\left(\hat{\delta}^{-2}\left(R\delta_3\delta^2\right)^{-1}\right)$ Viscous effects are brought to the same order as inviscid term when we assume

$$\hat{\delta} = \delta_3^{-1/3}\delta^{-2/3}R^{-1/3} \tag{4.47}$$

If we brought nonlinearity to the leading order within the critical layer, then we are forced to assume $\hat{\delta} = \left(\delta_2\delta^{-1}\delta_3^{-1}\right)^{1/2}$, which on using (4.46), (4.13) implies $\hat{\delta} = \left(R\delta^2\delta_3\right)^{-2/5}$ which is far smaller than the expression in (4.47). Therefore, as we approach the critical layer, viscous effects show up before any possible nonlinear effect and the correct expression for critical layer thickness is given by (4.47). This also implies wave nonlinearity to be small in the critical layer. Note that (4.46) and (4.47), together with (4.13) implies

$$\delta_2 = \delta_1\hat{\delta}^{-1/2} = R^{-5/6}\delta_3^{1/6}\delta^{-2/3} \tag{4.48}$$

Thus, using (4.13), (4.26), and (4.48), (4.14) and (4.16) reduces to

$$\mathbf{U}\cdot\nabla_\perp\mathbf{U} = -\nabla_\perp P + \Delta_\perp\mathbf{U} - R^{1/3}\delta^{2/3}\delta_3^{1/3}\langle\mathbf{u}\cdot\nabla_\perp\mathbf{u}\rangle - R^{1/3}\delta^{2/3}\delta_3^{1/3}\langle w\partial_z\mathbf{u}\rangle \,, \text{and } \nabla_\perp\cdot\mathbf{U} = 0 \tag{4.49}$$

$$\mathbf{U}\cdot\nabla_\perp W = \Delta_\perp W + \frac{\delta^2}{\delta_3}2\hat{r}U_1 - \left(\frac{1}{R\delta^2\delta_3}\right)^{2/3}\langle\mathbf{u}\cdot\nabla_\perp w\rangle \tag{4.50}$$

With the assumption in this case, it is clear that the wave averaged term $\langle\cdot\rangle = o(1)$ in (4.50). Therefore, it is clear from the streak equation $W = O_s(1)$ implies

$$\delta_3 = \delta^2 \tag{4.51}$$

Therefore, from the scale information gathered thus far, we have

$$\mathbf{v}_\perp = \delta^{-1}R^{-1}\mathbf{U}(\hat{r},\theta) + R^{-5/6}\delta^{-1/3}\mathbf{u}(\hat{r},\theta,z) \tag{4.52}$$

$$\tilde{w} = \delta^2 W(\hat{r},\theta) + R^{-5/6}\delta^{-4/3}w(\hat{r},\theta,z) \tag{4.53}$$

$$\tilde{p} = R^{-2}\delta^2 P(\hat{r},\theta) + R^{-5/6}\delta^{8/3}p(\hat{r},\theta,z) \tag{4.54}$$

and

$$1 - c = \delta^2 c_1 \tag{4.55}$$

From (4.48) and (4.51) , the critical layer thickness in the $\hat{r}$ variable becomes

$$\hat{\delta} = \left(R\delta^4\right)^{-1/3} \tag{4.56}$$

Note that δ thus far is arbitrary except that (4.51) and $\frac{1}{R\delta_3\delta^2} \ll 1$ implies

$$\delta \gg R^{-1/4} \tag{4.57}$$

The restriction on δ when $\delta \ll 1$ arises from higher order solvability as will be seen shortly. With the scalings derived thus far, from definitions of Reynolds stress S_1 and S_2 in (3.8)-(3.9), it follows that

$$S_1, S_2 = O_s\left(R^{-5/3}\delta^{-5/3}\right) \tag{4.58}$$

Using the scalings inferred in (4.52)-(4.55), we may re-write (4.27)- (4.28) as

$$\mu\partial_z w + \mathbf{u}\cdot\nabla_\perp\mu - \epsilon\Delta_\perp w = F_3 \,, \tag{4.59}$$

$$\mu\partial_z\mathbf{u} + \nabla_\perp p - \epsilon\Delta_\perp\mathbf{u} = \mathbf{F} \,, \tag{4.60}$$

where

$$\epsilon = \frac{1}{R\delta^4} \quad, \quad \mu = c_1 - \hat{r}^2 + W \tag{4.61}$$

$$F_3 = -\delta^2\partial_z p - \epsilon\mathbf{U}\cdot\nabla_\perp w - \epsilon^{5/6}\left[\mathbf{u}\cdot\nabla_\perp w + w\partial_z w - \langle\mathbf{u}\cdot\nabla_\perp w\rangle\right] + \epsilon\delta^2\partial_z^2 w \tag{4.62}$$

$$\mathbf{F} = -\epsilon\mathbf{U}\cdot\nabla_\perp\mathbf{u} - \epsilon^{5/6}\left[\mathbf{u}\cdot\nabla_\perp\mathbf{u} + w\partial_z\mathbf{u} - \langle\mathbf{u}\cdot\nabla_\perp\mathbf{u} + w\partial_z\mathbf{u}\rangle\right] + \epsilon\delta^2\partial_z^2\mathbf{u} \tag{4.63}$$

It is convenient to define $\mathbf{X} = (\mathbf{u}, w)$, which is in the space of divergence free functions, satisfying zero boundary conditions, Note that the full equations (4.59)-(4.60), without any approximation, may be compactly written as

$$\mathcal{L}\mathbf{X} = \mathbf{R} \tag{4.64}$$

where $\mathbf{R} = (\mathbf{F}, F_3)$, and the projection $[\mathcal{L}\mathbf{X}]_\perp$ is given by left hand side of (4.60), while the axial component of $[\mathcal{L}\mathbf{X}]_\parallel$ is given by (4.59). Note that the pressure p, upto an unimportant additive constant, is implicitly determined in terms of $\mathbf{X}$ by requiring $\mathbf{X}$

to be divergence free. We define space of functions $\{\mathbf{Y}\}$, where $\mathbf{Y} = (\tilde{\mathbf{u}}, \tilde{w})$ satisfies zero boundary condition, and is dual to the space of functions $\{\mathbf{X}\}$ through the non-degenerate pairing

$$(\mathbf{Y}, \mathbf{X}) = \int_\Omega (\tilde{\mathbf{u}}^* \cdot \mathbf{u} + \tilde{w}^* w) \, dV \tag{4.65}$$

where Ω is the domain inside cylinder domain truncated to a z-period. It is not difficult to note that the adjoint $\mathcal{L}^\dagger$ defined so that its projection in the perpendicular plane and along the pipe axis are defined by

$$\left[\mathcal{L}^\dagger \mathbf{Y}\right]_\perp = -\mu \partial_z \tilde{\mathbf{u}} - \epsilon \Delta_\perp \tilde{\mathbf{u}} - \mu \nabla_\perp \tilde{w} + \nabla_\perp q \tag{4.66}$$

and the axial component of $\left[\mathcal{L}^\dagger \mathbf{Y}\right]_\parallel$ is given by

$$\left[\mathcal{L}^\dagger \mathbf{Y}\right]_\parallel = -2\mu \partial_z \tilde{w} - \epsilon \Delta_\perp \tilde{w} + \partial_z q \tag{4.67}$$

where the dual space is constrained by the two dimensional divergence equation

$$\nabla_\perp \cdot \tilde{\mathbf{u}} = 0 \;, \tag{4.68}$$

which determines q in terms of $(\tilde{\mathbf{u}}, \tilde{w})$ upto a constant. Noting the scaling (4.45) of the waves outside the critical layer of thickness $\hat{\delta}$ given by (4.47), it follows that the contribution of waves to F_3 and $\mathbf{F}$ given in (4.62)-(4.63) is relatively small and to the leading order, we have the linear eigenvalue problem

$$\mathcal{L}\mathbf{X} = 0 \tag{4.69}$$

Without loss of generality, we may seek leading order solution in the form

$$\mathbf{X} = e^{i\alpha z}\left(\mathbf{u}^{(0)}, \mathbf{w}^{(0)}\right) + C.C. \tag{4.70}$$

Note that $\epsilon \Delta_\perp$ term is retained in $\mathcal{L}$ to provide a uniformly valid representation as $\epsilon \to 0$ in the critical and boundary layers. It is convenient to denote the leading order eigenvalue and eigenvectors as $(c_{1,0}, \mathbf{X}^{(0)})$ which itself will have an asymptotic expansion in ϵ, which poses no problem in the following argument. The behavior of $\mathbf{X}^{(0)}$ outside the critical and boundary layers is invisid to the leading order and given by

$$\mathbf{X}^{(0)} \sim \hat{\delta} e^{i\alpha z}\left(\mathbf{u}^{(I)}, w^{(I)}\right) + C.C. \tag{4.71}$$

where they satisfy

$$i\alpha \mu_0 \mathbf{u}^{(I)} = -\nabla_\perp p^{(I)} \tag{4.72}$$

$$i\alpha \mu_0 w^{(I)} = -\mathbf{u}^{(I)} \cdot \nabla_\perp \mu \tag{4.73}$$

$$\nabla_\perp \cdot \mathbf{u}^{(I)} + i\alpha w^{(I)} = 0 \tag{4.74}$$

where

$$\mu_0 = c_{1,0} - \hat{r}^2 + W \tag{4.75}$$

It is possible to eliminate $(\mathbf{u}^{(I)}, w^{(I)})$ from (4.72)-(4.74) in terms scaled pressure which satisfies the Rayleigh equation

$$\nabla_\perp \cdot \left(\frac{\nabla_\perp p^{(I)}}{\mu_0^2}\right) = 0 \tag{4.76}$$

Within the inviscid approximation, appropriate boundary condition for $p^{(I)}$ inhertied from $\mathbf{u}^{(I)} \cdot \hat{\mathbf{r}} = 0$ at the wall, would require

$$\partial_r p^{(I)}(\delta^{-1}, \theta) = 0 \tag{4.77}$$

The Rayleigh problem can also be posed in a slightly more convenient manner by introducing conjugate variable Φ so that

$$-i\alpha\mu_0 u^{(I)} = \partial_{\hat{r}}p^{(I)} = \frac{\mu_0^2}{\hat{r}}\partial_\theta\Phi \ , -i\alpha\hat{r}\mu_0 v^{(0)} = \partial_\theta p^{(0)} = -\hat{r}\mu_0^2\partial_{\hat{r}}\Phi \qquad (4.78)$$

Then, Φ satisfies the elliptic equation

$$\nabla_\perp \cdot \left(\mu_0^2\nabla_\perp\Phi\right) = 0 \qquad (4.79)$$

with wall boundary conditions now translating to Dirichlet condition

$$\Phi(\delta^{-1}, \theta) = 0 \qquad (4.80)$$

From this, it easy to see, when the critical curve is approached, *i.e.* $\mu_0 \to 0$, then the component of wave velocity tangent to the critical curve $\mathbf{u}^{(I)}\cdot\mathbf{e}_s$ blows up as $\frac{1}{\mu_0}$ while $\mathbf{e}_s \cdot \nabla_\perp p^{(I)} = O(1)$, while the normal component $\mathbf{e}_N \cdot \nabla_\perp p^{(I)} = O(\mu_0)$. Also from the inviscid equation (4.73) for $w^{(I)}$, it follows that $w^{(I)}$ also blows up as μ_0^{-1}. This information allows one to construct inner-equation when $\mu_0 = O(\hat{\delta}) = O(\epsilon^{1/3})$ where $\mathbf{e}_s \cdot \mathbf{u}^{(I)}, w^{(I)} = O(\hat{\delta}^{-1}) = \epsilon^{-1/3}$, implying from (4.71) and matching with inner solution representation in terms of Airy functions that $\mathbf{X}^{(0)}$ must be $O(1)$ in the critical layer, while $\mathbf{X}^{(0)} = O(\epsilon^{1/3})$ outside. There is also a boundary layer at the walls where inviscid behavior of $\mathbf{X}^{(0)}$ is modified, but this does not play a role in the argument below since waves decay fast in $\hat{r}$ (see §4.5) and therefore, the wall boundary layer for waves is weak. Note that the leading order analysis does not constrain δ or α. For this, higher order correction needs to be included.

It is convenient to expand $\mathbf{X}$ and corresponding scaled wave speed c_1:

$$\mathbf{X} = \mathbf{X}^{(0)} + \mathbf{X}^{(1)} + \cdots \ , \quad c_1 = c_{1,0} + c_{1,1} + \cdots \qquad (4.81)$$

Aside from assuming that $\mathbf{X}^{(1)} << \mathbf{X}^{(0)}, c_{1,1} << c_{1,0}$, it is convenient not to assume particular scalings in higher order correction at this stage. Then, it is clear from ((4.64)) that $\mathbf{X}^1$ satisfies

$$\mathcal{L}^{(0)}\mathbf{X}^{(1)} = \mathbf{R}^{(0)} - c_{1,1}\partial_z\mathbf{X}^{(0)} \ , \qquad (4.82)$$

where $\mathcal{L}^{(0)}$ is the operator $\mathcal{L}$ with $\mu = \mu_0$ and

$$\left[\mathbf{R}^{(0)}\right]_\perp = \mathbf{F}^{(0)} = e^{i\alpha z}\left(-\epsilon\mathbf{U}\cdot\nabla_\perp\mathbf{u}^{(0)} - \epsilon\alpha^2\delta^2\mathbf{u}^{(0)}\right)$$
$$- \epsilon^{5/6}e^{2i\alpha z}\left(\mathbf{u}^{(0)}\cdot\nabla_\perp\mathbf{u}^{(0)} + i\alpha w^{(0)}\mathbf{u}^{(0)}\right) + C.C. \quad (4.83)$$

$$\left[\mathbf{R}^{(0)}\right]_\parallel = F_3^{(0)} = e^{i\alpha z}\left(-i\alpha\delta^2 p^{(0)} - \epsilon\mathbf{U}\cdot\nabla_\perp w^{(0)} - \epsilon\delta^2\alpha^2 w^{(0)}\right)$$
$$- \epsilon^{5/6}e^{2i\alpha z}\left(\mathbf{u}^{(0)}\cdot\nabla_\perp w^{(0)} + i\alpha[w^{(0)}]^2\right) + C.C. \quad (4.84)$$

Solvability condition†

$$c_{1,1}\left(\mathbf{Y}, \partial_z\mathbf{X}^{(0)}\right) = \left(\mathbf{Y}, \mathbf{R}^{(0)}\right) \qquad (4.85)$$

where $\mathbf{Y} = (\tilde{\mathbf{u}}, \tilde{w})$ is any solution to the the adjoint problem

$$\mathcal{L}^\dagger\mathbf{Y} = 0 \qquad (4.86)$$

† We are assuming, as expected, that the null space of $\mathcal{L}^\dagger$ is orthogonal to the range of $\mathcal{L}$.

with $\mu = \mu_0$ whose perpendicular and parallel projections are defined by (4.66) and (4.67). We now look at the null space of $\mathcal{L}^\dagger$.

The leading order behavior of solution to $\mathcal{L}^\dagger \mathbf{Y} = 0$ as $\epsilon \to 0$ is discussed in the Appendix §8.1. It emerges that if we rescaled variables so that $\mathbf{Y} = (\tilde{\mathbf{u}}, \tilde{w}) = O_s(1)$ inside the critical layer of thickness $\hat{\delta} = \epsilon^{1/3}$, then outside the critical layer,

$$\mathbf{Y} = (\tilde{\mathbf{u}}, \tilde{w}) = O(\hat{\delta}^2) = O(\epsilon^{2/3}) \tag{4.87}$$

Now, we are ready to estimate the terms on the left and right side of (4.85). Because of (4.87) and (4.45), with $\hat{\delta} = \epsilon^{1/3}$, it follows that the contribution from outside the critical layer to $\left(\mathbf{Y}, \partial_z \mathbf{X}^{(0)}\right)$ is $O(\epsilon)$ which is far smaller than the $O(\epsilon^{1/3})$ contribution from the critical layer, noting the integrand to be $O_s(1)$ and the thickness to be $O(\hat{\delta}) = O(\epsilon^{1/3})$. Therefore

$$\left(\mathbf{Y}, \partial_z \mathbf{X}^{(0)}\right) = O_s(\epsilon^{1/3}) \tag{4.88}$$

Now, we consider the scaling of the right hand side in (4.85). We note that inside the critical layer, $\mathbf{U} \cdot \mathbf{e}_s = O(1)$ and $\mathbf{U} \cdot \mathbf{e}_N = O(\hat{\delta}) = O(\epsilon^{1/3})$, which follows from continuity equation (4.11). Therefore,

$$\langle e^{-i\alpha z} \left[\mathbf{R}^{(0)}\right]_\perp \rangle = -\epsilon \mathbf{U} \cdot \nabla_\perp \mathbf{u}^{(0)} = O(\epsilon) \ , \tag{4.89}$$

whereas it is $O(\epsilon^{4/3})$ outside the layer. On the other hand, we have inside the critical layer

$$\langle e^{-i\alpha z} \left[\mathbf{R}^{(0)}\right]_\parallel \rangle = -i\alpha\delta^2 p^{(0)} - \epsilon \mathbf{U} \cdot \nabla_\perp w^{(0)} = O\left(\delta^2, \epsilon\right) \tag{4.90}$$

where as outside it is $O(\delta^2, \epsilon^{4/3})$. Note that the pressure term outside remains the same order as inside the critical layer. Therefore, from expression of the inner-product, it follows that

$$\left(\mathbf{Y}, \mathbf{R}^{(0)}\right) = O\left(\delta^2 \epsilon^{1/3}, \epsilon^{4/3}\right) \tag{4.91}$$

being dominated by the contribution from the critical layer. It follows (4.85) that $c_{1,1} = O\left(\delta^2, \epsilon\right)$, with $O(\delta^2)$ term including α dependence, where as there is on α dependence in $O(\epsilon)$ term. Note that this calculation must result in

$$\Im c_{11} = 0 \tag{4.92}$$

With the normalization already chosen, the complex coefficients of δ^2 and ϵ on the right hand side of (8.27) are completely determined† by the eigensolutions of the leading order equation both for the the original as well as adjoint problems. Therefore, the only generic way in which (8.28) can be enforced is by requiring

$$\delta^2 = \epsilon = \frac{1}{R\delta^4} \ , \quad \text{implying} \quad \delta = R^{-1/6} \tag{4.93}$$

Note that from the same equation, since α appears together with δ^2 in the $O(\delta^2)$ term, the constraint (8.28) also constrains α.

4.3. Far-Field analysis for Rolls

Now, we seek to determine consistent asymptotic behavior of rolls $\mathbf{U}$ for large $\hat{r}$. This will be used in the following section to confirm that streak terms do not decay with $\hat{r}$, explaining the numerical observation that for $C1 - C2$ states, streaks do not have the

† We are assuming, as might be expected, the non-degeneracy of the eigenvalues.

collapsing structure as $R \to \infty$ as do rolls and waves. The ensuing argument is restricted to flows where the rolls have m_0-fold azimuthal symmetry for $m_0 = 2$ or 4, corresponding to the $C1$ and $C2$ solutions computed numericaly. Also, it is to be noted that the same analysis is valid for nonlinear viscous core (NVC) states, *i.e.* when $\delta = R^{-1/4}$ in the regime $\delta^{-1} >> \hat{r} >> 1$.

Using $\delta_3 = \delta^2$ in (4.49) and taking the curl $\nabla_\perp \times$, we get the two dimensional roll-vorticity equation:

$$\Delta_\perp \omega = \mathbf{U} \cdot \nabla_\perp \omega + \left(R\delta^4\right)^{1/3} \hat{\mathbf{z}} \cdot \left(\nabla_\perp \times \langle \mathbf{u} \cdot \nabla_\perp \mathbf{u} + w\partial_z \mathbf{u} \rangle\right) , \qquad (4.94)$$

where roll velocity $\mathbf{U} = (U, V) = \left(\frac{1}{\hat{r}}\psi_\theta, \psi_{\hat{r}}\right)$ and related to ω by

$$-\Delta_\perp \psi = \omega \qquad (4.95)$$

This is supplemented by regularity at the origin and wall boundary conditions $\psi\left(\delta^{-1}, \theta\right) = 0 = \partial_{\hat{r}}\psi\left(\delta^{-1}, \theta\right)$. Recall the property (4.45) of the waves outside the critical layer of thickness $\hat{\delta} = O((R\delta^4)^{-1/3})$, if $<< 1$, then the forcing from the wave outside the critical layer in (4.94) is $O\left((R\delta^4)^{-1/3}\right)$ and hence small in the case $\delta >> R^{-1/4}$. In all cases it is at most $O(1)$.

In the far-field $\hat{r} >> 1$, as shall be seen later and in conformity with numerical observations of the $C1$-$C2$ states, because of rapid decay in $\hat{r}$ (see (4.141)-(4.142) in the ensuing) for each the Reynolds stress terms arising from the waves in (4.94) is seen to be negligible; therefore, it is consistent to neglect them in the leading order asymptotics for ψ. Now, if $\mathbf{U} = o(\hat{r}^{-1})$, then it is consistent to assume that the large $\hat{r}$ behavior is dominated by solutions of Laplace's equation for vorticity ω, and hence biharmonic equation for ψ. In that case, the stream function ψ is expected to be dominated by the least decaying solution in $\hat{r}$ of the biharmonic equation which is a multiple of $\hat{r}^{-m_0+2}\sin(m_0\theta)$. For $m_0 = 4$, this assumption is self-consistent since the corresponding $\mathbf{U} = O(\hat{r}^{-3}) = o(\hat{r}^{-1})$.

On the other hand if $m_0 = 2$, if we assumed that the stream function ψ is dominated by the least decaying solution of biharmonic equation, then we arrive at $\mathbf{U} = O(\hat{r}^{-1})$, implying $\mathbf{U} \cdot \nabla_\perp \omega$ is the same order as $\Delta_\perp \omega$ in (4.94). This is inconsistent with neglecting $\mathbf{U} \cdot \nabla\omega$. Nonetheless, it is to be recognized that the non-generic situation $\psi \sim \hat{r}^{-2}\sin(2\theta)$ for the biharmonic solution is a possibility for $m_0 = 2$ in which case, it is consistent to ignore $\mathbf{U} \cdot \nabla_\perp\omega$.

In order to recognize role of forcing and wall boundary conditions and determine this nongeneric situation where the least decaying behavior is suppressed for any particular m_0, it is better to formulate an integral equation approach. The equation for coefficient of $\sin(m\theta)$ for stream function ψ may be written as

$$-\left(\frac{d^2}{d\hat{r}^2} + \frac{1}{\hat{r}}\frac{d}{d\hat{r}} - \frac{m^2}{\hat{r}^2}\right)^2 \psi_m = [\nabla_\perp \cdot (\mathbf{U}\omega)]_m + \left(R\delta^4\right)^{1/3}\left(\nabla_\perp \times \langle \mathbf{u} \cdot \nabla_\perp \mathbf{u} + w\partial_z\mathbf{u}\rangle\right)_m =: F_m(\hat{r})$$

$$(4.96)$$

with the polar coordinate representation of the m-th azimuthal mode

$$\mathbf{U} = (U, V) = \left(\frac{m}{\hat{r}}\cos(m\theta)\psi_m(\hat{r}), -\psi_m'(\hat{r})\sin(m\theta)\right) \qquad (4.97)$$

The solution to (4.96) satisfying noslip condition at the walls: $\psi_m(\delta^{-1}) = 0 = \psi_m'(\delta^{-1})$

and regular at the origin is given by

$$
\psi_m(\hat{r}) = \frac{1}{8m(m^2-1)} \left\{ (m+1)\hat{r}^m \int_{\delta^{-1}}^{\hat{r}} F_m(t)t^{3-m}dt + (m-1)\hat{r}^{-m} \int_0^{\hat{r}} F_m(t)t^{3+m}dt \right.
$$
$$
\left. -(m-1)\hat{r}^{m+2} \int_{\delta^{-1}}^{\hat{r}} F_m(t)t^{1-m}dt - (m+1)\hat{r}^{2-m} \int_0^{\hat{r}} F_m(t)t^{1+m}dt \right\}
$$
$$
+ A_m \hat{r}^m + B_m \hat{r}^{m+2} \quad (4.98)
$$

where

$$
A_m = -\frac{\delta^{2m}}{8m} \int_0^{\delta^{-1}} F_m(t)t^{3+m}dt + \frac{\delta^{2m-2}}{8(m-1)} \int_0^{\delta^{-1}} F_m(t)t^{m+1}dt \quad (4.99)
$$

$$
B_m = \frac{\delta^{2m+2}}{8(m+1)} \int_0^{\delta^{-1}} t^{3+m}F_m(t)dt - \frac{\delta^{2m}}{8m} \int_0^{\delta^{-1}} t^{m+1}F_m(t)dt \quad (4.100)
$$

Thus, since Reynolds stress term from waves is negligible, we have $F_m \sim [\nabla_\perp \cdot (\mathbf{U}\omega)]_m$. Now, we have $\nabla_\perp \omega = \left(\partial_{\hat{r}}\omega, \frac{1}{\hat{r}}\partial_\theta \omega \right)$

4.3.1. Leading order roll asymptotics for four-fold ($m_0 = 4$) symmetric solution

For a state, such as the C_2, where we have shift and rotate symmetry besides shift and reflect symmetry, there is a four fold symmetry for rolls and streaks, though not for waves, in which case the stream function corresponding to the rolls may be expressed as $\psi = \sum_{j=1}^\infty \psi_{4j} \sin(4j\theta)$. It follows that

$$
\omega = \sum_{j=1}^\infty \omega_{4j}(\hat{r}) \sin(4j\theta) , \quad (4.101)
$$

where

$$
\omega_{4j}(\hat{r}) = \psi''_{4j}(\hat{r}) + \frac{1}{\hat{r}}\psi'_{4j}(\hat{r}) - \frac{16j^2}{\hat{r}^2}\psi_{4j}(\hat{r}) \quad (4.102)
$$

It follows

$$
\nabla_\perp \omega = \sum_{j=1}^\infty \left(\omega'_{4j}(\hat{r}) \sin(4j\theta) , \frac{4j}{\hat{r}}\omega_{4j}(\hat{r}) \cos(4j\theta) \right) \quad (4.103)
$$

$$
\mathbf{U} \cdot \nabla_\perp \omega = \sum_{j,k=1}^\infty \left(\frac{4k}{\hat{r}}\psi_{4k}(\hat{r})\omega'_j(\hat{r}) \sin(4j\theta)\cos(4k\theta) - \frac{4j}{\hat{r}}\psi'_{4k}(\hat{r})\omega_{4j}(\hat{r}) \sin(4k\theta)\cos(4j\theta) \right) \quad (4.104)
$$

and therefore, with $m = 4n$. It is consistent to assume (see (4.141)-(4.142) in the ensuing) that the wave contribution to F_m is small and so

$$
F_m \sim [\mathbf{U} \cdot \nabla_\perp \omega]_m = \sum_{j=1}^{n-1} \left\{ \frac{2(n-j)}{r}\psi_{4(n-j)}(r)\omega'_{4j}(r) - \frac{2j}{r}\psi'_{4(n-j)}(r)\omega_{4j}(r) \right\}
$$
$$
+ \sum_{k=1}^\infty \left\{ \frac{2k}{r}\psi_{4k}(r)\omega'_{4n+4k}(r) + \frac{2(n+k)}{r}\psi'_{4k}(r)\omega_{4n+4k}(r) \right\}
$$
$$
- \sum_{j=1}^\infty \left\{ \frac{2(n+j)}{r}\psi_{4n+4j}(r)\omega'_{4j}(r) + \frac{2j}{r}\psi'_{4n+4j}(r)\omega_{4j}(r) \right\} \quad (4.105)
$$

It is clear from the above expression that the contribution to F_m for $m > 4$ in the range $1 << \hat{r} << \delta^{-1}$ must come from the first term. while for $m = 4$, there is no contribution from the first term. It is not difficult to conclude that for $n \geqslant 1$, $\psi_{4n} \sim \hat{r}^{-2n}, \omega_{4n} \sim \hat{r}^{-2-2n}$, while $F_4 \sim \hat{r}^{-10}$, and for $n \geqslant 2$, $F_{4n} \sim \hat{r}^{-4-2n}$. In particular, for $n = 1$ $(m = 4)$, we obtain from (4.98)

$$\psi_4(\hat{r}) = \frac{1}{480} \left\{ -5\hat{r}^{-2} \int_0^{\delta^{-1}} F_4 t^5 dt + 3\hat{r}^{-4} \left(\int_0^{\delta^{-1}} F_4 t^7 dt \right) + O(\hat{r}^{-6}) \right\} \tag{4.106}$$

which implies that the leading order behavior of the roll in the far-field is

$$\mathbf{U} = (U, V) \sim \frac{1}{\hat{r}^3} \left(4c_4 \cos(4\theta), 2c_4 \sin(4\theta) \right) \tag{4.107}$$

where c_4 is the coefficient of $\hat{r}^{-2}$ in (4.106) where the higher order harmonics decay even faster.

4.3.2. *Leading order roll asymptotics for two-fold ($m_0 = 2$) symmetric solution*

Now, consider the asymptotics for states with two-fold azimuthal symmetry, so that $m = 2n$ for integer $n \geqslant 1$. We mentioned earlier that the least decaying solution to the biharmonic equation corresponds to $\psi = \sin(2\theta)$, which is not consistent with neglect of $\mathbf{U} \cdot \nabla_{\perp} \omega$.

This suggests that if indeed the leading order behavior of $\mathbf{U} = O(\hat{r}^{-1})$. Thus we should look for stream function solution of the fully nonlinear equation (4.94) (neglecting the wave contribution) in the form

$$\psi = F(\theta) \tag{4.108}$$

where corresponding velocity $(U, V) = \frac{1}{\hat{r}} \left(F'(\theta), 0 \right)$ having π-periodicity in θ. This leads to the nonlinear ODE:

$$2F'(\theta)F''(\theta) + 4F''(\theta) + F^{(iv)}(\theta) = 0 \tag{4.109}$$

The first integral gives

$$F'^2(\theta) + 4F'(\theta) + F'''(\theta) = 3A_1 - 4 \tag{4.110}$$

Define G so that $F'(\theta) + 2 = -6G$. Then

$$G'' = -\frac{A_1}{2} + 6G^2 \tag{4.111}$$

implying on integration

$$G'^2 = 4G^3 - A_1 G - A_0 \tag{4.112}$$

This has a solution in terms of the Weirstrass elliptic function $\mathcal{P}(z + C, \omega_1, \omega_2)$. Requiring π periodicity of a real valued solution gives rise a one-parameter family of solution which may be taken to be a_1 in the following Fourier representation

$$G(\theta) = \sum_{k=0}^{\infty} a_k \cos(2k\theta) \tag{4.113}$$

However, any such solution must correspond to no net radial flux through a cylinder $\hat{r} = \hat{r}_0$ since the flux through the other boundary $\hat{r} = \delta^{-1}$ is zero. This implies that $F(\theta)$ must be also π-periodic in θ, implying that

$$\int_0^{\pi} (6G(\theta) + 2)d\theta = 0 \quad \text{implying } a_0 = -\frac{1}{3} \tag{4.114}$$

The only solution that corresponds to this is $a_1 = 0$. This can be seen easily through a pertubation expansion in parameter a_1. Straight forward perturbation expansion and requirement of periodicity shows

$$G(\theta) = -1/3 + a_1 \cos(2\theta) + a_1^2 \left(-1/4 \cos(4\theta) + 1/8\right) + \frac{3}{64} a_1^3 \cos(6\theta)$$

$$+ a_1^4 \left(-\frac{1}{128} \cos(8\theta) + \frac{1}{128} \cos(4\theta) + \frac{1}{512}\right) + a_1^5 \left(\frac{5}{4096} \cos(10\theta) - \frac{9}{4096} \cos(6\theta)\right)$$

$$+ a_1^6 \left(-\frac{3}{16384} \cos(12\theta) + \frac{1}{2048} \cos(8\theta) - \frac{3}{8192} \cos(4\theta) - \frac{3}{32768}\right) + O(a_1^7) \quad (4.115)$$

There is no freedom left in satisfying $a_0 = -\frac{1}{3}$ when $a_1 \neq 0$ but small. That this is the case beyond the perturbation regime follows from the Elliptic function representation.

We are forced to conclude that the assumption that $\mathbf{U} = O(\hat{r}^{-1})$ is inconsistent with with no flux through the surface $\hat{r} = \hat{r}_0$, which in turn is necessary for no flux through the boundary walls. Instead we have to look for non-generic solutions of the bi-harmonic equation $\Delta^2 \psi = 0$ in the far-field for which $\psi(\hat{r}, \theta) \sim \frac{1}{\hat{r}^2} \sin(2\theta)$, in which case it is consistent to ignore $\mathbf{U} \cdot \nabla_\perp \omega$ in (4.94). With this assumption we return to the integral equation (4.98), now with the representation $\psi = \sum_{j=1}^{\infty} \psi_{2j}(\hat{r}) \sin(2j\theta)$. It follows that

$$\omega = \sum_{j=1}^{\infty} \omega_{2j}(\hat{r}) \sin(2j\theta) , \quad (4.116)$$

where

$$\omega_{2j}(\hat{r}) = \psi''_{2j}(\hat{r}) + \frac{1}{\hat{r}} \psi'_{2j}(\hat{r}) - \frac{4j^2}{\hat{r}^2} \psi_{4j}(\hat{r}) \quad (4.117)$$

It follows

$$\nabla_\perp \omega = \sum_{j=1}^{\infty} \left(\omega'_{2j}(\hat{r}) \sin(2j\theta) , \frac{2j}{\hat{r}} \omega_{2j}(\hat{r}) \cos(2j\theta)\right) \quad (4.118)$$

$$\mathbf{U} \cdot \nabla_\perp \omega = \sum_{j,k=1}^{\infty} \left(\frac{2k}{\hat{r}} \psi_{2k}(\hat{r}) \omega'_{2j}(\hat{r}) \sin(2j\theta) \cos(2k\theta) - \frac{2j}{\hat{r}} \psi'_{2k}(\hat{r}) \omega_{2j}(\hat{r}) \sin(2k\theta) \cos(2j\theta)\right)$$

$$(4.119)$$

It is again consistent to assume that the wave contribution towards F_m is small (see (4.141)-(4.142) in the ensuing) implying that

$$F_m \sim [\mathbf{U} \cdot \nabla_\perp \omega]_m = \sum_{j=1}^{n-1} \left\{\frac{(n-j)}{r} \psi_{2(n-j)}(r) \omega'_{2j}(r) - \frac{j}{r} \psi'_{2(n-j)}(r) \omega_{2j}(r)\right\}$$

$$+ \sum_{k=1}^{\infty} \left\{\frac{k}{r} \psi_{2k}(r) \omega'_{2n+2k}(r) + \frac{(n+k)}{r} \psi'_{2k}(r) \omega_{2n+2k}(r)\right\}$$

$$- \sum_{j=1}^{\infty} \left\{\frac{(n+j)}{r} \psi_{2n+2j}(r) \omega'_{2j}(r) + \frac{j}{r} \psi'_{2n+2j}(r) \omega_{2j}(r)\right\} \quad (4.120)$$

It is consistent to assume $F_2, F_4, F_6 \sim \hat{r}^{-8}$, $F_{2n} \sim \hat{r}^{-(2n+2)} \log \hat{r}$ and $\psi_2, \psi_4 \sim \hat{r}^{-2}$ and $\psi_{2n} \sim \hat{r}^{-2n+2} \ln \hat{r}$ for $n \geqslant 3$, provided we satisfy the non-generic condition

$$\int_0^{\delta^{-1}} F_2(t) t^3 dt = 0 \quad (4.121)$$

Then, in particular for $m = 2$ $(n = 1)$ from (4.98), we get

$$\psi_2(\hat{r}) \sim \frac{1}{48} \left\{ \hat{r}^{-2} \left(\int_0^{\delta^{-1}} F_2(t) t^5 dt \right) + O(\hat{r}^{-4}) \right\} \tag{4.122}$$

The nongeneric assumption (4.121) is forced on us as as otherwise a fully-nonlinear analysis with the ansatz $\psi = F(\theta)$ in the roll-equation revealed no acceptable solution. Therefore, we conclude that with two-fold symmetry $(m_0 = 2)$, we must have

$$\mathbf{U} = (U, V) \sim \frac{1}{\hat{r}^3} \left(2c_2 \cos(2\theta), 2c_2 \sin(2\theta) \right) \tag{4.123}$$

where c_2 is the coefficient of $\hat{r}^{-2}$ in (4.122).

4.4. *Far-Field Streak analysis and absence of log correction to leading order*

Consider the full streak equation, which on using divergence equation, may be written in the form

$$\nabla_\perp W = -2\hat{r}U + \nabla_\perp \cdot (\mathbf{U}W) + \left(R\delta^4 \right)^{-2/3} \langle \nabla_\perp \cdot (\mathbf{u}w) \rangle \tag{4.124}$$

Now, we have

$$W(\hat{r}, \theta) = \sum_{k=0}^{\infty} W_k(\hat{r}) \cos(kk_0\theta) \tag{4.125}$$

and therefore, in particular

$$W_0(r) = \frac{1}{2\pi} \int_0^{2\pi} W(\hat{r}, \theta) d\theta =: \overline{W} \tag{4.126}$$

It follows from (4.124) and the observation that $U_0(r) = 0$ that $W_0(r)$ satisfies

$$\frac{1}{\hat{r}} \frac{d}{d\hat{r}} \left(\hat{r} \frac{d}{d\hat{r}} \tilde{W}_0 \right) = \overline{\nabla_\perp \cdot (\mathbf{U}W)} + \left(R\delta^4 \right)^{-2/3} \overline{\langle \nabla_\perp \cdot (\mathbf{u}w) \rangle} =: M_0(\hat{r}) \tag{4.127}$$

Therefore, using regularity at the origin, and $W_0(\delta^{-1}) = 0$, we have from integration of (4.127)

$$W_0(r) = \int_{\delta^{-1}}^{\hat{r}} \frac{dr'}{r'} \int_0^{r'} sM_0(s)ds = \int_{\delta^{-1}}^{\hat{r}} \left(\ln \hat{r} - \ln s \right) sM(s)ds + \left(\int_0^{\delta^{-1}} sM(s)ds \right) \ln r \tag{4.128}$$

However, from expression of $M_0(\hat{r})$ in (4.127), and using divergence theorem and pipe-wall boundary conditions at $\hat{r} = \delta^{-1}$.

$$\int_0^{\delta^{-1}} sM_0(s)ds = \frac{1}{2\pi} \int_0^{\delta^{-1}} \hat{r}d\hat{r} \int_0^{2\pi} d\theta \nabla_\perp \cdot (\mathbf{U}W)$$

$$+ \left(R\delta^4 \right)^{-2/3} \frac{\alpha}{4\pi^2} \int_0^{2\pi/\alpha} dz \left[\int_0^{\delta^{-1}} \hat{r}d\hat{r} \int_0^{2\pi} d\theta \nabla_\perp \cdot (\mathbf{u}w) \right] = 0 \tag{4.129}$$

It follows that $W_0'(\delta^{-1}) = 0$. This implies that the period averaged friction at the wall remains the same as for Poisseuille flow. However, since the calculation is with a fixed pressure gradient, the flux for these new travelling states is smaller, and hence the friction factor is higher. On integration by parts, and using expression for M_0, this leads to (4.128) also implies

$$W_0(\hat{r}) = \int_{\delta^{-1}}^{\hat{r}} \left(\overline{UW} + \overline{\langle uw \rangle} \right) (s)ds \tag{4.130}$$

The integral representation (4.130) also explains the flatness of the $k = 0$ mode of the streak in a neighborhood of the origin as the integrand is small when both rolls and waves are small, as found in the numerical calculations. Now, consider the m-th azimuthal component of the wave which in scaled form satisfies

$$\left(\frac{d^2}{d\hat{r}^2} + \frac{1}{\hat{r}}\frac{d}{d\hat{r}} - \frac{m^2}{\hat{r}^2}\right)W_m = -2\hat{r}U_m + \nabla_\perp \cdot (\mathbf{U}W)_m + \left(\frac{1}{R\delta^4}\right)^{2/3}\langle\nabla \cdot (\mathbf{u}w)\rangle_m =: M_m(r)$$

(4.131)

where subscript m denotes $\cos(m\theta)$ Fourier-component for $m \geqslant 2$. Therefore, by requiring W_m to be regular at $\hat{r} = 0$ and be zero at $\hat{r} = \delta^{-1}$, we have

$$W_m(\hat{r}) = \frac{\hat{r}^m}{2m}\int_{\delta^{-1}}^{\hat{r}}\rho^{1-m}M_m(\rho)d\rho - \frac{\hat{r}^{-m}}{2m}\int_0^{\hat{r}}\rho^{1+m}M_m(\rho)d\rho + B_m\hat{r}^m \ , \qquad (4.132)$$

where

$$B_m = \frac{\delta^{2m}}{2m}\int_0^{\delta^{-1}}\rho^{1+m}M_m(\rho)d\rho \qquad (4.133)$$

4.4.1. *Far-Field behavior of streak for four-fold symmetry ($m_0 = 4$)*

We now consider the behavior of M_m, using the behavior of the rolls $\hat{U}_m = (U_m, V_m)$ derived earlier, for $m = 4n$, $n \geqslant 1$. These are the four-fold azimuthally symmetric roll and streaks for states such as $C2$ that we have computed. We have already deduced that $\psi_{4n}(\hat{r}) \sim \hat{r}^{-2n}$ for $n \geqslant 1$ and therefore, it will follow that $(U_{4n}, V_{4n}) \sim \hat{r}^{-2n-1}$. It is consistent to assume (see (4.141)-(4.142) in the ensuing) that the wave contribution to M_{4n} is negigible and hence from the decay of (U_{4n}, V_{4n}) it follows at once that $M_{4n} \sim \hat{r}^{-2n}$, $W_{4n} \sim \hat{r}^{-2n+2}$ for $n \geqslant 1$. We also note that this implies that M_0 which has no contribution from $2rU_0$ term, will have the asymptotic behavior $\hat{r}^{-4}$ and therefore the asymptotic behavior of $W_0(r) \sim \hat{r}^{-3}$ in the regime $1 << \hat{r} << \delta^{-1}$. In particular, we note that the streak has a dominating contribution like $W(\hat{r}, \theta) \sim W_4(\hat{r})\cos(4\theta) \sim \cos(4\theta)$ in the asymptotic regime. In other words, the streak does not decay and continues to the far-field, until the wall effect becomes important. This is seen in Figure 36, though limitations in the largeness of R, the regime $1 << \hat{r} << \delta^{-1}$ is not quite visible.

4.4.2. *Far-Field behavior of streak for two-fold symmetric states*

We now consider the behavior of M_m, using the behavior of rolls $\hat{U}_m = (U_m, V_m)$ derived earlier, for $m = 2n$, $n \geqslant 1$. These are the two fold azimuthally symmetric roll and streaks for states such as $C1$ that we have computed. Recall, we derived $\psi_2, \psi_4 \sim \hat{r}^{-2}$, $\psi_{2n} \sim \hat{r}^{-2n+2}\ln\hat{r}$ for $n \geqslant 3$. This implies $(U_2, V_2), (U_4, V_4) = O(\hat{r}^{-3})$ and $(U_{2n}, V_{2n}) \sim \hat{r}^{-2n+1}\ln\hat{r}$ for $n \geqslant 3$. implying from neglect of wave contribution (see (4.141)-(4.142)) that $M_2, M_4 \sim \hat{r}^{-2}$ and $M_{2n} \sim \hat{r}^{-2n+2}\ln\hat{r}$, for $n \geqslant 3$. This implies that $W_2 \sim \hat{c}_2, W_4 \sim \hat{c}_4$, which are constants, and $W_{2n} \sim \hat{r}^{4-2n}\ln\hat{r}$ for $n \geqslant 3$. We also note that M_0, which has no contribution from $2rU_0$ term since $U_0 = 0$ has asymptotic behavior $\hat{r}^{-4}$ and therefore the asymptotic behavior of $W_0(r) \sim \hat{r}^{-3}$ in the regime $1 << \hat{r} << \delta^{-1}$. In particular, we note that the streak has a dominating contribution like $W(\hat{r}, \theta) \sim \hat{c}_2\cos(2\theta) + \hat{c}_4\cos(4\theta)$ in the asymptotic regime. In other words, the streak does not decay and continues to the far-field, until the wall effect becomes important. However, this behavior is not clear in Figure 33, because the behavior becomes more complicated by the expected occurrence of $\hat{r}^{-1}\sin(4\theta)$ in the roll-stream function appearing in a higher order analysis and the fact that δ is not so small in the numerical calculations.

4.5. *Far-field analysis of Wave equation*

We have from the pressure equation the linear pressure equation the following representation

$$p = \sum_{m=0}^{\infty} p_m(\hat{r}, z) \cos(m\theta) \tag{4.134}$$

Then, it is clear that $p_m(r, z)$ will satisfy

$$\partial_{\hat{r}}^2 p_m + \frac{1}{\hat{r}} \partial_{\hat{r}} p_m - \frac{m^2}{\hat{r}^2} p_m - \left[\frac{2}{(c_1 - \hat{r}^2 + W)} \left(-2\hat{r} + \partial_{\hat{r}} W\right) \partial_r p \right]_m$$
$$- \frac{1}{\hat{r}^2} \left[\frac{2\partial_\theta W}{(c_1 - \hat{r}^2 + W)} \partial_\theta p \right]_m + \delta^2 \partial_z^2 p_m = 0 \tag{4.135}$$

If $W_r << \hat{r}$ and $W_\theta << \hat{r}^2$, which is the case both for two-fold and four-fold azimuthally symmetric streaks, then the behavior in a regime $1 << \hat{r} << \delta^{-1}(1 - R^{-1/2+\epsilon})$ is given by

$$\partial_{\hat{r}}^2 p_m - \frac{3}{\hat{r}} \partial_{\hat{r}} p_m - \frac{m^2}{\hat{r}^2} p_m + \delta^2 \partial_z^2 p_m = 0 \tag{4.136}$$

with corresponding radial and azimuthal velocities satisfying $\partial_z u_m \sim \hat{r}^{-2} \partial_{\hat{r}} p_m$ and $\partial_z v_m = \pm m \hat{r}^{-3} p_m$ and axial wave velocity component satisfying $\partial_z w_m \sim -2\hat{r}^{-1} u_m$ The general solution of 4.136 in terms of Bessel functions:

$$p_m(\hat{r}, z) = \hat{r}^2 \sum_l e^{i\alpha l z} \left(C_{l,m} I_{\sqrt{4+m^2}}(l\delta\alpha\hat{r}) + D_{l,m} K_{\sqrt{4+m^2}}(l\delta\alpha\hat{r}) \right) \tag{4.137}$$

The equations have to be modified in the regime $\delta\hat{r} - 1 = O(R^{-1/2})$ to account for the wall boundary layer. However, radial component u_m of the wave velocity as the wall boundary layer is approached must be zero to the leading order; hence the only consistent solution corresponds to choice $C_{l,m} = 0$. Now, since $\delta << 1$, in the regime $1 << \hat{r} << \delta^{-1}$, the expected behavior of p_m is given by

$$p_m(\hat{r}, z) \sim \hat{D}_{l,m} e^{i\alpha z} (\hat{r})^{2-\sqrt{m^2+4}} + C.C. \tag{4.138}$$

Using (4.72), this gives leading order decay rate for wave velocity components perpendicular to the axis

$$(u, v) \sim -\frac{1}{i\alpha} e^{i\alpha z} \hat{r}^{-2(\sqrt{2}-1)-3} \left((2\sqrt{2} - 2)\sin(2\theta), 2\cos(2\theta) \right) + C.C. \tag{4.139}$$

Using (4.73), it follows that that the axial velocity behaves as

$$w \sim -\frac{1}{\alpha^2} e^{i\alpha z} \hat{r}^{-2(\sqrt{2}-1)-4} (2\sqrt{2} - 2)\sin(2\theta) + C.C. \tag{4.140}$$

We also note that rapid algebraic decay of m-azimuthal mode

$$(u_m, v_m) \sim \hat{r}^{-\sqrt{m^2+4}-1} \tag{4.141}$$

$$w_m \sim \hat{r}^{-\sqrt{m^2+4}-2} \tag{4.142}$$

This is quite consistent with the numerical profiles for waves corresponding to $C2$ solution shown in Figure 39. Similar decay is observed for $C1$ mode as well.

4.6. *Canonical parameter free problem for NVC states*

Using scaled variables (4.39)-(4.40), (4.3) transforms into the the following set of scaled nonlinear equations:

$$\left(c_1 - \hat{r}^2 + \hat{w}\right)\partial_z\hat{\mathbf{v}}_\perp + \hat{\mathbf{v}}_\perp \cdot \nabla_\perp\hat{\mathbf{v}}_\perp = -\nabla_\perp\hat{p} + \Delta_\perp\hat{\mathbf{v}}_\perp + \delta^2\partial_z^2\hat{\mathbf{v}}_\perp \tag{4.143}$$

$$\left(c_1 - \hat{r}^2 + \hat{w}\right)\partial_z\hat{w} + \hat{\mathbf{v}}_\perp \cdot \nabla_\perp\left(c_1 - \hat{r}^2 + \hat{w}\right) = -\delta^2\partial_z\hat{p} + \Delta_\perp\hat{w} + \delta^2\partial_z^2\hat{w} \tag{4.144}$$

$$\nabla_\perp \cdot \hat{\mathbf{v}}_\perp + \frac{\partial\hat{w}}{\partial z} = 0 \tag{4.145}$$

To the leading order, $\delta^2 = O(R^{-1/2})$ terms are ignored, and the resulting fully nonlinear parameter-free eigenvalue problem in the infinite domain $0 < \hat{r} < \infty$, 2π-periodic in both θ and αz:

$$\left(c_1 - \hat{r}^2 + \hat{w}\right)\partial_z\hat{\mathbf{v}}_\perp + \hat{\mathbf{v}}_\perp \cdot \nabla_\perp\hat{\mathbf{v}}_\perp = -\nabla_\perp\hat{p} + \Delta_\perp\hat{\mathbf{v}}_\perp \tag{4.146}$$

$$\left(c_1 - \hat{r}^2 + \hat{w}\right)\partial_z\hat{w} + \hat{\mathbf{v}}_\perp \cdot \nabla_\perp\left(c_1 - \hat{r}^2 + \hat{w}\right) = \Delta_\perp\hat{w} \tag{4.147}$$

has to be solved together with divergence condition (4.145), which is qualitatively analogous to a problem in boundary layer flow Deguchi and Hall (2014). The far-field behavior of rolls, streaks and wave components of the travelling wave, discussed in subsections §(4.3)- §(4.5) gives the relevant far-field condition for different Fourier components of $\hat{\mathbf{v}}_\perp$ and $\hat{w}$.

5. Comparison between numerical computation and asymptotic scaling

First, for VWI states when $\delta = 1$, the R^{-1} scale for rolls, $O(1)$ scale for streaks and a maximal wave amplitude of $O(R^{-5/6})$ occurring in a critical layer of width $R^{-1/3}$ is, as expected, the same as Hall and Sherwin (2010) theory for channels. Because $(1 - c)^{-1} = O(1)$, and the critical layer is not close to the pipe center, the geometric difference between a pipe and channel does not make any difference to the scale prediction. Indeed, reported scale for rolls and critical layer thickness from direct numerical calculation by Viswanath (2009a) for the S anti-symmetric state is consistent with this prediction. Since asymptotic theory predicts that wave ampitude scaling $R^{-5/6}$ only persists over a layer of thickness $R^{-1/3}$, and drops down to $O(R^{-7/6})$ outside the layer, it is clear that the kinetic energy of the waves is dominated by critical layer contribution and scales as R^{-2}. The squareroot of kinetic energy for $l = 1$, which is the dominant contribution, reported in Viswanath (2009a) is $R^{-0.97}$, not far from asymptotic theory. As mentioned before, we were unable to get numerical convergence for WK solutions for values of R much larger than about 11,000 and so agreement with asymptotic scaling results for VWI-states is only qualitative.

On the other hand, the numerically computed C_1, C_2 solutions appear to suggest a shrinking structure near the center of the pipe as R increases. For such cases, we have identified two theoretical possibilities in the section §4 as $R \to \infty$:

Case (**i**) corresponds to a nonlinear viscous core with radial scaling $\delta = R^{-1/4}$, with axial component of both streak and waves scaling as $\delta_3 = \delta_4 = \delta^2 = R^{-1/2}$ while perpendicular components of both rolls and wave-velocity scaling as $\delta_1 = \delta_2 = \delta^3 = R^{-3/4}$. In this case, the perturbation of, wave speed from 1 scales as $\delta_c = \delta^2 = R^{-1/2}$. The canonical equations that arise have been presented in §4.6.

Case (**ii.**) corresponds to a shrinking VWI state where $\delta = R^{-1/6}$, $\delta_3 = \delta_c = \delta^2 = R^{-1/3}$, $\delta_1 = R^{-5/6}$, $\delta_2 = R^{-5/6}\delta^{-1/3} = R^{-7/9}$, $\delta_4 = R^{-5/6}\delta^{-4/3} = R^{-11/18}$.

We notice from Table 1 that $\delta_1\delta \approx \frac{1}{R}$, and $\delta_c \approx \delta_3$ as expected from the theory in either case (**i**) or (**ii**). though for the smaller α value, $C2$ solution shows a marked departure. We also notice that $\delta_4 \approx \frac{\delta_2}{\delta}$ as expected from theory. However, $\delta^2 \approx R^{-0.46}$ is not as close to $\delta_3 \approx R^{-0.36}$ as expected from $R \to \infty$ consistent scaling. Nonetheless, the observed wave stress S_1, S_2 scaling in Figures 40, 41 is consistent with asymptotic scaling argument $R^{-5/3}\delta^{-5/3}$. Since our numerical results on improved resolution did not change the scales significantly, our conclusion is that the $R \to \infty$ asymptotics has been attained for some, but not all quantities. This should not be too surprising since for instance the scaling of radial roll component seen in Figure 31 show that in some instance the largest amplitude azimuthal component has steeper slope than the second largest. Clearly, if the same slopes persist, the one which does not decay as rapidly with R will have to dominate eventually. In this connection, it is to be noted further that Deguchi and Walton (2013) numerical scaling results for spiralling centermodes in a pipe were in agreement with Smith and Bodonyi (1982) asymptotics for $R \geqslant 10^8$; hence it is not unexpected that our finite R scaling results for $R \leqslant 2 \times 10^5$ should deviate from $R \to \infty$ asymptotics.

To the extent that the observed core scaling δ (see Table 1) in the numerically calculated range of R is much closer to the theoretical $R^{-1/4}$ scale for NVC states than the $R^{-1/6}$ predicted for shrinking VWI states, we believe that the $C1-C2$ solutions are finite R realization of the NVC states. There is of course significant discrepancy between the numerically computed and asymptotically predicted δ_3, δ_c, but we believe this is because the R range of calculations is not sufficiently large. It is noteworthy that $1-c$ versus R curve consistently drifts towards a steeper slope for larger α suggesting that this is indeed the case since in the wave analysis, αR, appears as a single large parameter. Also, the Reynolds stress contour curves in Figures 42- 43 show that they are significantly spread out from the critical curve, which is quite different from the typical clustering observed in the VWI solution Deguchi and Hall (2014).

6. Discussion and Conclusion

In this paper, we report numerical computation travelling wave solutions with shift and reflect symmetry through a numerical continuation process involving small alternate wall suction and injection in the azimuthal direction. Through linear stability analysis of the base state in the presence of suction-injection at a critical Reynolds number, a neutrally stable mode was used to determine initial guess in a Newton iteration procedure to determine finite amplitude travelling wave solution. Far from the Hopf-bifurcation point in the parameter space, solutions were continued until suction-injection was completely turned off. This allowed recovery of previous solutions of Wedin and Kerswell (2004), which provided an additional check on the numerical code. Though restricted only to solutions with two-fold azimuthal symmetry, the process of calculation also resulted in the discovery of two previously unrecognized solution branches, marked by a collapsing structure near the center of the pipe. We present many features of these solutions, identified as $C1$ and $C2$, including scaling of the lower-branch with Reynolds number in the range $5 \times 10^4 < R < 2 \times 10^5$. The $C2$ branch of solution possesses shift and rotate symmetry, besides the shift and reflect symmetry, resulting in streaks and rolls having four-fold azimuthal symmetry.

We also presented general asymptotic arguments for $R \to \infty$ to identify all possible scalings as $R \to \infty$. For asymptotic states where axial wave number is independent of R, we identify two possible classes of solution. The first is a nonlinear viscous core (NVC), with core radius $\delta = R^{-1/4}$, where axial components of fluid velocity scale as $R^{-1/2}$, while

velocity components perpendicular to the pipe axis scale as $R^{-3/4}$. In this case, the wave speed c satisfies $(1-c) \sim c_1 R^{-1/2}$ as $R \to \infty$, where c_1 is some order one constant. In the shrinking core, the inner-equation is a fully nonlinear eigenvalue problem with c_1 as the eigenvalue; the equation resembles a fully nonlinear Navier-Stokes with $R = 1$. This nonlinear viscous core state is similar in many respect to the ones discovered by Deguchi and Hall (2014) in a boundary layer flow. While the wave and roll components are localized in the shrinking core with algebraic decay as one moves away from the core, the streak component, though small, is the same size inside and outside the core, until wall effects become important. Unlike boundary layer flows of Deguchi and Hall (2014), there is no exponential growth of streak magnitude, instead some azimuthal component remains constant. We present evidence to suggest that the computed $C1$-$C2$ solutions are actually a finite R realization of the NVC states with two-fold azimuthal symmetry.

A second possibility is a class of Vortex Wave (VWI) States, which have rather different asymptotic structures from NVC. We identify, two sub-classes of VWI states, with core width $\delta = 1$ or $\delta = R^{-1/6}$ depending on whether or not the vortex wave-structure collapse towards the pipe center. For a vortex wave (VWI) solution, small linear waves of amplitude $O(R^{-5/6}\delta^{-4/3})$ concentrated mostly in a critical layer of width $\delta\hat{\delta} = \delta(R\delta^4)^{-1/3}$ drive rolls of magnitude $O(R^{-1}\delta^{-1/3})$ which generates streaks of magnitude δ^2. In this case $(1-c) = O(\delta^2)$. Outside the critical layer where viscosity is important but nonlinear interactions still small, the wave components become smaller by a factor of $\hat{\delta} = (R\delta^4)^{-1/3}$. When $\delta = 1$, the scalings of this vortex wave solutions match those of Hall and Sherwin (2010) in a channel-flow, and comparison with so-called S-anti-symmetric numerical solution of Viswanath (2009a) suggests that his solution is a finite R realization of VWI states. Qualitative comparison with data suggests that the same is likely true for the Wedin and Kerswell (2004) solution, though a more quantitative comparison is hampered by our inability to continue Wedin and Kerswell (2004) solution beyond about $R = 11,000$. In the case of shrinking core $\delta << 1$, the conclusion that $\delta = R^{-1/6}$ is the only possibility requires us to consider how neutral modes are perturbed by higher-order effects, and the viscous critical layer plays a paramount role in this consideration.

To the extent that all both VWI and TVC states arise from asymptotically small perturbations of the basic Pouisseuille flow, their relevance to transition in turbulence is already recognized. In this context, we note that the shrinking core states have waves and rolls scaling with larger magnitude than for $\delta = 1$, in that sense, it takes a larger perturbation from Poussueille to reach these new states. On the otherhand, these shrinking core states have less interaction with the pipe boundaries, and therefore likely more robust to perturbations at the boundaries. The stability and control of these states, which are likely to have slow and low dimensional unstable manifolds, are important matters for further research with both theoretical and practical implications.

7. Acknowledgment

8. Appendix

8.1. *Adjoint equation analysis*

The purpose of this appendix is to determine leading order asymptotic behavior of null-space solutions to the adjoint problem $\mathcal{L}^\dagger$ defined in (4.66)-(4.67) when $\epsilon \to 0$.

Note the the kernel of $\mathcal{L}^\dagger$ is determined by nonzero solution to

$$\mu_0 \partial_z \tilde{\mathbf{u}} + \epsilon \Delta_\perp \tilde{\mathbf{u}} = -\mu_0 \nabla_\perp \tilde{w} + \nabla_\perp q \tag{8.1}$$

$$2\mu_0 \partial_z \tilde{w} + \epsilon \Delta_\perp \tilde{w} = \partial_z q \tag{8.2}$$

together with two-dimensional divergence equation (4.68). Because of the z dependence of (4.83)-(4.84), it is clear that nontrivial condition in (4.85) can arise possibly only when z dependence in the adjoint problem is either in the form $e^{\pm i\alpha z}$ or $e^{\pm 2i\alpha z}$. We will only consider $e^{\pm i\alpha z}$ dependence in the adjoint problem since the inviscid adjoint problem is related as the original Rayleigh equation for which eigenfunctions are assumed to exist with $e^{i\alpha z}$ dependence. Further, we can restrict only to $e^{i\alpha z}$ dependence in z since since eigenfunctions with $e^{-i\alpha z}$ dependence does not produce any independent relation from (4.85).

In the region outside the critical layer, the inviscid balance requires that

$$-\mu_0 i\alpha \tilde{\mathbf{u}} = \mu_0 \nabla_\perp \tilde{w} - \nabla_\perp q \tag{8.3}$$

$$-2\mu_0 i\alpha \tilde{w} = -i\alpha q \tag{8.4}$$

Thus, in the inviscid region, to the leading order (using $\langle \tilde{q} \rangle = 0 = \langle \tilde{w} \rangle$)

$$\tilde{w} = \frac{q}{2\mu_0} \tag{8.5}$$

It is clear on substituting (8.5) and

$$q = \frac{2}{\mu_0} \tilde{q} \tag{8.6}$$

into (8.3)-(8.4) that divergence equation $\nabla_\perp \cdot \tilde{\mathbf{u}} = 0$ implies

$$\nabla_\perp \cdot \left(\frac{\nabla_\perp \tilde{q}}{\mu_0^2} \right) = 0 \tag{8.7}$$

and that

$$\mu_0 i\alpha \tilde{\mathbf{u}} = \frac{1}{\mu_0} \nabla_\perp \tilde{q} \tag{8.8}$$

The condition $\tilde{u} = 0$ on the wall immediately implies the Neumann condition

$$\partial_{\tilde{r}} \tilde{q} \left(\delta^{-1}, \theta \right) = 0 \tag{8.9}$$

The inviscid approximation (8.7) with boundary condition (8.9) to the adjoint problem is, as expected, the same as for the original pressure function because the Rayleigh equation is in the self-adjoint form. Therefore, from previous argument for the pressure p, we know that as the critical layer is approached normal component of inviscid $\tilde{q}$ behave as

$$\mathbf{e_s} \cdot \nabla_\perp \tilde{q} \sim -A_1(s) , \quad \mathbf{e_N} \cdot \nabla_\perp \tilde{q} \sim -\left(\frac{A_1(s)}{A_0(s)} \right)' \mu_0 \quad \text{where } A_0 = |\nabla_\perp \mu_0| \tag{8.10}$$

where s denotes the coordinate orthogonal to $\nabla \mu_0$ and $\mathbf{e}_s$ and $\mathbf{e}_N$ denote unit vectors in the direction of increasing s and increasing μ_0. From the inviscid adjoint equation, the

following behavior is implied as the critical layer is approached

$$\tilde{w} \sim \frac{A_w(s)}{\mu_0^2} \ , \quad \text{where} \quad A'_w(s) = -A_1(s) \tag{8.11}$$

$$\tilde{\mathbf{u}} \cdot \mathbf{e_s} \sim \frac{A_S}{\mu_0^2} \quad \text{where} \quad A_S(s) = -\frac{A_1(s)}{i\alpha} \tag{8.12}$$

$$\tilde{\mathbf{u}} \cdot \mathbf{e_N} \sim \frac{A_N}{\mu_0^2} \quad \text{where} \quad A_N = -\frac{1}{i\alpha} \left(\frac{A_1(s)}{A_0(s)}\right)' \tag{8.13}$$

With the knowledge of solution behavior as critical layer is approached, we introduce the critical layer variables

$$\mu_0 = A_0^{2/3}\hat{\delta}n \tag{8.14}$$

$$\tilde{\mathbf{u}} \cdot \mathbf{e_s} \sim \frac{A_s}{A_0^{4/3}\hat{\delta}^2}\mathcal{V} \ , \quad \tilde{\mathbf{u}} \cdot \mathbf{e_N} \sim \frac{A_N}{A_0^{2/3}\hat{\delta}}\mathcal{U} \ , \quad \hat{W} \sim \frac{A_W}{A_0^{4/3}\hat{\delta}^2}\mathcal{W} \ , \quad q \sim \frac{2A_W}{A_0^{2/3}\hat{\delta}}\mathcal{Q} \tag{8.15}$$

The axial velocity results in

$$2i\alpha n\mathcal{W} + \partial_n^2\mathcal{W} = 2i\alpha\mathcal{Q} \tag{8.16}$$

The velocity component in the perpendicular plane in the direction of increasing μ_0 results in the following leading order balance

$$-n\partial_n\mathcal{W} + 2\partial_n\mathcal{Q} = 0 \tag{8.17}$$

The equations (8.16)-(8.17) are self-contained and come with the matching condition

$$\mathcal{W} \sim \frac{1}{n^2} \ , \mathcal{Q} \sim \frac{1}{n} \quad \text{as} \quad n \to \pm\infty \tag{8.18}$$

The tangential velocity equation in the parpendicular plane in the inner-scale results in

$$i\alpha n\mathcal{V} + \partial_n^2\mathcal{V} = i\alpha\mathcal{R}(n,s) \ , \tag{8.19}$$

where

$$\mathcal{R}(n,s) = (2\mathcal{Q} - n\mathcal{W}) + B(s)\partial_n^2\mathcal{W} \ , \tag{8.20}$$

where

$$B(s) = \frac{2A'_0 A_W}{3\alpha^2 A_0 A_S} \tag{8.21}$$

We note that the term independent of s in (8.20) has the asymptotic behavior $\frac{1}{n}$ which dominates $B(s)\partial_n^2\mathcal{W} \sim \frac{6B(s)}{n^4}$ as $n \to \pm\infty$. while divergence equation implies

$$\partial_n\mathcal{U} + \mathcal{V} + B_1(s)\left(2\mathcal{V} + n\partial_n\mathcal{V}\right) + B_0(s)\partial_s\mathcal{V} = 0 \ , \tag{8.22}$$

where

$$B_0(s) = \frac{A_S(s)}{A_0(s)A_N(s)} \ , \quad B_1(s) = -\frac{2A'_0(s)B_0(s)}{3A_0(s)} \tag{8.23}$$

Note that $\mathcal{Q}$ can be eliminated from (8.16) using (8.17) and the resulting equation gives rise to

$$\partial_n^3\mathcal{W} + i\alpha n\partial_n\mathcal{W}_n + 2i\alpha\mathcal{W} = 0 \tag{8.24}$$

This has solution with asymptotic behavior $\mathcal{W} \sim \frac{1}{n^2}$ with the exact representation

$$\mathcal{W}(n) = e^{-i\pi/3}\alpha^{2/3}F\left(e^{-i\pi/6}\alpha^{1/3}n\right) \tag{8.25}$$

where F satisfies

$$zF'' - F' - z^2 F = -1 \tag{8.26}$$

This has a unique solution with behavior $F(z) \sim \frac{1}{z^2}$ as $e^{i\pi/6}z \to \pm\infty$ with the explicit representation

$$F(z) = \frac{4\pi}{(-\sqrt{3}+i)z}\left\{ \mathrm{Ai}'(\omega^{-1}z)\int_\infty^1 \frac{\mathrm{Ai}'(z\tau)}{\tau^2}\mathrm{d}\tau - \mathrm{Ai}'(z)\int_{\omega\infty}^1 \frac{\mathrm{Ai}'(\omega^{-1}z\tau)}{\tau^2}\mathrm{d}\tau \right\} \tag{8.27}$$

where

$$\omega = e^{2i\pi/3} \tag{8.28}$$

The algebraic asymptotic behavior $F(z) \sim \frac{1}{z^2}$ as $e^{i\pi/6}z \to \pm\infty$ is not difficult to deduce. We notice that exponential smallness of the integral involving $\mathrm{Ai}'(z)$ is balanced by the exponential largeness of $\mathrm{Ai}'(\omega^{-1}z)$ outside the integral when $e^{i\pi/6}z \to +\infty$, which on integration by parts, is seen to result in a $O(z^{-2})$ decay. Again the exponential smallness of the integral involving $\mathrm{Ai}'(\omega^{-1}z)$ is balanced by the exponential largeness of $\mathrm{Ai}'(z)$ when $e^{i\pi/6-i\pi}z \to +\infty$. leaving us with $O(z^{-2})$ decay. To see that the expression in (8.27) is actually not singular at $z = 0$ we employ integration by parts, which on using Airy equation, results in

$$F(z) = \frac{4\pi}{(-\sqrt{3}+i)}\left(\mathrm{Ai}'\left(\frac{z}{\omega}\right)\int_\infty^z \mathrm{Ai}(z')\mathrm{d}z' - \omega\mathrm{Ai}'(z)\int_{\omega\infty}^z \mathrm{Ai}\left(\frac{z'}{\omega}\right)\mathrm{d}z' \right) \tag{8.29}$$

which is manifestly regular at $z = 0$. Further from the form of F, it is clear that it is a derivative of a function $G(z)$, whose asymptotic behavior as $e^{i\pi/6}z \to \pm\infty$ is given by $G(z) \sim -\frac{1}{z}$. Thus it follows that

$$\int_{-\infty}^\infty \mathcal{W}(n)\mathrm{d}n = 0 \tag{8.30}$$

Once $\mathcal{W}$ is determined, using (8.16) to eliminate $\mathcal{Q}$ from (8.20) and defining

$$\mathcal{V}(n,s) = \mathcal{W}(n) + i\alpha B(s)e^{-i\pi/3}\alpha^{2/3}H\left(e^{-i\pi/6}\alpha^{1/3}n\right), \tag{8.31}$$

it follows that $H(z)$ satisfies

$$H'' - zH = F'' \tag{8.32}$$

The solution $H(z)$ that decays like z^{-5} as $e^{i\pi/6}z \to \pm\infty$ is given by

$$H(z) = \frac{4\pi}{(\sqrt{3}+i)}\left(\mathrm{Ai}\left(\frac{z}{\omega}\right)\int_\infty^z \mathrm{Ai}(z')F''(z')\mathrm{d}z' - \mathrm{Ai}(z)\int_{\omega\infty}^z \mathrm{Ai}\left(\frac{z'}{\omega}\right)F''(z')\mathrm{d}z' \right) \tag{8.33}$$

Notice that the fast decay rate of $H(z)$ ensures that $\mathcal{V}(n,s) \sim \mathcal{W}(n) \sim \frac{1}{n^2}$ as as $n \to \pm\infty$, as required Once $\mathcal{V}$ through (8.31), then divergence equation (8.22) may be used to determine $\mathcal{U}$.

The upshot of this calculation is to demonstrate that inner-outer matching is possible for the adjoint problem and that if we rescaled our adjoint velocity variables so that within the critical layer,

$$(\tilde{\mathbf{u}}, \tilde{w}) = O_s(1) \tag{8.34}$$

then outside the critical layer of thickness $\hat{\delta} = \epsilon^{1/3} = \left(R\delta^4\right)^{-1/3}$, we must have

$$(\tilde{\mathbf{u}}, \tilde{w}) = O(\epsilon^{2/3}) \tag{8.35}$$

REFERENCES

BATCHELOR, G.K & GILL, A.E. 1962 Analysis of the stability of axisymmetric jets, *J. Fluid Mech.* **14** (4), 529-551.

BENNEY, D. 1984 The evolution of disturbances in shear flows at high Reynolds numbers. *Stud. Appl. Math.* **70**, 1-19.

BLACKBURN, H.M., HALL, P. & SHERWIN, S.J. 2013 Lower branch equilibria in Couette flow: the emergence of canonical states for arbitrary shear flows. *J. Fluid Mech.*, **726**, **R2**, 12.

DEGUCHI, K. & HALL, P. 2014 Free-stream coherent structures in parallel boundary-layer flows, *J. Fluid Mech.*, **752**: 602-625.

DEGUCHI, K. & HALL, P. 2014 Canonical exact coherent structures embedded in high Reynolds number flows, *Phil. Trans. R. Soc*, **A 372**: 20130352.

DEGUCHI, K. & WALTON, A.G. 2013 A swirling spiral wave Solution in pipe flow, *J. Fluid Mech*, **737**, (R2) 1-12.

FAISST, H. & ECKHARDT, B. 2003 Traveling waves in pipe flow. *Phys. Rev. Lett.*, **91**, 224502.

FITZERALD, R. 2004 New experiments set the scale for the onset for the onset of turbulence in pipe flow. *Physics Today* **57** (2), 21-24.

GIBSON, J.F., HALCROW, J. & CVITANOVIC, P. 2009 Equilibrium and travelling-wave solutions of plane Couette flow., *J. Fl. Mech*, **638**, 243-266.

HALL, P. & SHERWIN, S. 2010 Streamwise vortices in shear flows: harbingers of transition and the skeleton of coherent structures, *J. Fluid Mech.*, **661**, 178-205

HALL, P. & SMITH, F. 1991 On strongly nonlinear vortex/wave interactions in boundary layer transition, *J. Fluid Mech.*, **227**, 641-666.

HOF, B.,VAN DOORNE, C.,WESTERWEEL, J.,NIEUWSTADT, F., FAISST, H.,ECKHARDT, B.,WEDIN, H.,KERSWELL, R., & WALEFFE, F. 2004, Experimental observation of nonlinear traveling waves in the turbulent pipe flow. *Science* **305** (5690), 1594-1598.

LI, Y.C., & VISWANATH, D. 2009, EXACT AND ASYMPTOTIC CONDITIONS ON TRAVELING WAVE SOLUTIONS OF THE NAVIER-STOKES EQUATIONS, *Phys. Fluids*, **21**, 101703.

KERSWELL, R. & TUTTY, O. 2007. Recurrence of traveling waves in transitional pipe flow *J. Fluid Mech*, **584**, 69-102.

PRINGLE, C.C.T & KERSWELL, R.R. 2007. Asymmetric, helical and mirror-symmetric travelling waves in pipe flow. *Phys. Rev. Lett.*, **99**, 074502.

PRINGLE, C.C.T., DUGUET, Y., & KERSWELL, R.R. 2009. Highly symmetric travelling waves in pipe flow. *Phil. Trans. R. Soc.*, A **367**(1888), 457-472.

NAGATA, M. 1990 Three dimensional finite-amplitude solutions in plane Coutte flow: bifurcation from infinity *J. Fluid Mech*, **217**, 519-527.

OZCAKIR, O. 2014 Vortex-Wave solutions of Navier-Stokes equations in a cylindrical pipe, *Ph.D Thesis*, The Ohio State University.

SCHNEIDER, T., GIBSON, J., LAGHA, M., DE LILLO, F. & ECKHARDT, B. 2008 Laminer-Turbulent boundary in plane Couette flow, *Phys. Rev. E.* 037301.

SCHNEIDER, T. AND ECKHARDT, B. 2999 Edge States intermediate between laminar and turbulent dynamics in pipe flow, *Phil. Trans. R. Soc.*, A **367** 577-587.

SMITH, F.T. & BODONYI, R.J. 1982 Amplitude-dependent neutral modes in the Hagen-Poiseille flow through a circular pipe, *Proc. R. Soc. Lond.* A **384**, 463-489.

VISWANATH, D. 2007 Recurrent motions within plane Couette turbulence. *J. Fluid Mech*, **580**, 339-358.

VISWANATH, D. 2009 Critical layer in pipe flow at high Reynolds number, *Phi. Trans. R. Soc. A*, **580**, 561-576.

VISWANATH, D. & CVITANOVIC, P. 2009 Stable manifolds and the transition to turbulence in pipe flow., *J. Fluid Mech*, **627**, 215-233.

WALEFFE, F. 1995 Hydrodynamic stability and turbulence: beyond transients to a self-sustaining process, *Stud. Appl. Math.* **95** (3), 319-343.

WALEFFE, F. 1997 On a self-sustaining process in shear flows, *Phys. Fluids*, **9** (4), 883-900.

WALEFFE, F. 1998 Three dimensional coherent states in plane shear flows, *Phys. Rev. Lett.*, **81** (19), 4140-4143.

WALEFFE, F. 2001 Exact coherent structures in channel flow, *J. Fluid Mech*, **435**, 93-102.

Waleffe, F. 2003 Homotopy of exact coherent structures in plane shear flows, *Phys. Fluids*, **15** (6), 1517-1534.

Wang, J., Gibson, J. & Waleffe, F. 2007 Lower branch coherent states in shear flows: transition and control, *Phys. Rev. Lett.*, **98** (20), 204501.

Wedin, H & Kerswell, R. 2004 Exact coherent structures in pipe flow: travelling wave solutions, *J. Fluid Mech*, **508**, 333-371.
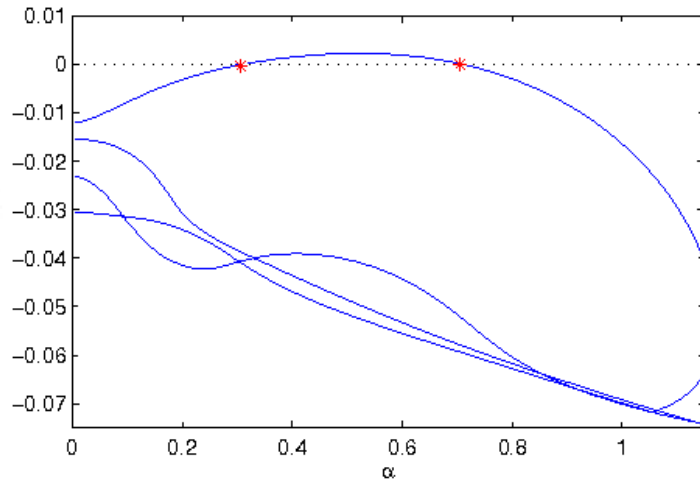
Figure 1: Im(c) versus α for the four least stable modes for $R = 1700$ and $s = 10$
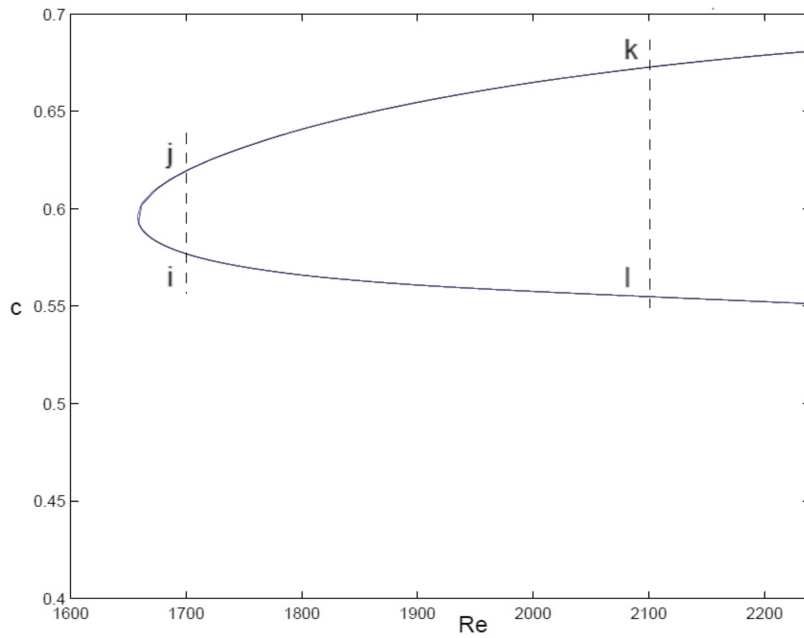
Figure 2: c versus R for WK branch at $\alpha = 1.55$: Gray Curve: Wedin and Kerswell (2004) calculations, Blue curve: Our $(N, M, P) = (45, 8, 5)$ calculations, Black Curve $(N, M, P) = (85, 12, 5)$.
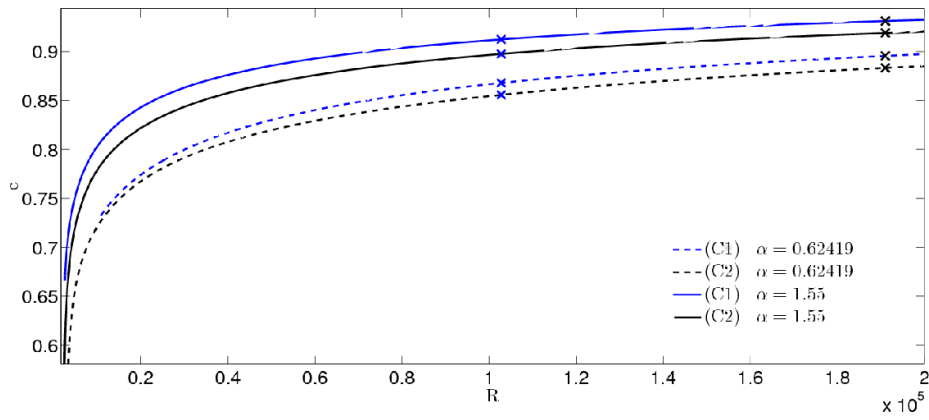
Figure 3: c vs. R for different solution branches $C1$, $C2$ for different axial wavelength α.

(a) (i) (b) (j)
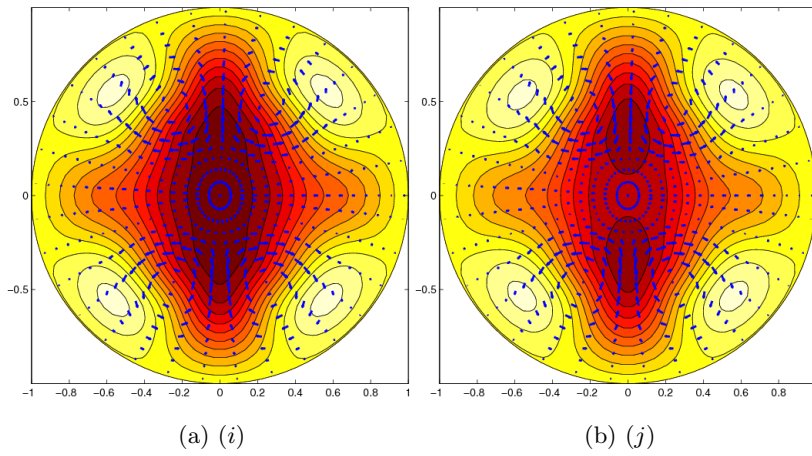
Figure 4: Streamwise averaged velocity profiles for WK solution at $R = 1700$, $\alpha = 1.55$, using $(N, M, P) = (45, 8, 5)$; (a) and (b) corresponding to points (i) and (j) in Figure 2.

(a) $C1$ (b) $C2$
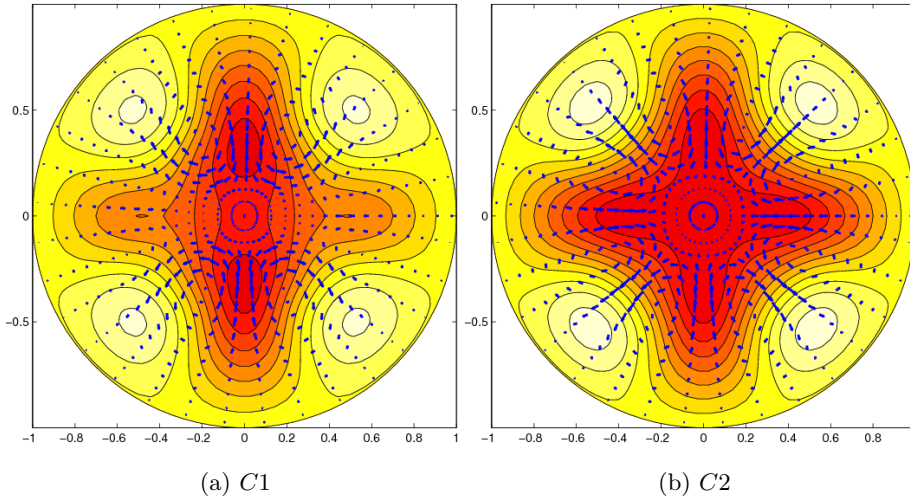
Figure 5: Streamwise averaged velocity profile at $R = 3940$ for $\alpha = 1.55$, using $(N, M, P) = (45, 8, 5)$. In (a) $\max W = 0.0712$, $\min W = -0.233$, $\max |(U, V)| = 0.00483$; (b) $\max W = 0.0806$, $\min W = -0.239$, $\max |(U, V)| = 0.042$.
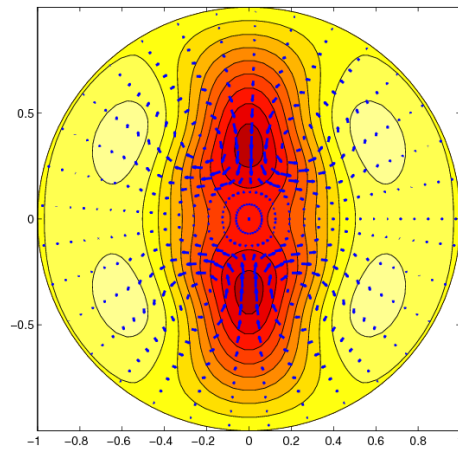
Figure 6: Streamwise averaged velocity profile for WK solution at $R = 3940$ for $\alpha = 1.55$, using $(N, M, P) = (45, 8, 5)$: $\max W = 0.0487$, $\min W = -0.26$, $\max |(U, V)| = 0.00466$

(a) $C1$ (b) $C2$
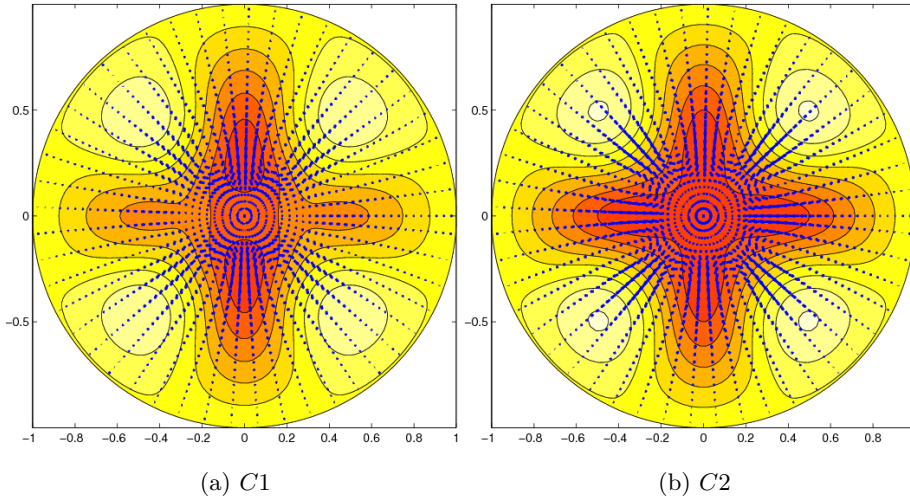
Figure 7: Streamwise averaged streamwise velocity profile at $R = 10^4$ for $\alpha = 1.55$, using $(N, M, P) = (85, 12, 5)$.
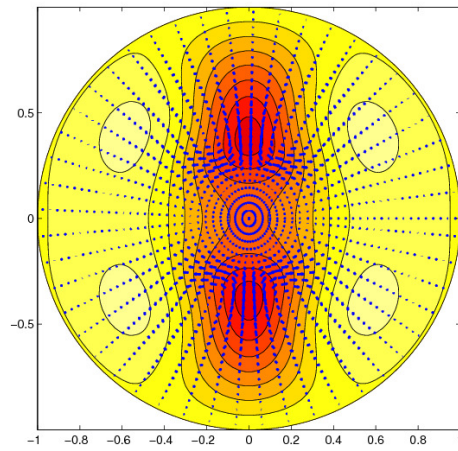
Figure 8: Streamwise averaged streamwise velocity profile at $R = 10^4$ for $\alpha = 1.55$, using $(N, M, P) = (85, 12, 5)$ for WK solution

O. Ozcakir, S. Tanveer, P. Hall and E.A.Overman

(a) *C1*   (b) *C2*
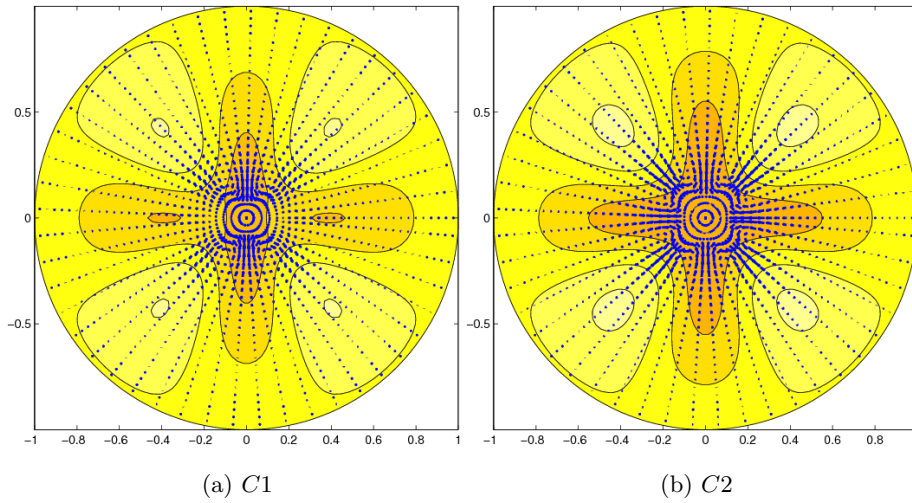
Figure 9: Streamwise averaged streamwise velocity profile at $R = 10^5$ for $\alpha = 1.55$, using $(N, M, P) = (85, 12, 5)$.
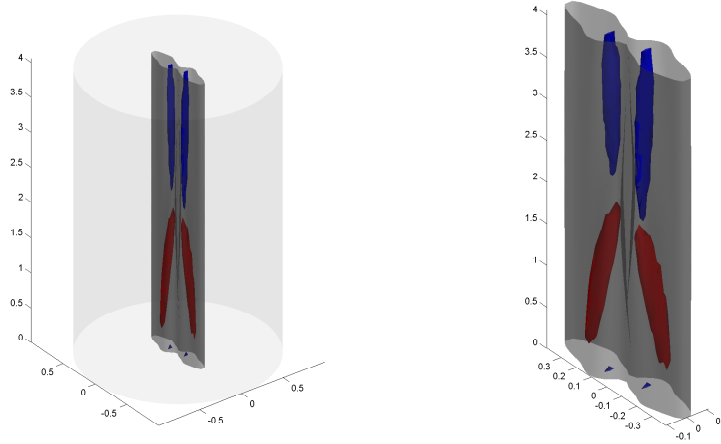
Figure 10: Streamwise velocity and vorticity isosurfaces at 0.8 times extreme values at $R = 50,000$ for $\alpha = 1.55$ for $C1$.
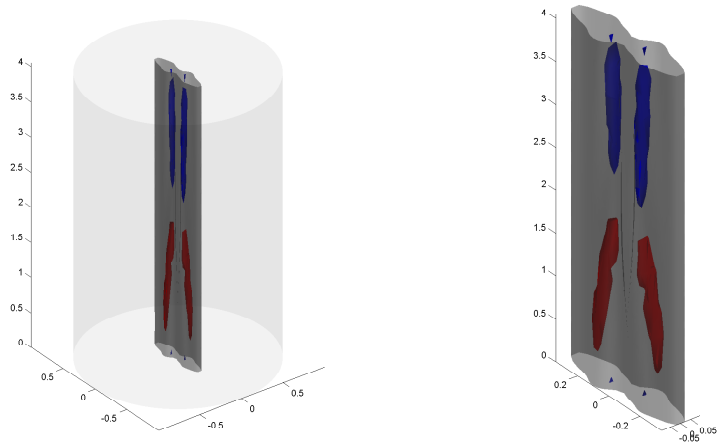
Figure 11: Streamwise velocity and vorticity isosurfaces at 0.8 times extreme values at $R = 102,820$ for $\alpha = 1.55$ for $C1$.
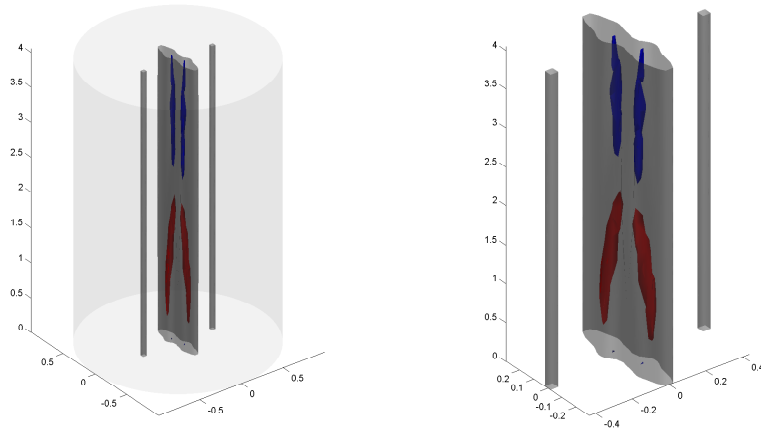
Figure 12: Streamwise velocity and vorticity isosurfaces at 0.8 times extreme values at $R = 191,020$ for $\alpha = 1.55$ for $C1$.
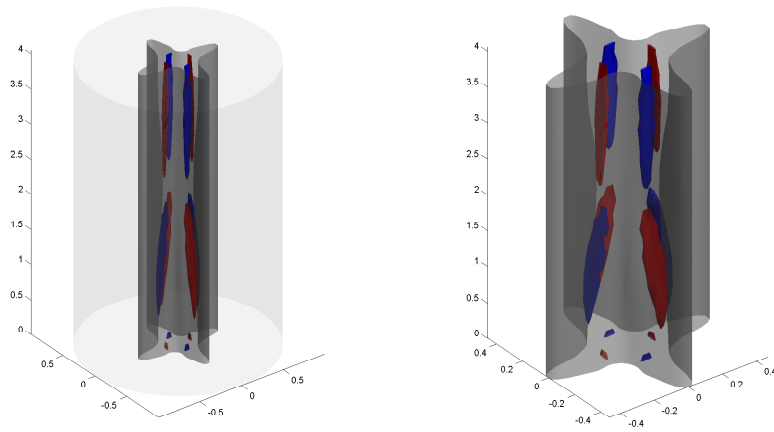
Figure 13: Streamwise velocity and vorticity isosurfaces at 0.8 times extreme values at $R = 50,000$ for $\alpha = 1.55$ for $C2$.
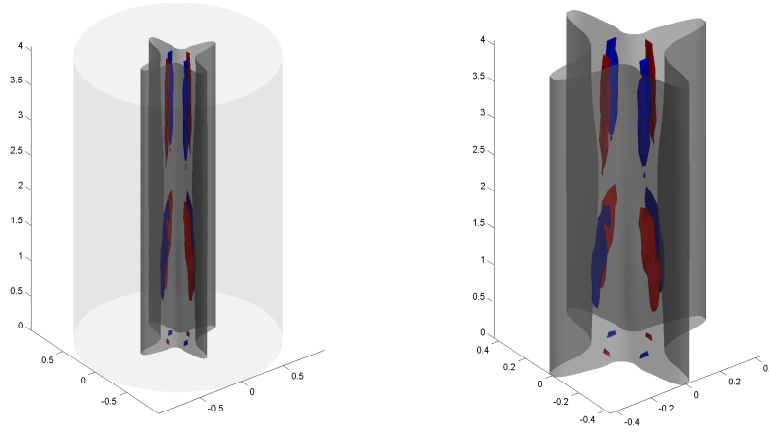
Figure 14: Streamwise velocity and vorticity isosurfaces at 0.8 times extreme values at $R = 102,820$ for $\alpha = 1.55$ for $C2$.
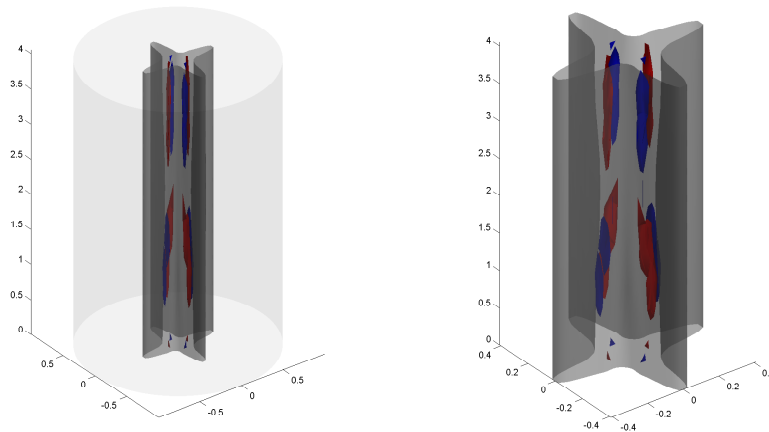
Figure 15: Streamwise velocity and vorticity isosurfaces at 0.8 times extreme values at $R = 191,020$ for $\alpha = 1.55$ for $C2$.
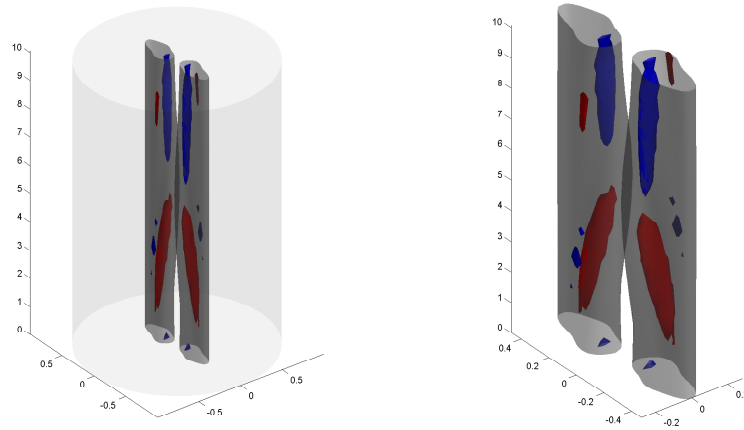
Figure 16: Streamwise velocity and vorticity isosurfaces at 0.8 times extreme values at $R = 50,000$ for $\alpha = 0.624$ for $C1$.
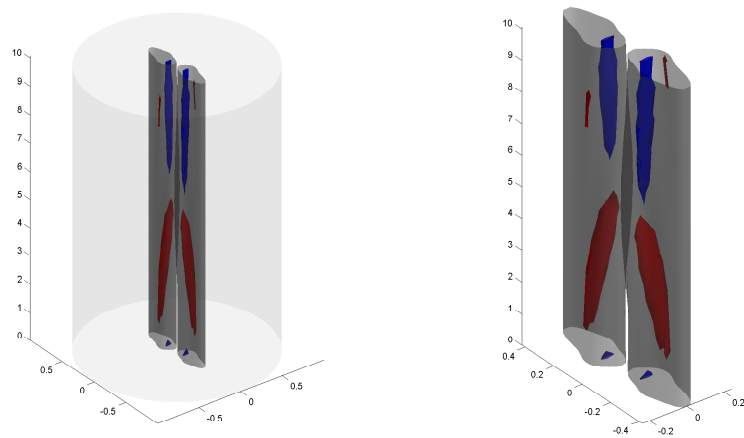
Figure 17: Streamwise velocity and vorticity isosurfaces at 0.8 times extreme values at $R = 102,820$ for $\alpha = 0.624$ for $C1$.
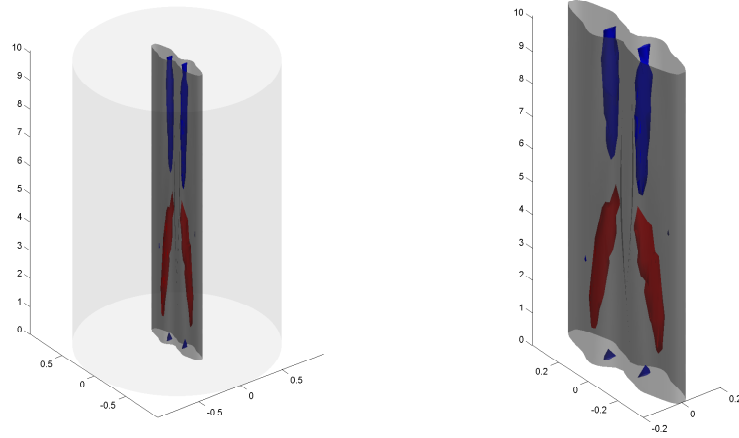
Figure 18: Streamwise velocity and vorticity isosurfaces at 0.8 times extreme values at $R = 191,020$ for $\alpha = 0.624$ for $C1$.
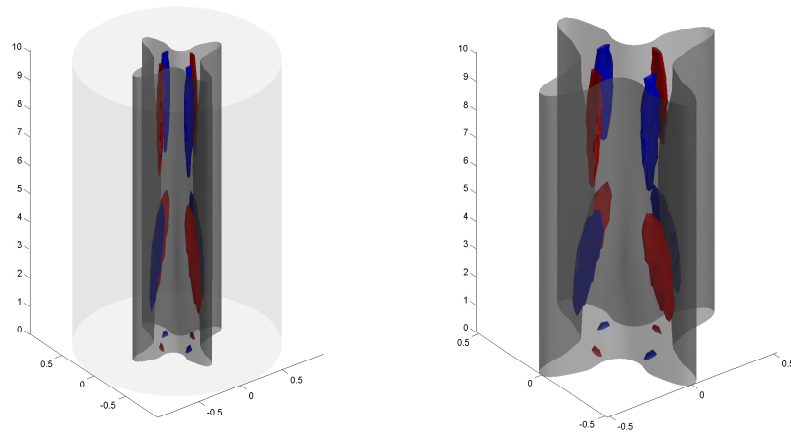
Figure 19: Streamwise velocity and vorticity isosurfaces at 0.8 times extreme values at $R = 50,000$ for $\alpha = 0.624$ for $C2$.

O. Ozcakir, S. Tanveer, P. Hall and E.A.Overman
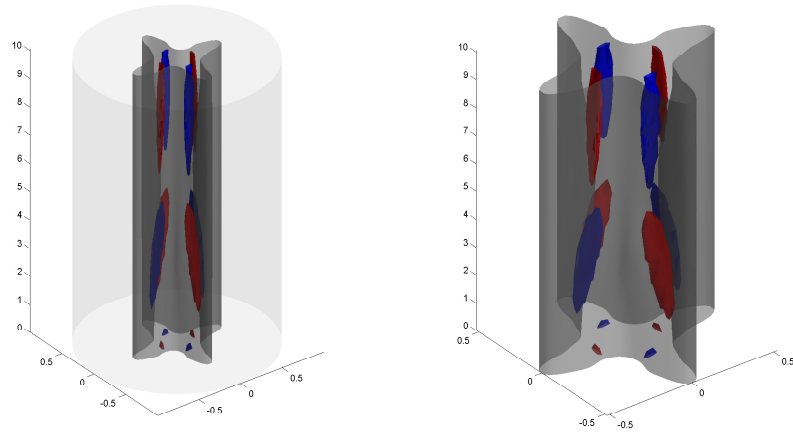
Figure 20: Streamwise velocity and vorticity isosurfaces at 0.8 times extreme values at $R = 102,820$ for $\alpha = 0.624$ for $C2$.
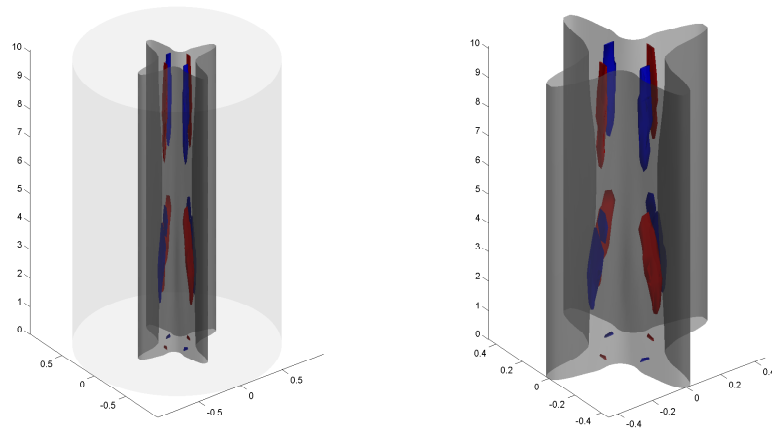
Figure 21: Streamwise velocity and vorticity isosurfaces at 0.8 times extreme values at $R = 191,020$ for $\alpha = 0.624$ for $C2$.
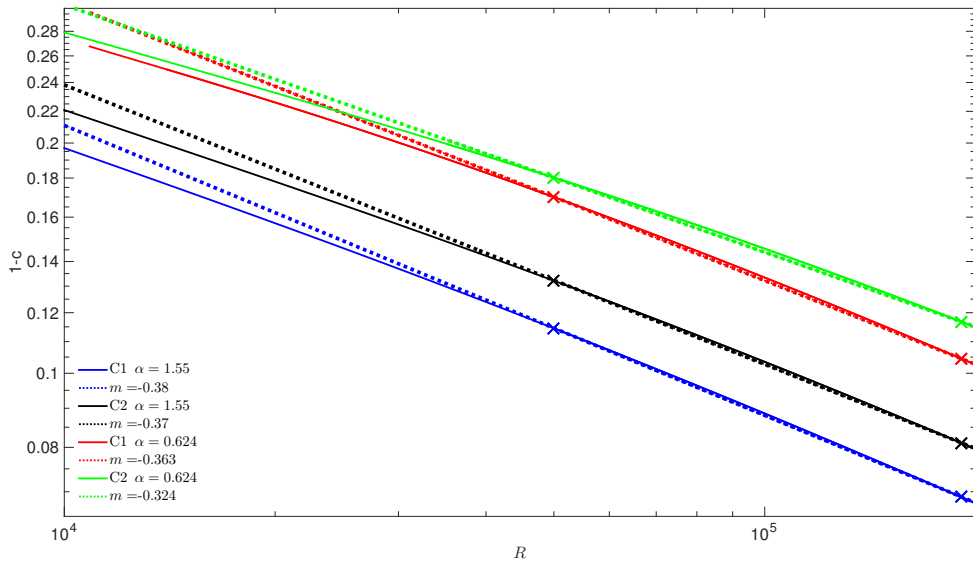
Figure 22: $1 - c$ vs. R in a $\log - \log$ scale for different α for $C1$ and $C2$ solutions. Dotted lines are linear approximations to each curve using larger R.
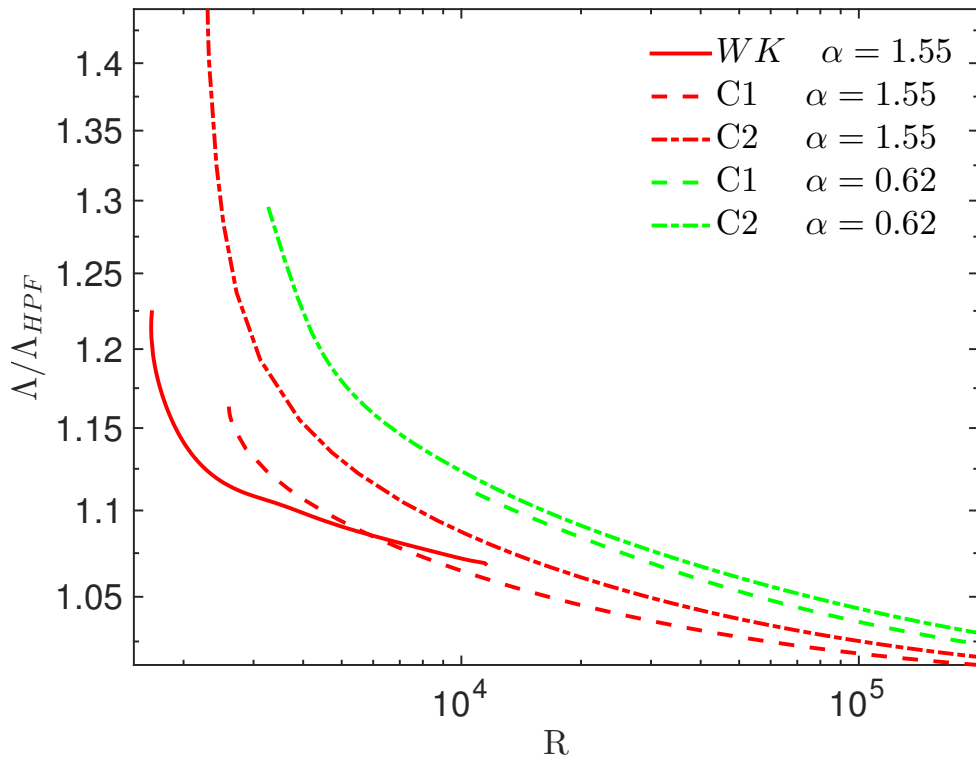
Figure 23: Friction factor ratio Λ/Λ_{HPF} vs. R for lower branch WK, $C1$ and $C2$ solutions at $\alpha = 1.55$, $\alpha = 0.624$; note $\Lambda = \Lambda_{HPF} = 64/R$ for Hagen-Poiseuille flow.

(a) $C1$ (b) $C2$
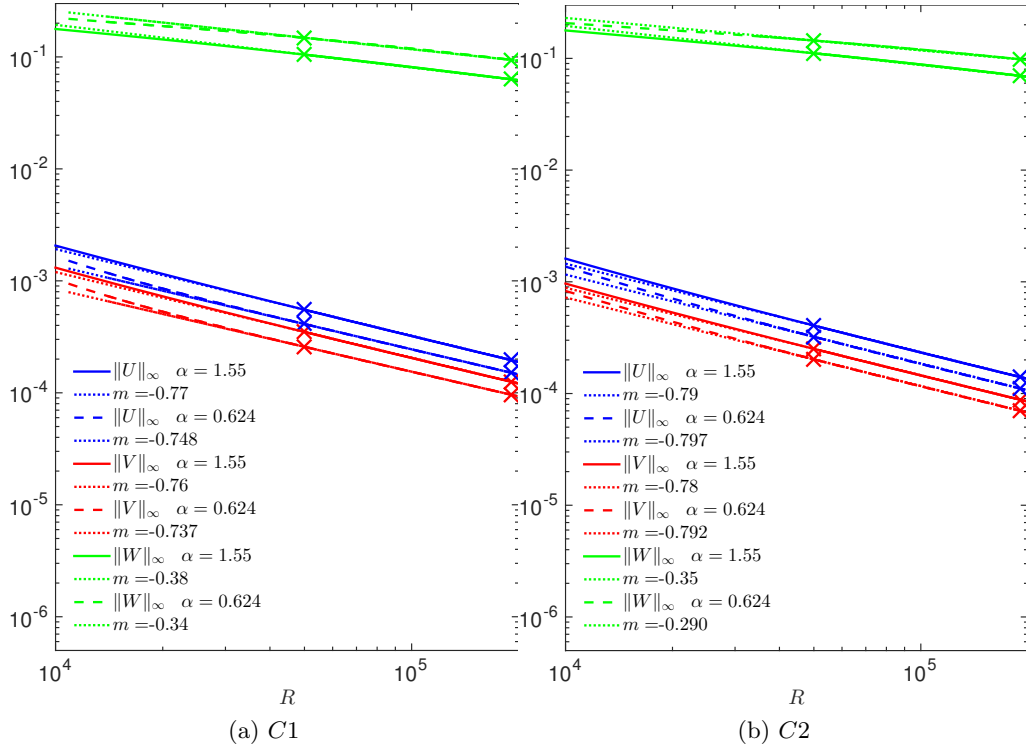
Figure 24: Sup- Norm of Roll components (U, V) and of sreak W vs. R for $C1$ and $C2$ solution.
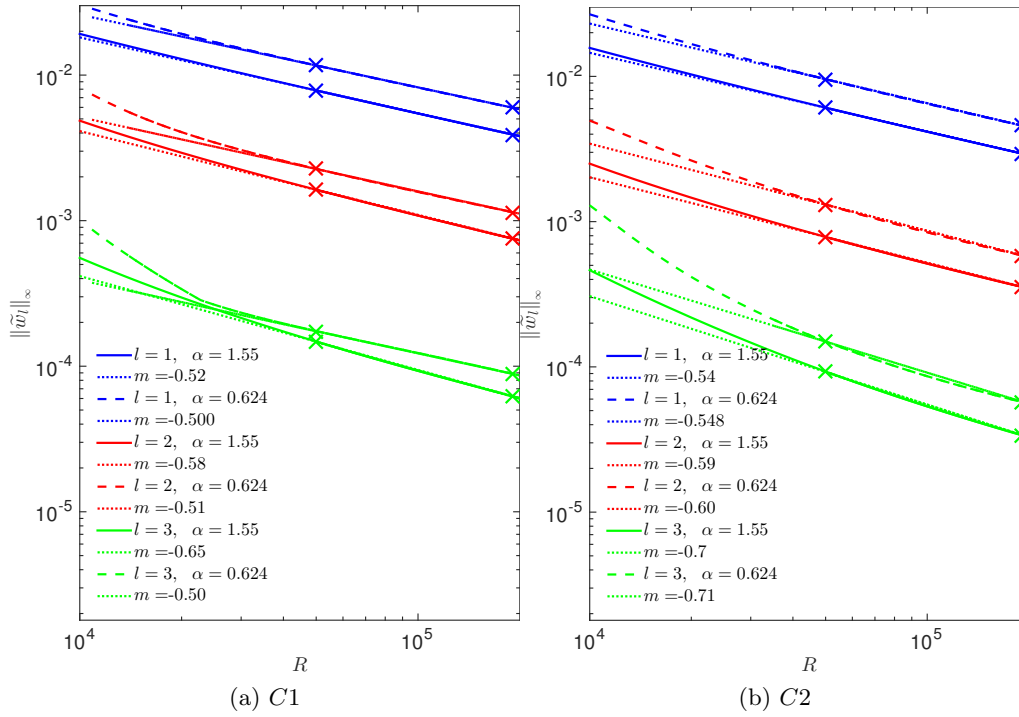
Figure 25: Supremum over (r, θ) of wave components $\widetilde{w}_l$ at $l = 1, 2, 3$ for $C1$ and $C2$ solutions for different α.
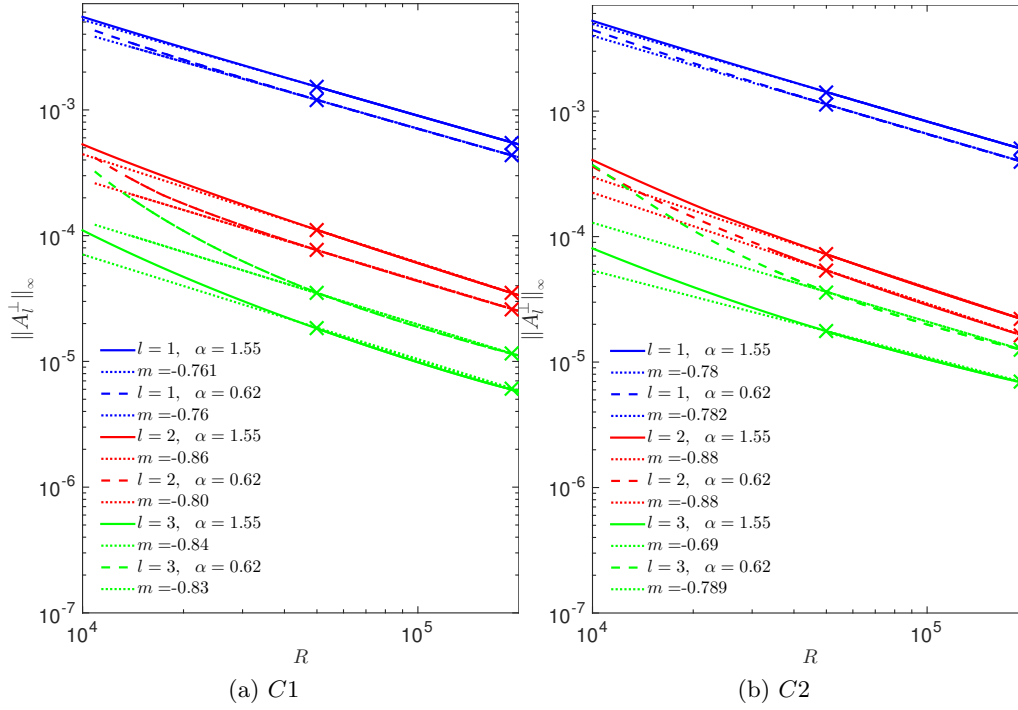
Figure 26: Supremum over (r, θ) of $\perp$ wave components u_l at $l = 1, 2, 3$ for $C1$ and $C2$ solutions for different α.
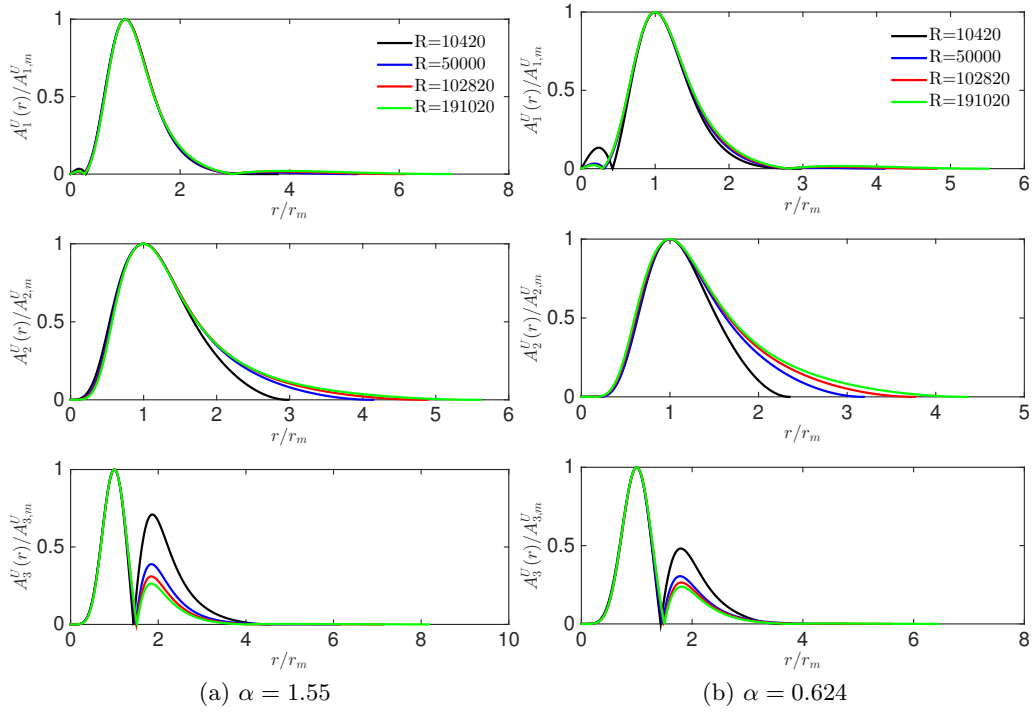
Figure 27: Scaled radial roll amplitude function $A_k^U(r)/A_{k,m}^U$ vs. r/r_m for $C1$ solution for $k = 1, 2, 3$ for different R.

(a) $\alpha = 1.55$ (b) $\alpha = 0.624$
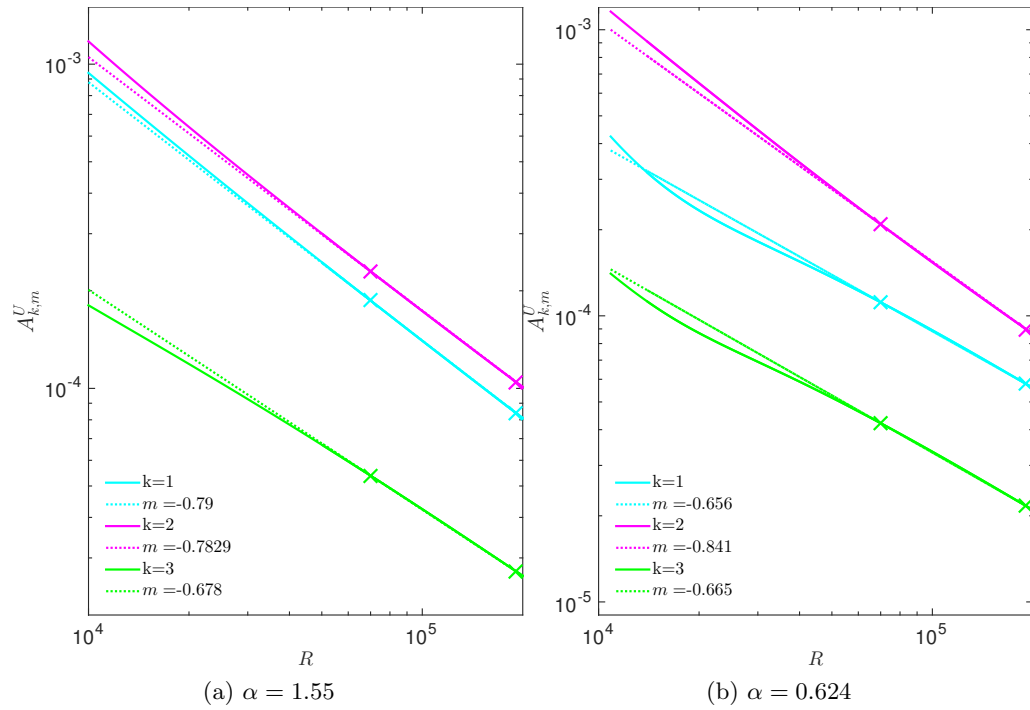
Figure 28: Maximal radial roll amplitude $A_{k,m}^U$ for k-th azimuthal component versus R for $C1$ solution for $\alpha = 1.55$ and $\alpha = 0.624$.

(a) $\alpha = 1.55$

(b) $\alpha = 0.624$
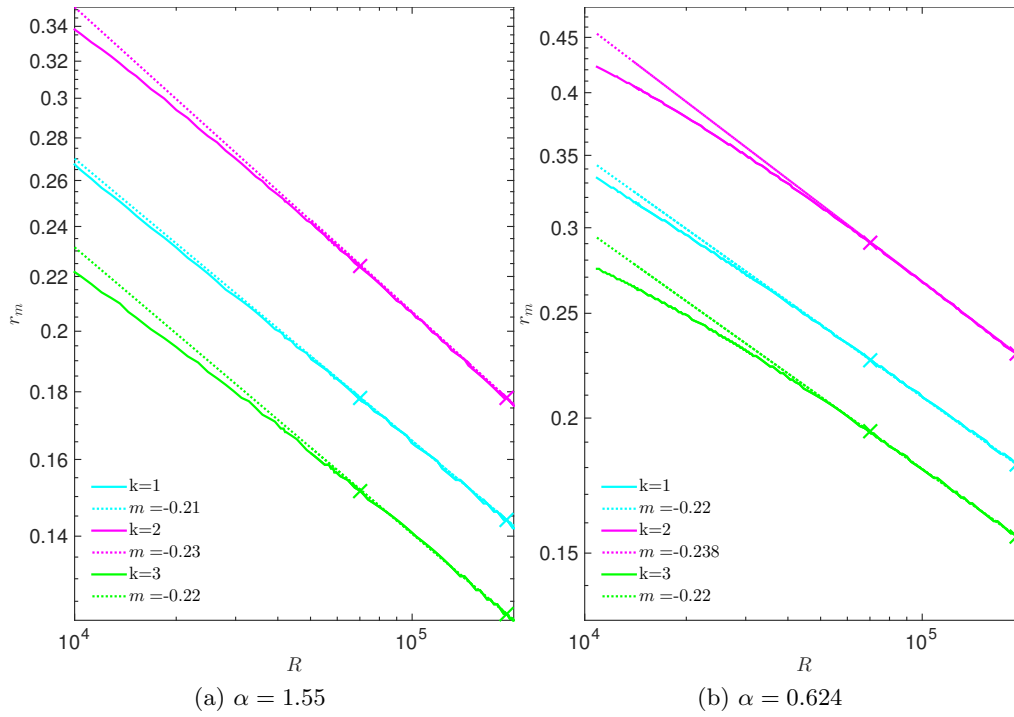
Figure 29: Maximal radial roll amplitude location for k-th azimuthal mode r_m against R for $C1$ solution for $\alpha = 1.55$ and $\alpha = 0.624$.

(a) $\alpha = 1.55$ (b) $\alpha = 0.624$
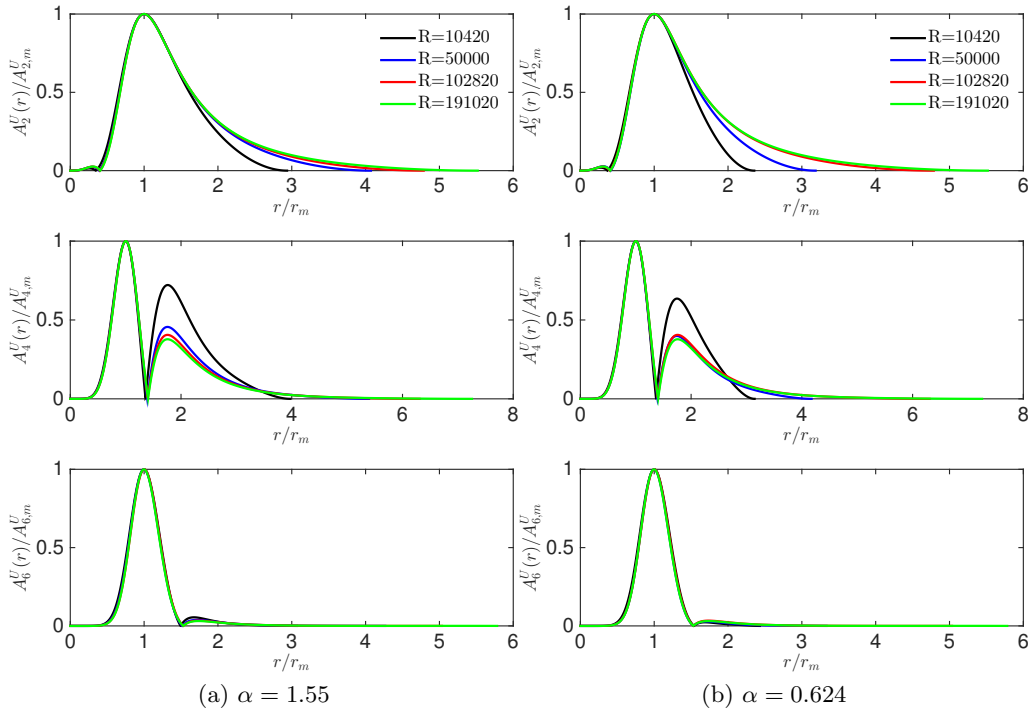
Figure 30: Scaled radial roll amplitude function $A_k^U(r)/A_{k,m}^U$ vs. r/r_m for $C2$ solution for $k = 2, 4, 6$ for different R.
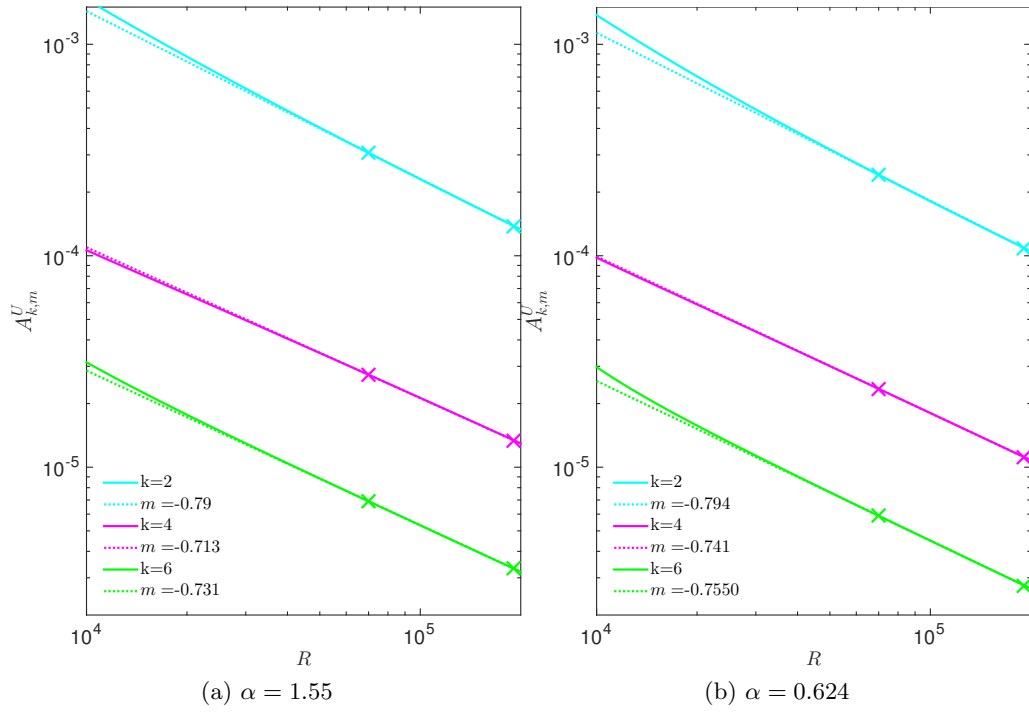
Figure 31: Maximal radial roll amplitude $A_{k,m}^{U}$ for k-th azimuthal component vs R for $C2$ solution for $\alpha = 1.55$ and $\alpha = 0.624$.

(a) $\alpha = 1.55$　　　　　　　　　　(b) $\alpha = 0.624$
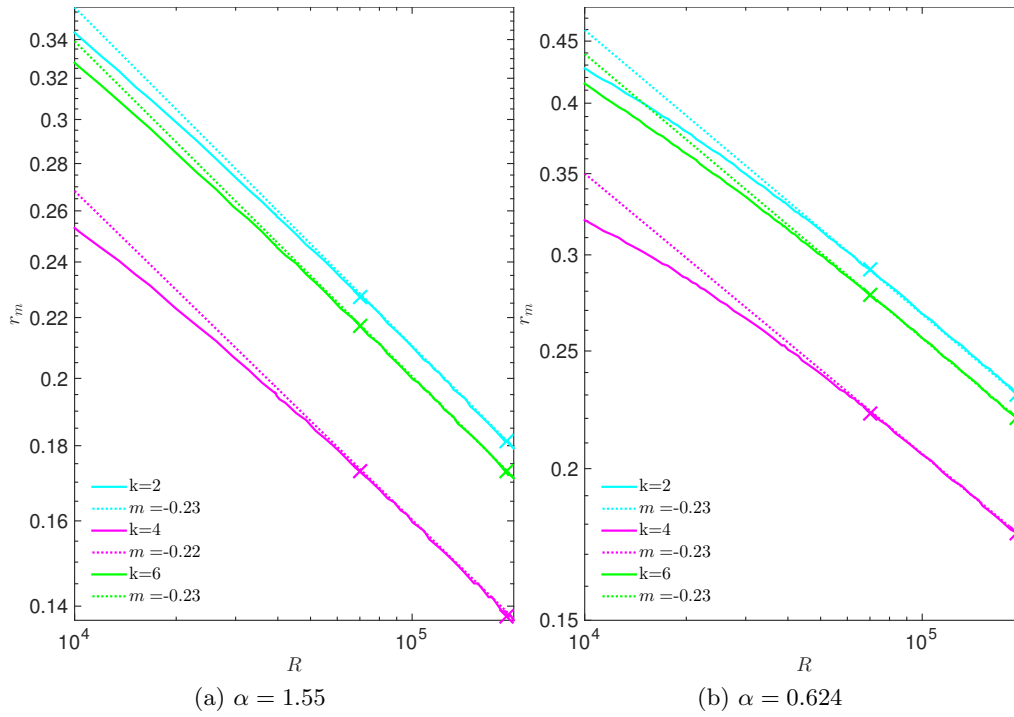
Figure 32: Radial location r_m for maximal radial roll amplitude versus R for $C2$ solution for $\alpha = 1.55$ and $\alpha = 0.624$.

(a) $\alpha = 1.55$ (b) $\alpha = 0.624$
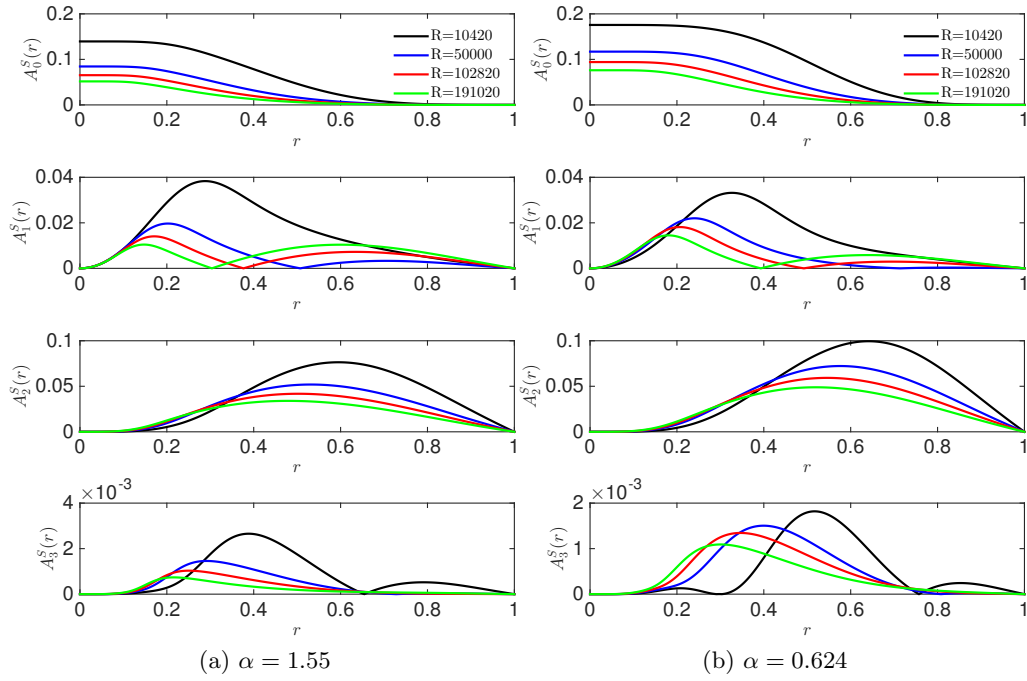
Figure 33: Profile of $C1$- Streak amplitude $A_k^S(r)$ versus r for different R and k for given α.
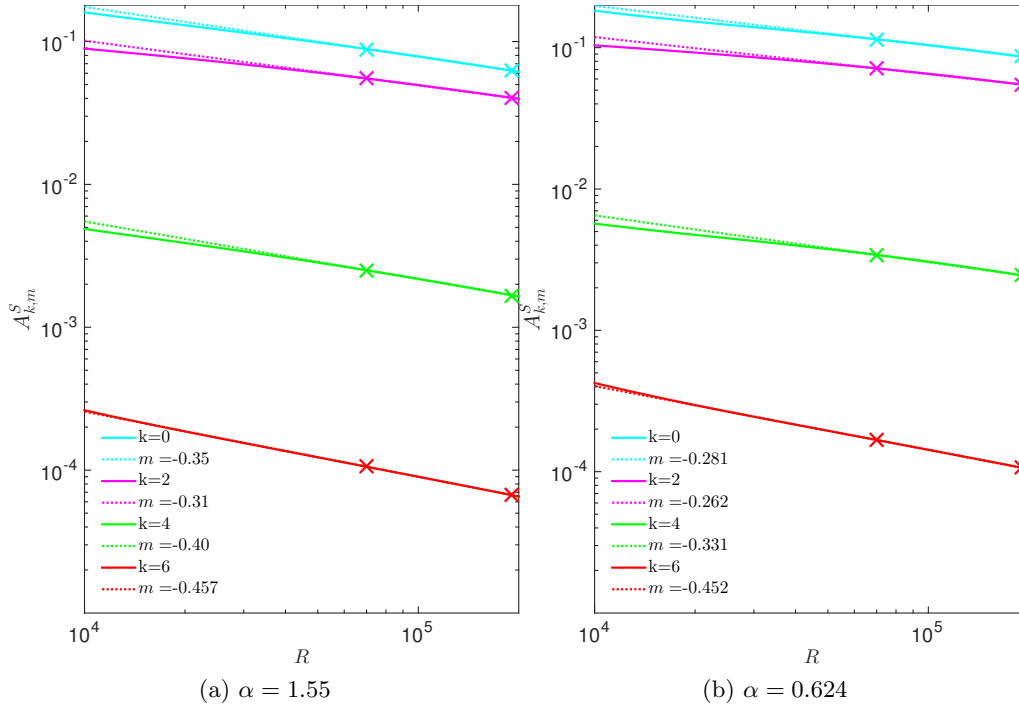
(a) $\alpha = 1.55$

(b) $\alpha = 0.624$
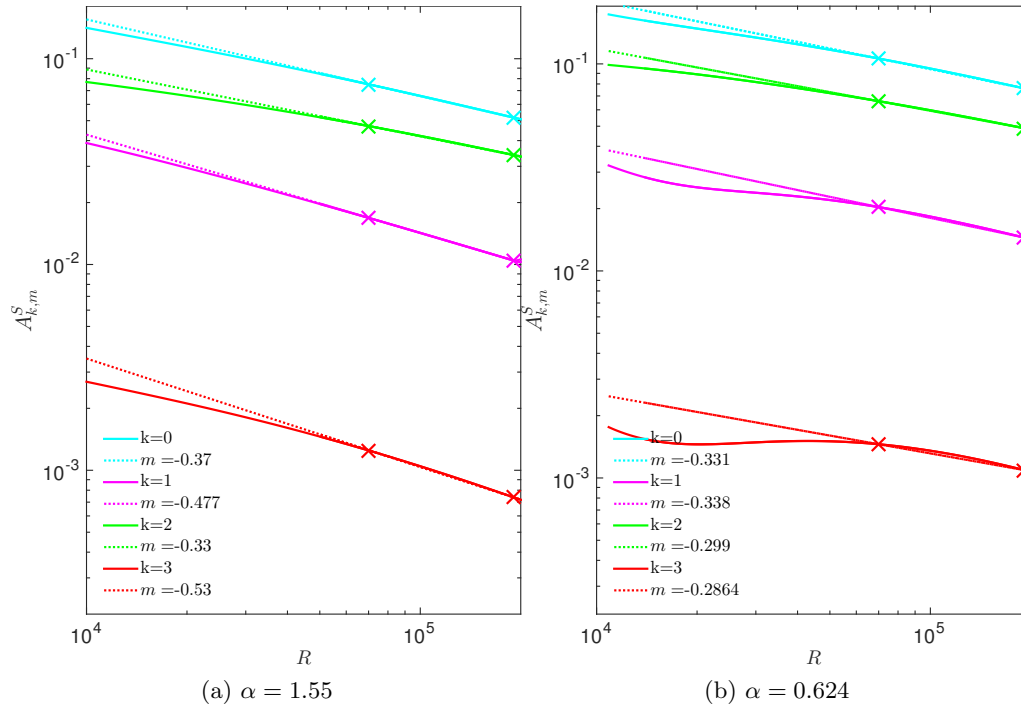
Figure 34: Maximal kth streak amplitude $A_{k,m}^S$ vs. R for $C1$ solution for $k = 0, 1, 2, 3$ for $\alpha = 1.55$ and $\alpha = 0.624$.
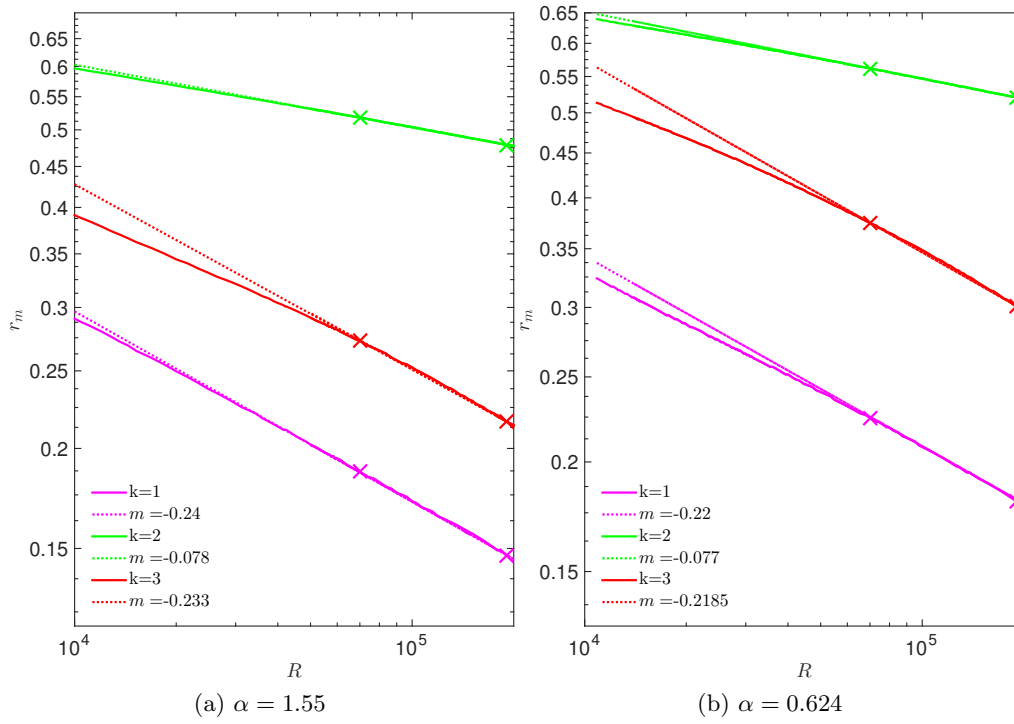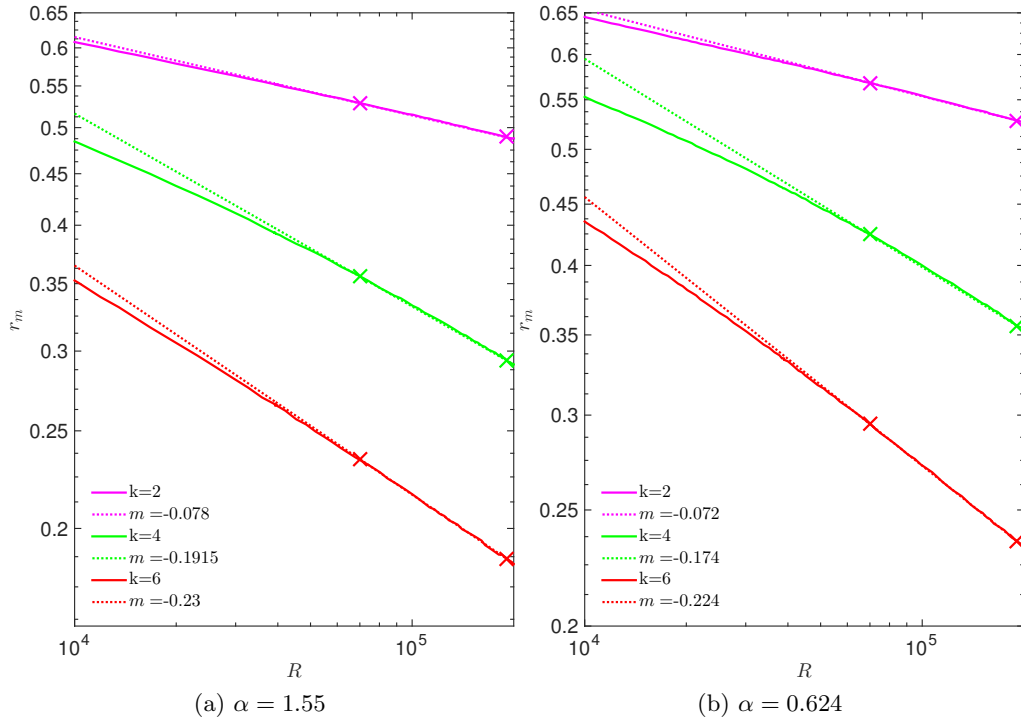
Figure 35: Radial location r_m where maximal streak amplitude occurs in Figure 34 for $C1$ solution against R for different k for two different $\alpha = 1.55$ and $\alpha = 0.624$. $k = 0$ is missing since it has a flat profile.

(a) $\alpha = 1.55$ (b) $\alpha = 0.624$
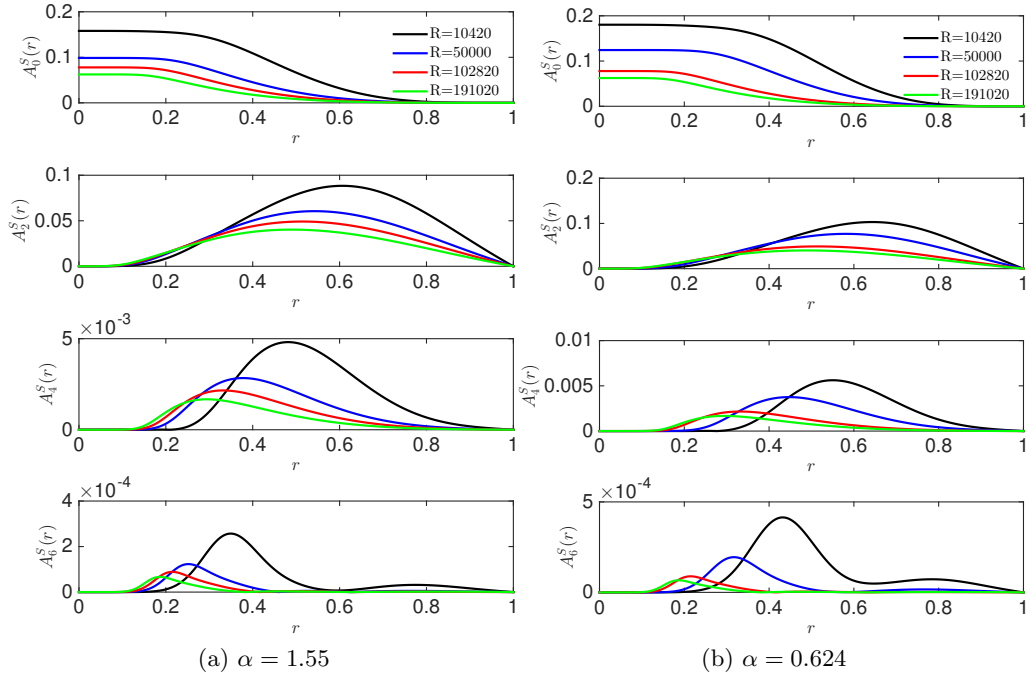
Figure 36: Profile of $C2$ Streak amplitude $A_k^S(r)$ versus r for different R and k for given α

(a) $\alpha = 1.55$ (b) $\alpha = 0.624$

Figure 37: Maximal kth streak amplitude $A_{k,m}^S$ vs. R for $C2$ solution for $k = 0, 2, 4, 6$ for $\alpha = 1.55$ and $\alpha = 0.624$.

(a) $\alpha = 1.55$ (b) $\alpha = 0.624$

Figure 38: Radial location r_m where maximal streak amplitude occurs in Figure 37 for $C2$ solution against R for different k for two different $\alpha = 1.55$ and $\alpha = 0.624$. $k = 0$ is missing since it has a flat profile.
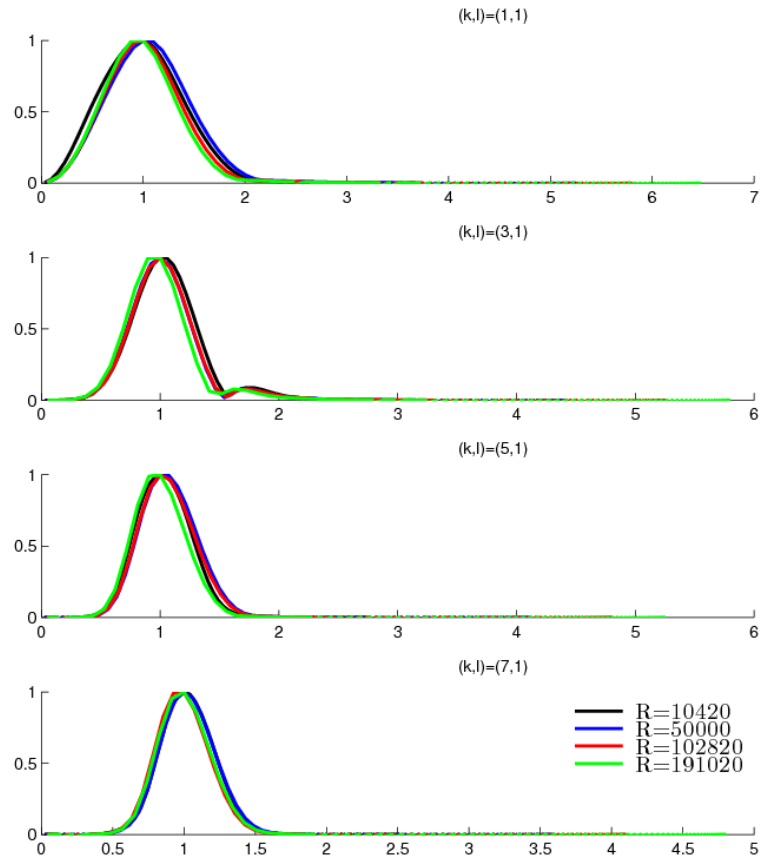
Figure 39: scaled axial wave amplitude $w_{kl}(r)/w_{k,l,m}$ versus r for $C2$ solution at $l = 1$ for different k for $\alpha = 1.55$.
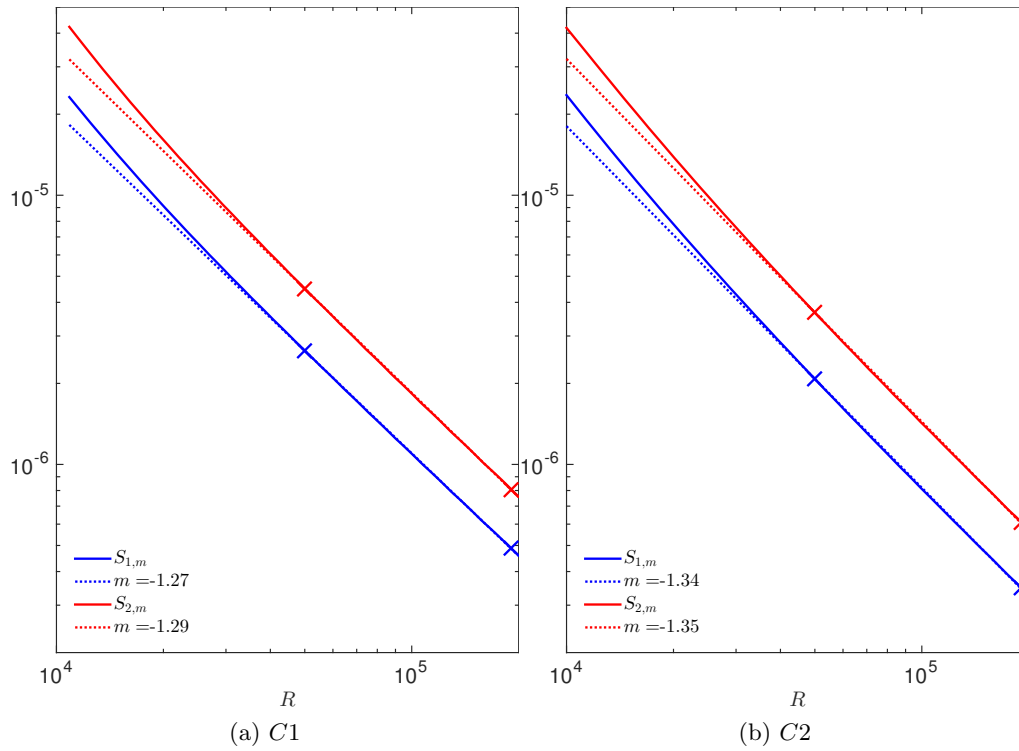
Figure 40: Scaling of maximal wave stress $S_{1,m}$, $S_{2,m}$ with R for $\alpha = 0.624$ for (a) $C1$ and (b) $C2$ solutions.
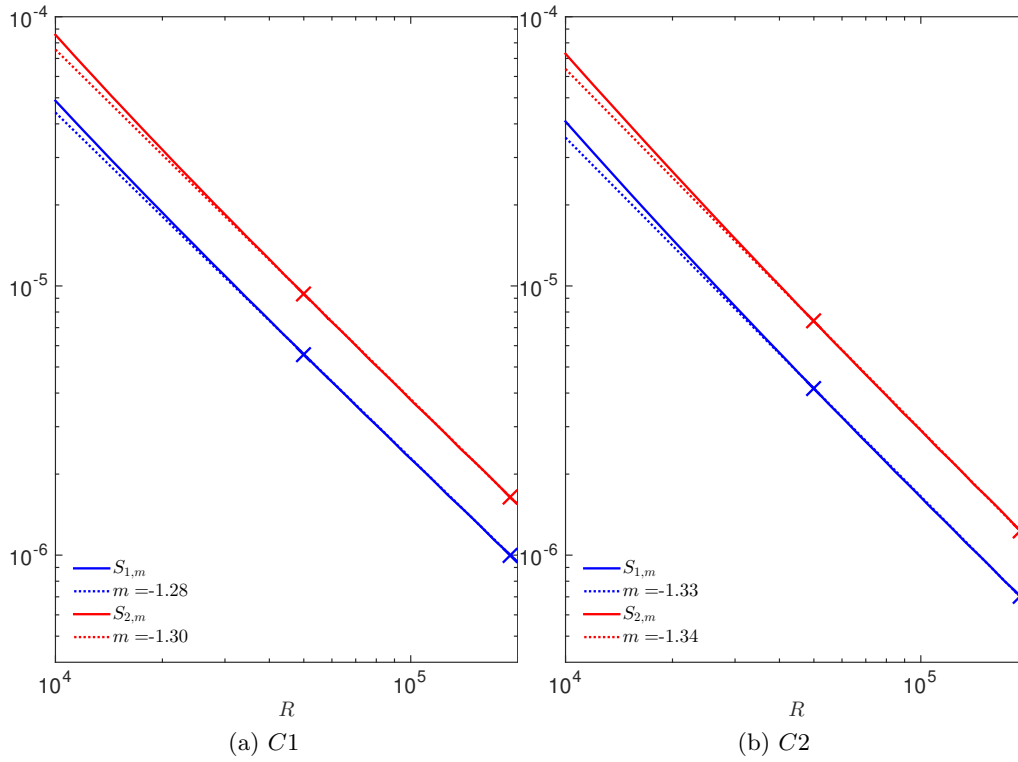
Figure 41: Scaling of maximal wave stress $S_{1,m}$, $S_{2,m}$ with R for $\alpha = 1.55$ for (a) $C1$ and (b) $C2$ solutions.
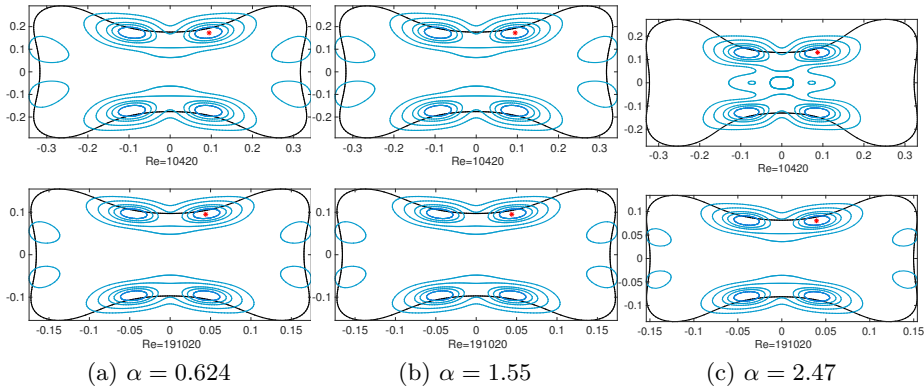
.

Figure 42: S_2 contours for $C1$ solution showing 0.9, 0.8, 0.7, 0.5 and 0.3× $S_{2,m}$ for three different values of R for given α. Critical Curve is shown in black, and location of $S_{2,m}$ shown in *.

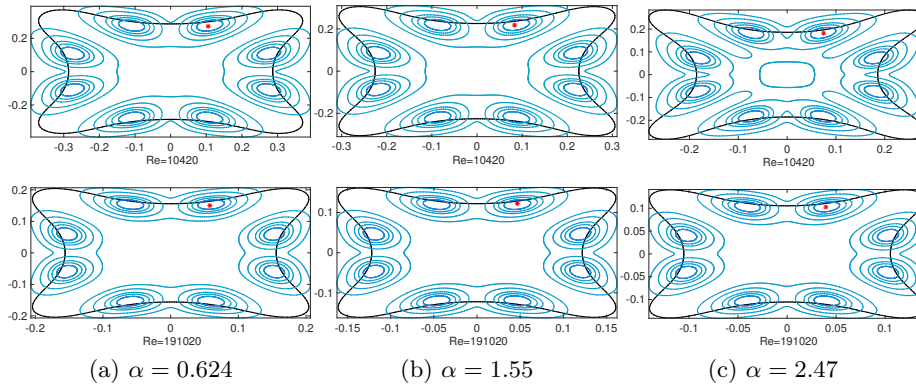(a) $\alpha = 0.624$ (b) $\alpha = 1.55$ (c) $\alpha = 2.47$

Figure 43: S_2 contours for $C2$ solution showing 0.9, 0.8 ,0.7,0.5 and 0.3$\times$ $S_{2,m}$ for three different values of R. Critical Curve is shown in black, and location of $S_{2,m}$ shown in $*$.